

Computer simulation of altermagnets with relativistic corrections

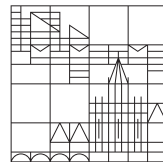
BACHELOR'S THESIS

submitted by

Marian Duelli
(01/1267440)

at the

Universität
Konstanz



Mathematics and Natural Sciences Section
Physics Department
Group of Prof. Dr. Ulrich Nowak

Supervisor: Moumita Kundu

First reviewer: Prof. Dr. Ulrich Nowak

Konstanz, 16th October 2025

Abstract

Altermagnets (AMs) represent an emerging class of magnetic materials that combine properties of ferromagnets (FMs) and antiferromagnets (AFMs), offering significant potential for spintronics applications. This thesis investigates the fundamental characteristics of spin dynamics in a simplified altermagnetic system through computer simulations. The study employs a two-dimensional toy model on a checkerboard lattice featuring anisotropic intrasublattice exchange interactions that fulfil the required altermagnetic symmetry criteria. Spin dynamics are modelled using atomic spin dynamics simulations based on the stochastic Landau-Lifshitz-Gilbert (LLG) equation.

The work establishes a clear link between the anisotropic exchange interactions and the direction-dependent splitting of the magnon dispersion relation. The introduction of an external magnetic field along the easy axis is shown to shift the magnon bands, alter magnon populations, and induce a net magnetization. This interplay is used to explain the microscopic origins of the spin Seebeck effect (SSE), with analysis extended to magnon propagation lengths and the calculation of longitudinal spin currents. Furthermore, the study provides evidence for the magnonic spin Nernst effect (SNE) by identifying a transverse spin accumulation at the material's edges and calculating a pure transverse spin current for specific crystallographic directions. Finally, the influence of the relativistic Dzyaloshinskii-Moriya interaction (DMI) on the system's equilibrium state and the SSE is examined, with the caveat that the presented implementation breaks the altermagnetic symmetry.

This research provides valuable microscopic insights into spin excitations and thermal transport phenomena in altermagnets, contributing to the foundational understanding of this novel magnetic phase.

Zusammenfassung

Technologische Fortschritte erhöhen die Anforderungen an Informations- und Speichertechnologien kontinuierlich [1, 2]. In diesem Kontext bietet die Spintronik die Möglichkeit den Spin-Freiheitsgrad als Informationsträger zu verwenden [3]. Speziell können kollektive Anregungen magnetischer Momente in Festkörpern, genannt Magnonen, benutzt werden, um Informationen zu transportieren. Diese Technologie bringt den Vorteil verringerten Energieverbrauchs durch Reduktion von Abwärme [4], erhöhten Bearbeitungsgeschwindigkeiten und Nonvolatilität [3].

Die vorliegende Arbeit befasst sich mit dem Bereich der Spinkaloritronik [5, 6], also temperaturgesteuerten Spintronik. In der Vergangenheit wurden Ferromagnete und Antiferromagnete bereits intensiv untersucht [7], wobei beide Klassen gewisse Vorteile besitzen [8]. Eine vielversprechende magnetische Phase, genannt Altermagnetismus, ist zunehmend von Forschungsinteresse [8, 9], da sie verspricht gewisse Eigenschaften von Ferro- und Antiferromagneten zu vereinen. Altermagnete besitzen keine Nettomagnetisierung, sind durch nichtrelativistisches Splitting von Magnonenbändern und bestimmte Symmetriekriterien ausgezeichnet [8–11].

Methodisch wird ein vereinfachtes zwei-dimensionales Modell, basierend auf einem Schachbrettgitter mit anisotropen Austauschenergien im selben Untergitter, das die altermagnetischen Symmetriebedingungen erfüllt, verwendet. Die Dynamik der magnetischen Momente wird klassisch mittels der Landau-Lifshitz-Gilbert Gleichung modelliert, welche eine Präzession einzelner Momente mit heuristischer Dämpfung beschreibt. Thermische Störungen werden mittels eines temperaturabhängigen Rauschterms berücksichtigt, welcher die Anregung einzelner Momente verursacht.

Die Computersimulation basiert dann darauf, dass diese stochastische Landau-Lifshitz-Gilbert Gleichung numerisch integriert wird, damit dynamische Prozesse vorhergesagt werden und schließlich Gleichgewichtszustände erschlossen werden können. Das numerische Lösen dieser stochastischen Prozesse wird Langevin-Simulation genannt [12] und wird hier hochparallelisiert auf Grafikkarten durchgeführt, um die Simulation großer Systeme zu ermöglichen.

Die Simulationsergebnisse bestätigen eine eindeutige, richtungsabhängige Aufspaltung der Magnonmoden. Die Arbeit etabliert eine direkte, mikroskopische Verknüpfung zwischen den richtungsabhängigen Heisenberg-Austauschenergien. Der Einfluss eines externen magnetischen Feldes resultiert in einer Verschiebung der Magnonenbänder, Aufhebung der Entartung am Gamma-Punkt, einer veränderten Magnonpopulation der verschiedenen Moden und eine Nettomagnetisierung des Materials. Die dadurch gewonnenen Informationen können weiter verwendet werden, um den hier simulierten Spin Seebeck Effekt zu erklären, auch unter Einfluss eines Magnetfeldes.

Der Spin Seebeck Effekt beschreibt die Generation eines Spinstroms unter Einfluss

eines Temperaturgradienten, hier eine abrupte Temperaturstufe. Die mikroskopischen Ursachen werden weiter untersucht, indem die Ausbreitungsdistanz („propagation length“) der zwei Magnonmoden in verschiedene altermagnetische Richtungen bestimmt wird. Der Spin Seebeck Effekt wird direkt nachgewiesen, indem basierend auf den mikroskopischen Spinkonfigurationen ein longitudinaler magnonischer Spinstrom berechnet wird.

Als weiterer Effekt wird der Spin Nernst Effekt betrachtet, der die Generation transversaler Spinströme als Resultat eines longitudinalen Temperaturgradienten beschreibt. Diese Arbeit stellt Beweise für die Existenz dieses Effekts in diesem Modell eines Altermagneten bereit. Einerseits wird eine Magnonakkumulation an den Rändern des Materials festgestellt, aber auch ein rein magnonischer Spinstrom direkt nachgewiesen. Da die Existenz eines reinen magnonischen Spin Nernst Effekt noch nicht zweifelsfrei experimentell nachgewiesen werden konnte [13, 14], zeigt sich die Existenz in diesem Altermagnetismus-Modell vielversprechend.

Letztlich wird der Einfluss der relativistischen Dzyaloshinskii-Moriya-Interaktion auf den Gleichgewichtszustand und den Spin Seebeck Effekt betrachtet. Die Ergebnisse dieser Untersuchung sind unter dem Vorbehalt, dass die konkrete Implementation hier die altermagnetische Symmetrie zerstört, zu sehen. Es wird eine zusätzliche relativistische Aufspaltung der Magnonbänder um den Gamma-Punkt festgestellt, solange der relativistische Effekt stark genug ist. Weiter, wird eine Verkantung der magnetischen Momente bestätigt, und beobachtet, dass durch das Wechselspiel von einem externen magnetischen Feld und der relativistischen Interaktion, Effekte verstärkt werden. Das Verkanten resultiert in einem schwachen magnetischen Moment, was den Spin Seebeck in einer weiteren Spinkomponente ermöglicht, unabhängig von der kristallographischen Richtung.

Insgesamt bietet die hier vorgestellte Forschung nützliche mikroskopische Einblicke in Spinanregungen und damit verbundenen Transportphänomenen in Altermagneten. Ziel ist ein Beitrag zum fundamentalen Verständnis der neuartigen magnetischen Phase des Altermagnetismus und einem simulationsbasierten Nachweis des magnonischen Spin Nernst Effektes.

Contents

Abstract	iii
Zusammenfassung	v
1 Introduction	1
2 Theory	3
2.1 Solid state magnetism	3
2.1.1 Atomic magnetic moments	3
2.1.2 Extended Heisenberg model	5
Dzyaloshinskii-Moriya interaction (DMI)	6
2.1.3 Stochastic Landau-Lifshitz-Gilbert equation	7
2.1.4 Magnons	9
Relation to classic spin models	12
Antiferromagnetic magnons	14
2.2 Altermagnetism	15
2.2.1 Altermagnetic toy model	17
2.2.2 Introduction of DMI	19
2.3 Spin currents	19
2.4 Spin Seebeck effect	21
2.5 Spin Nernst effect	22
3 Methods of Simulation	25
3.1 Numerical solving of stochastic differential equations	25
3.2 Implementation of the spin system	27
3.3 Structure definition	27
3.4 Exchange files	30
3.5 Boundary conditions	31
3.6 Thermal models	32
3.7 Simulation output	32
3.7.1 Layer-wise magnetisation output	33
3.7.2 Spin configuration output	33
4 Results	35
4.1 Equilibrium properties	35
4.1.1 Introduction of a static magnetic field	35

4.1.2	Surface effects	40
4.2	Spin Seebeck effect	43
4.2.1	Introduction of a static magnetic field	43
	Magnon propagation length	47
4.2.2	Spin currents	49
4.3	Spin Nernst effect	51
4.3.1	Spin accumulation	51
4.3.2	Spin currents	53
4.3.3	Magnon spectra	54
4.4	Relativistic effects: Dzyaloshinskii-Moriya interaction	56
4.4.1	Equilibrium properties	56
4.4.2	Spin Seebeck effect	59
5	Conclusion and Outlook	63
	Acknowledgements	65
	References	67
	Tools Used	75
A	Derivations in regards to Magnons	77
A.1	Ground state of the ferromagnetic chain	77
A.2	Excitation of a single spin	78
A.3	Single magnon state	79
A.4	Extended Heisenberg model	81
B	Miscellaneous	83
B.1	Derivation of formulas for spin currents	83
B.2	Implementation of DMI	85
	Erklärung	87

List of Figures

2.1	Dzyaloshinskii-Moriya interaction	7
2.2	Landau-Lifshitz-Gilbert equation	8
2.3	Spin wave in a ferromagnetic chain	13
2.4	Antiferromagnetic magnon eigenmodes with opposite handedness . .	14
2.5	Comparison of ferro-, antiferro- and altermagnets	16
2.6	Schematic illustration of the toy model	18
2.7	Spin Nernst Effect	23
3.1	Structure definition of the conventional configuration	28
3.2	Structure definition of the tilted configuration	29
4.1	Equilibrium magnetization vs. magnetic field	36
4.2	Dispersion relations with and without magnetic field	38
4.3	Dispersion relation for negative and positive field	40
4.4	Spin configuration nontilted: boundaries	41
4.5	Spin configuration tilted: boundaries	42
4.6	SSE: Magnetization for different fields	44
4.7	SSE: Magnon accumulation for different fields	45
4.8	SSE: Magnetic profiles for different directions at $B > 0$	46
4.9	Propagation lengths	47
4.10	SSE: Peak magnon dependency on magnetic field	49
4.11	Longitudinal spin currents	50
4.12	Spin configuration with a temperature step	51
4.13	Transversal magnetization profiles	52
4.14	Transversal spin currents	53
4.15	Transversal magnon spectra	55
4.16	Spin components with DMI	56
4.17	Dispersion relations with and without DMI	58
4.18	Spin Seebeck effect with DMI: z-component	60
4.19	Spin Seebeck effect with DMI: y-component	61

List of Acronyms

- ABC** absorbing boundary condition. [31](#), [32](#), [43](#), [45](#), [49](#)
- AFM** antiferromagnet. [iii](#), [1](#), [5](#), [14–17](#), [22](#), [23](#), [27](#), [36](#), [37](#), [39](#), [46](#), [48](#), [52](#), [54](#), [59](#), [61](#), [63](#)
- AM** altermagnet. [iii](#), [1–3](#), [14–19](#), [22](#), [23](#), [30](#), [35](#), [44](#), [46](#), [51](#), [54](#), [56](#), [59](#), [63](#), [64](#), [86](#)
- API** application programming interface. [27](#), [75](#)
- BZ** Brillouin zone. [15](#), [56](#), [80](#)
- CPU** central processing unit. [27](#)
- DM** Dzyaloshinskii-Moriya. [vi](#), [6](#), [19](#), [30](#), [57](#), [58](#), [85](#)
- DMI** Dzyaloshinskii-Moriya interaction. [iii](#), [1](#), [5–7](#), [14](#), [19](#), [22](#), [23](#), [30](#), [31](#), [35](#), [56–61](#), [63](#), [64](#), [83](#), [85](#), [86](#)
- FM** ferromagnet. [iii](#), [1](#), [5](#), [9](#), [14–16](#), [20](#), [22](#), [39](#), [63](#)
- GPU** graphics processin unit. [27](#), [29](#), [75](#)
- IVP** initial value problem. [25](#), [26](#)
- LH** left-handed. [39](#), [44](#), [46](#), [60](#), [62](#)
- LHM** left-handed mode. [14](#), [15](#), [37](#), [39](#), [40](#), [44–46](#), [48](#), [50](#), [52](#), [54](#), [55](#), [59](#), [60](#)
- LLG** Landau-Lifshitz-Gilbert. [iii](#), [v](#), [3](#), [8](#), [9](#), [12](#), [13](#), [25–27](#), [32](#), [48](#), [63](#), [83](#)
- ODE** ordinary differential equation. [25](#)
- RH** right-handed. [39](#), [44–46](#), [62](#)
- RHM** right-handed mode. [14](#), [15](#), [37](#), [39](#), [40](#), [44](#), [47](#), [48](#), [52](#), [54–56](#), [59](#), [60](#)
- SDE** stochastic differential equation. [25–27](#)
- SL** sublattice. [14–22](#), [27](#), [28](#), [30](#), [31](#), [33](#), [35](#), [36](#), [39](#), [40](#), [42](#), [44–49](#), [52](#), [54](#), [56](#), [57](#), [59](#), [60](#), [62](#), [63](#), [83](#), [84](#), [86](#)
- SNE** spin Nernst effect. [iii](#), [1](#), [3](#), [19](#), [21–23](#), [32](#), [35](#), [40](#), [43](#), [51–54](#), [56](#), [63](#), [64](#)
- SSE** spin Seebeck effect. [iii](#), [1](#), [3](#), [19](#), [21](#), [22](#), [32](#), [35](#), [43–46](#), [49–54](#), [59–61](#), [63](#)
- TRS** time-reversal symmetry. [15](#)

Chapter 1

Introduction

Today, in the information age, information storage and processing are among the technological driving forces of progress. With the rise of artificial intelligence, the demand for efficient transmission and processing has further skyrocketed [1, 2]. This is where the field of spintronics plays a vital role [15].

The central idea of spintronics is to use electron *spin* as a carrier of information, in contrast to traditional electronics that rely solely on charge [3]. This can be achieved by integrating the spin degree of freedom into conventional charge-based devices or by designing systems that operate purely on spin. Collective spin excitations coined as spin waves or magnons can be used to transport information. This technology has the potential advantages of decreased power consumption, increased processing speed, and nonvolatility [3, 4]. Newly relevant research is for example being done in the area of spin based logic devices [16].

In the past, there has been a transition from ferromagnetic to antiferromagnetic spintronics [8]. In contrast to ferromagnets (FMs), antiferromagnets (AFMs) offer robustness against external perturbation and do not produce stray fields while displaying ultrafast dynamics [7, 8]. AFMs however, natively lack spin-polarized currents due to degenerate magnon bands and symmetry constraints.

In this environment, a third phase of magnetism termed altermagnetism provides advantages of both conventional classes of magnetic materials [8, 9]. It has been experimentally confirmed in 2024 [17]. Altermagnets (AMs) exhibit no net magnetization, have broken time reversal symmetry, exhibit nonrelativistic spin splitting and are characterized by distinct symmetry criteria [8–11]. A number of magnetic transport phenomena are expected to appear in AMs [8]. Due to its unique nature, AMs have already found its way into popular media [18–20].

In this work, an altermagnetic toy model is used to simulate spin dynamics in a simple AM, which aims to provide insight into fundamental characteristics. This can especially be useful in this new field with limited experimental data [17].

In a previous work [21], the equilibrium state and the spin Seebeck effect (SSE) have been studied. Here, an external magnetic field is introduced to further study its effect on the equilibrium state and transport mechanisms.

Additionally, a transversal transport phenomenon called spin Nernst effect (SNE) is analysed. This effect based on purely magnonic spin currents has not yet been conclusively observed experimentally [13, 14] but is expected in basic AMs [22, 23]. Thus, this work based on atomistic spin dynamics seeks to provide helpful insight into the effect.

Lastly, the relativistic, second order Dzyaloshinskii-Moriya interaction (DMI) is also considered in this work as it is present in many physical altermagnetic candidates.

Finally, this work pursues to contribute to the field of caloritronics — temperature-driven spintronics — by studying the effect of an external field on and different transport phenomena in a simple AM.

Chapter 2

Theory

This work is based on the computer simulation of magnetic materials, specifically magnons. In order to accurately describe and understand the underlying phenomena, it is necessary to first establish a theoretical basis.

This chapter will start by explaining why atoms exhibit magnetic moments and then introduce the extended Heisenberg model, which is based on the interaction of these magnetic moments. Then, the classical equation of motion for magnetic moments in a heat bath, the stochastic Landau-Lifshitz-Gilbert (LLG) equation is presented. For a fundamentally correct description, a quantum mechanical description of collective spin excitations is introduced.

After establishing the basis of solid state magnetism, the focus shifts to the alternating magnetic order and the specific implementation for this work. To complete this chapter, the spin Seebeck effect (SSE) and spin Nernst effect (SNE) are introduced, after providing theory regarding spin currents.

2.1 Solid state magnetism

Solid state physics is a branch of science concerning the structure and properties of solid materials [24]. Solid state magnetism specifically, treats fundamental principles responsible for magnetic properties of a solid structure [25].

2.1.1 Atomic magnetic moments

An isolated atom exhibits a certain magnetic moment. In a classical interpretation one imagines an electron with a certain angular momentum \vec{L} orbiting the nucleus which corresponds to an effective electric current I in a closed loop around a signed area \vec{A} . With that model, the magnetic moment of an atom with a single electron with mass m_e and charge $-e$ can be deducted to $\vec{\mu}_L = -\frac{e}{2m_e} \vec{L}$ by using the definition of the magnetic moment $\vec{m} = I \cdot \vec{A}$ [26].

This makes the existence of an atomic magnetic moment plausible. To be exact, at the scale of atoms, a quantum mechanical approach must be considered. For now, a hydrogen atom with a single electron is examined ignoring relativistic effects. For this central potential, the Schrödinger equation can be solved analytically, which is for example done in [27] or [28]. As a result, you get quantum numbers n , l and m_l which are used to describe the state of the electron in this atom. For example, the principal quantum number n describes the energy of the state. These quantum numbers are each in relation to eigenvalues of specific operators. Analogously to classical mechanics, the magnetic moment of a moving electron is in relation to the

angular momentum operator \hat{l} . When looking at an eigenstate $|\psi\rangle$, the eigenvalue $\hat{l}^2 = \hbar^2 l(l+1)$ ¹ can be used to obtain the amplitude of the magnetic moment

$$\left| \hat{\mu}_l \right| = \frac{e}{2m_e} \hbar \sqrt{l(l+1)} = \mu_B \sqrt{l(l+1)}, \quad (2.1)$$

where \hbar is the reduced Planck constant and μ_B is the Bohr magneton. Similarly $\hat{l}_z = \hbar m_l$ can be used to describe the projection $(\vec{\mu}_L)_z = \mu_B m_l$ along a specific direction z . The azimuthal quantum number l can assume values $0, 1, \dots, n-1$ and the magnetic quantum number m_l ranges from $m_l = -l$ to $m_l = +l$ in integer steps.

Furthermore, the intrinsic angular momentum called spin \hat{s} of the electron is considered. It causes a magnetic moment

$$\hat{\mu}_s = -g_e \frac{e}{2m_e} \hbar \cdot \hat{s} \quad (2.2)$$

where g_e is the Landé factor for an electron with the experimentally determined value of $g_e \approx 2.0023$ [29, 30].

For systems with more than one electron the situation becomes more complex because the electrons also interact with each other. It is possible to differentiate between two edge cases of angular momentum coupling. In the case of \vec{L} - \vec{S} coupling with weak spin-orbit interaction, the total angular momentum \hat{J} is constructed from the vector sum of the total orbital angular momentum and the total spin. The orbital contribution is given by $\hat{L} = \sum_i \hat{l}_i$ with magnitude $|\hat{L}| = \hbar \sqrt{L(L+1)}$, while the spin contribution is given by $\hat{S} = \sum_i \hat{s}_i$ with magnitude $|\hat{S}| = \hbar \sqrt{S(S+1)}$. Together they yield the total angular momentum $\hat{J} = \hat{L} + \hat{S}$. The total magnetic moment in that case is $\hat{\mu}_J = \hat{\mu}_L + \hat{\mu}_S$ [31]. Due to the Landé factor in eq. (2.2), $\hat{\mu}_J$ is not antiparallel to \hat{J} , instead there is a precession of $\hat{\mu}_J$ around \hat{J} [30, 32]. The component parallel to \hat{J} can be measured and is

$$\left| (\hat{\mu}_J)_J \right| = -g_J \mu_B \sqrt{J(J+1)} \quad (2.3)$$

with the system specific Landé-factor g_J and the total angular momentum quantum number J , which ranges from $(L-S)$ to $(L+S)$. The g-factor g_J can be calculated or determined empirically for different atoms and states [30, 32].

It has to be noted, that this coupling is an approximation which works for light atoms. Generally, even more quantities like the spin of the nucleus can be considered. In any case, the described properties illustrate the existence of an atomic magnetic moment. The interaction of these atomic magnetic moments causes a material to have specific magnetic properties.

The simulations performed for this thesis work with a set atomic magnetic moment dismissing its complicated origins. It is conventionally just called ‘spin’ [21]. This nomenclature is also implemented in this work.

¹Actually, the operator \hat{l} is not the same as the scalar on the right. To be correct, you could write $\hat{l}^2 |\psi\rangle = \hbar^2 l(l+1) |\psi\rangle$ when $|\psi\rangle$ refers to the corresponding eigenvector. This means, when the operator is applied to an eigenvector, it is the same as the eigenvalue multiplied by the eigenvector. Here, this rigour is often ignored to get the point across. Therefore, when one side of any equation in this subsection contains an operator and the other is scalar, one has to imagine the operator to be applied to appropriate eigenvectors

2.1.2 Extended Heisenberg model

The cause of magnetic properties of a system lie in the interaction between the atoms. In 1928, Heisenberg explained the origin of the direct exchange between electrons of neighbouring atoms by treating the Coulomb interaction with the Pauli principle between electrons of neighbouring atoms [33]. This corresponds to an overlap of the respective wave functions.

His idea builds the basis for the Heisenberg model [12, 24, 34, 35]. The foundation is the spin-dependent Hamiltonian

$$\mathcal{H}_{\text{exc}} = - \sum_{\langle ij \rangle} J_{ij} \vec{S}_i \cdot \vec{S}_j \quad (2.4)$$

for the exchange energy between the different atoms. In the exact quantum mechanical assessment, \mathcal{H}_{exc} and the spins $\vec{S}_{i,j}$ are operators. As briefly mentioned above in section 2.1.1, only certain directions for the spins are allowed in this case. Here, $\vec{S}_i := \frac{\vec{u}_i}{\mu_s}$ technically refers to a magnetic moment, which is normalized to unit length.

In the classical limit, \vec{S}_i is a vector which can point anywhere on the unit sphere [12]. The summation over $\langle ij \rangle$ refers to summing over all magnetic moments i and the atoms surrounding them j . This summation is frequently restricted to only a few nearest neighbours as the coupling energy J_{ij} often becomes negligible for atoms that are far away from each other. Regarding direct exchange, this is fairly straight forward. When only the nearest neighbours are considered, an exchange energy $J_{ij} > 0$ leads to a ferromagnetic (FM) order while a negative coupling constant causes anti-ferromagnetic (AFM) ordering if the lattice structure allows it [12].

It has to be noted, that there are also long ranged indirect interactions like the super-exchange or the RKKY² exchange [24, 35].

Beyond the exchange energy given in Eq. (2.4), additional terms contribute to the total energy [12, 29, 34]. The spins interact with an external magnetic field \vec{B} . This can be described with the Zeeman energy term

$$\mathcal{H}_B = -\mu_s \sum_i \vec{S}_i \cdot \vec{B}. \quad (2.5)$$

In absence of coupling between the atoms, this interaction causes the spins to align with the field, which is known as paramagnetism [12, 29].

Furthermore, the crystalline structure can create one or more preferred orientation of the spins. In the simplest case of uniaxial anisotropy

$$\mathcal{H}_{\text{ani}} = -d_z \sum_i (S_{iz})^2 \quad (2.6)$$

the spins prefer the z -axis as magnetic easy axis of the system with anisotropy constant $d_z > 0$ [12, 29]. In the case of $d_z < 0$ the spins prefer to be oriented in the easy plane perpendicular to the z -axis.

Additionally, the relativistic Dzyaloshinskii-Moriya interaction (DMI) is considered in this work.

²Ruderman-Kittel-Kasuya-Yosida

Dzyaloshinskii-Moriya interaction (DMI)

Surprisingly, the antiferromagnetic crystal called $\alpha\text{-Fe}_2\text{O}_3$ exhibits a spontaneous ‘weak’ magnetic moment in a certain state. Dzyaloshinskii explained this phenomenon phenomenologically with relativistic spin-lattice and magnetic dipole interactions within the crystal [36]. Later, Môriya expanded on his explanation and derived this antisymmetric spin coupling microscopically by extending the theory of superexchange to include spin-orbit coupling, which is also a relativistic effect [37]. This exchange is called Dzyaloshinskii-Moriya interaction (DMI) and the energy between two spins \vec{S}_i and \vec{S}_j can be expressed via

$$\mathcal{H}_{\text{DMI}}^{(ij)} = -\vec{D}_{ij} \cdot (\vec{S}_i \times \vec{S}_j) \quad (2.7)$$

where \vec{D}_{ij} is a constant vector describing the interaction, here named DM-vector.³ The total Hamiltonian can then be expressed as

$$\mathcal{H}_{\text{DMI}} = -\sum_{\langle ij \rangle} \vec{D}_{ij} \cdot (\vec{S}_i \times \vec{S}_j) = -\frac{1}{2} \sum_{i \neq j} \vec{D}_{ij} \cdot (\vec{S}_i \times \vec{S}_j) \quad (2.8)$$

where the sum represents a summation over neighbouring spins just like for Eq. (2.4). The factor $\frac{1}{2}$ is needed for the representation on the right because here every combination of spins are counted twice with $\vec{D}_{ij} = -\vec{D}_{ji}$ [35, 37].

In order to discuss symmetry, we take a look at Fig. 2.1a [34, 35]. The Hamiltonian must be invariant under every symmetry operation that fixes the bond midpoint and axis. Here, an inversion changes the role of the spins in Eq. (2.7). The Hamiltonian $\mathcal{H}_{\text{DMI}}^{(ij)}$ therefore changes sign, unless $\vec{D}_{ij} = 0$. Therefore, DMI requires a broken inversion symmetry.

Next, we take a look at Fig. 2.1b. Here, there is no inversion symmetry but a twofold rotation axis, which is orthogonal to the connecting line of the spins. When applying this rotation on \mathcal{H}_{DMI} , it can be concluded that \vec{D}_{ij} has to be in the plane perpendicular to the axis of rotation. Further considerations of symmetry give the direction [34].

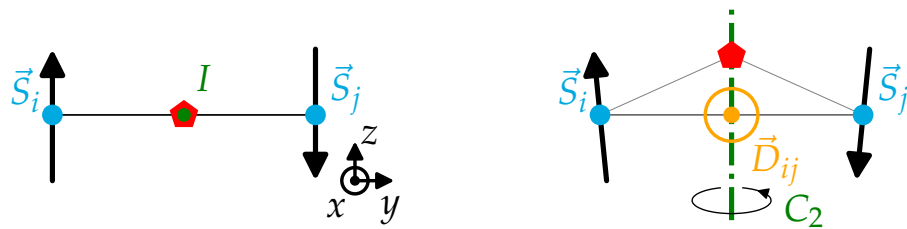
Physically, electron spins on sites without inversion symmetry minimize the energy by tilting out of the collinear antiferromagnetic order, becoming slightly noncollinear. This canting is generally small as it has to compete with the Heisenberg exchange term (2.4), but it does create small magnetic moment [34, 35]. The implementation for this work is presented in Sec. 2.2.2, where an easy axis in z -direction and a DM-vector in x -direction results in canting along the $-y$ -direction.

To describe the system as a whole, the different Hamiltonians are then added up to

$$\mathcal{H} = \mathcal{H}_{\text{exc}} + \mathcal{H}_{\text{ani}} + \mathcal{H}_{\text{B}} + \mathcal{H}_{\text{DMI}} . \quad (2.9)$$

Generally, the extended Heisenberg model used in this thesis can of course be expanded by adding more energy terms from different physical origins.

³The sign convention originally introduced by Môriya [37] is without a preceding minus sign. For consistency with Eq. (2.4), we introduce it here.



(a) The red atom is in the centre between the two spins creating an inversion centre I .
(b) Here, there is no inversion centre but there is a two-fold axis of rotation C_2 .

Figure 2.1: Illustration of symmetry properties of the Dzyaloshinskii-Moriya interaction. Further description in the text. Graphics inspired from figure 12.13 in [34]. The x -axis and the \vec{D}_{ij} -vector are pointing out of plane.

2.1.3 Stochastic Landau-Lifshitz-Gilbert equation

The Heisenberg model can be used to determine equilibrium properties by, for example, taking the canonical ensemble. When wanting to calculate non-equilibrium properties, an equation of motion has to be found [12].

Ignoring damping, the motion of a spin \vec{S}_i in a spin system can be described by the Landau-Lifshitz equation [38] without damping

$$\frac{d\vec{S}_i(t)}{dt} = -\frac{\gamma}{\mu_s} \vec{S}_i(t) \times \vec{H}_i(t) \quad (2.10)$$

where $\vec{S}_i := \vec{\mu}_i / \mu_s$ still is normalized to unit length, $\vec{H}_i := -\partial\mathcal{H}/\partial\vec{S}_i$ is the effective magnetic field (in energy units) at the lattice point i and $\gamma = g_e\mu_B/\hbar$ is the gyromagnetic ratio of an electron, which is defined as the absolute value of the ratio between the magnetic moment to the angular momentum of the particle [29, 34, 39]. The equation can partially derived quantum mechanically, even though it is a classical equation [34, 39]. In his dissertation, Evers explains that, even though it is a classical equation, it is a ‘quite accurate description’ [39]. The relationship between the quantum mechanical model described below and the classical description is also discussed again in Sec. 2.1.4.

Equation (2.10) effectively sets the movement of spin i in relation to the orientation of the other spins, as the effective field is the derivative

$$\vec{H}_i := -\frac{\partial\mathcal{H}}{\partial\vec{S}_i} \quad (2.11)$$

of the Hamiltonian \mathcal{H} [39]. According to the Heisenberg model introduced in Sec. 2.1.2, the Hamiltonian \mathcal{H} depends explicitly on all spin degrees of freedom. Equation (2.10) describes an infinite precession around the effective field \vec{H}_i [34].

In practice, an infinite precession is unrealistic, as there are energy losses due to damping in the spin system, for example because of interactions with the lattice [29, 39]. As per the complex origin of damping, a phenomenological damping term is introduced, which tries to return the spins towards their ground state. For that

purpose, Gilbert [40] proposed the ansatz

$$\frac{d\vec{S}_i}{dt} = -\frac{\gamma}{\mu_s} \vec{S}_i \times \vec{H}_i + \alpha \vec{S}_i \times \frac{d\vec{S}_i}{dt} \quad (2.12)$$

with the Gilbert damping parameter α . This equation applies a torque proportional to the rate of change of the spin, pushing it into its ground state [39]. When solving for the time derivative of \vec{S}_i , the result is the Landau-Lifshitz-Gilbert (LLG) equation

$$\frac{d\vec{S}_i}{dt} = -\frac{\gamma}{\mu_s(1+\alpha^2)} \vec{S}_i \times (\vec{H}_i(t) + \alpha \vec{S}_i \times \vec{H}_i(t)) \quad (2.13)$$

[12]. The torques applied to a single spin as described above are shown schematically in Fig. 2.2.

When describing a system using the LLG Eq. (2.13) starting in an excited state, the spins would just return to their respective ground state with the passing of time because of the damping. For a finite temperature this behaviour is not realistic, which is why a thermal noise term $\vec{\xi}_i(t)$ is introduced. The effective field is redefined by adding this term

$$\vec{H}_i := -\frac{\partial \mathcal{H}}{\partial \vec{S}_i} + \vec{\xi}_i(t) \quad (2.14)$$

and inserting it into (2.13) leading to the stochastic Landau-Lifshitz-Gilbert equation [12]. The simplest implementation of noise is (Gaussian) white noise, which is

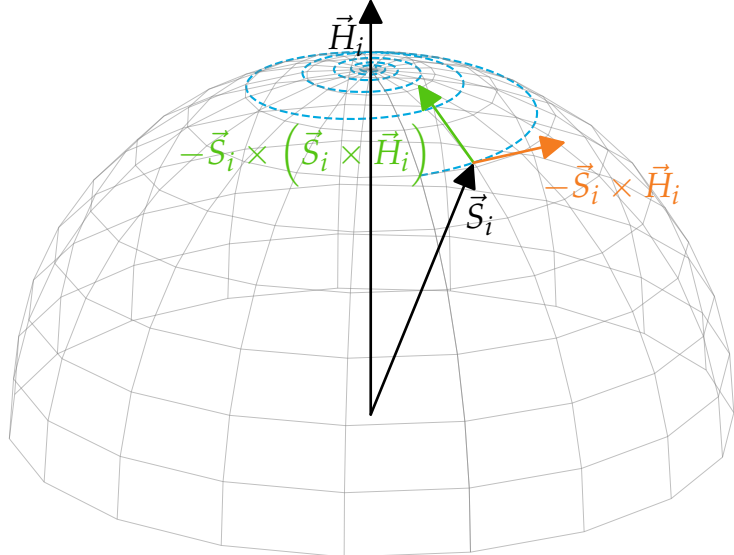


Figure 2.2: Qualitative diagram of the trajectory and torques acting on an excited spin \vec{S}_i according to the LLG (2.13). The precession is caused by the torque $-\vec{S}_i \times \vec{H}_i$ (orange) and the damping is proportional to $-\vec{S}_i \times (\vec{S}_i \times \vec{H}_i)$ (green) pushing \vec{S}_i into its ground state.

uncorrelated in space and time. Its properties can be written as

$$\langle \vec{\xi}_i(t) \rangle = 0 \quad (2.15)$$

$$\langle \xi_i^\eta(t) \xi_j^\theta(t') \rangle = 2\alpha k_B T \frac{\mu_s}{\gamma} \delta_{ij} \delta_{\eta\theta} \delta(t - t') \quad (2.16)$$

with the Boltzmann constant k_B , the temperature T and the average $\langle \cdot \rangle$ over different stochastic paths $\vec{\xi}(t)$. Here i and j still denote the lattice point and $\eta, \theta \in \{x, y, z\}$ the Cartesian components of $\vec{\xi}_{i,j}$ [12, 39].

The inclusion of thermal noise (2.14) leads to stochastic fluctuations in the effective field, resulting in a noisy trajectory and sustained spin precession even at long times, in contrast to what is shown in Fig. 2.2 without noise.

This assumption of uncorrelated noise is a simplification but the definition of noise in Eq. (2.16) guarantees correct thermal averages. The Gilbert damping parameter α describes the coupling strength of the heat bath and thermal fluctuations, which depend linearly on α and T . As a stochastic differential equation, the stochastic LLG equation produces different trajectories from identical starting conditions. Therefore, to describe the system in a correct manner, thermal averages have to be taken [12].

2.1.4 Magnons

At temperature $T = 0$, a ferromagnet is completely ordered. For a finite temperature, the order is disturbed by excitations called spin waves [25].

This section discusses spin waves and their quantized form, magnons, which is essential for understanding the physics of spin dynamics.

Here, the quantum mechanical derivation of spin waves, which provides a fundamentally correct basis for their description, is presented. While the semi-classical approach based on the classical LLG equation yields correct results and is widely used as a heuristic treatment (see e.g. [25, 29, 34]), only the quantum mechanical study captures the underlying physics from first principles. The following exposition is largely based on the dissertation by Martin Evers, where the derivation is presented with greater mathematical rigour and detail [39]. The connection to classical spin dynamics is discussed subsequently.

To get a general grasp of the concept of magnons, a ferromagnetic chain of spins $\hat{S}_1, \dots, \hat{S}_N$ with periodic boundary conditions $\hat{S}_{N+1} = \hat{S}_1$ is treated. The spins are placed at positions $r_l = l \cdot a$ where l is the integer-index of the spin and a is the lattice constant.

It has to be noted that we are working with operators which act as observables instead of simple variables in this quantum mechanical approach. We therefore go from the classical spin \vec{S} to the spin-operator \hat{S} . Furthermore, we refrain from working with spins which are normalized to unit length in contrast to section 2.1.2, where the Heisenberg Model was introduced, as the notation would become quite cumbersome. To keep the interaction constants to be in dimension of energy anyway, we instead normalize with \hbar , which is the smallest quantity of angular momentum. Now, the exchange constants in the classical and quantum mechanical view only differ by a dimensionless factor, which is not relevant to understand the concept of magnons.

We now insert the spin-operators into the Heisenberg Model. To keep it simple, here, we only focus on the exchange interaction (2.4). Furthermore, only nearest neighbour interactions are considered which are all assumed to be equal ($J_{l,l+1} = J$). The Hamiltonian then is

$$\hat{\mathcal{H}} = -J \sum_{l=1}^N \hat{\vec{S}}_l \cdot \hat{\vec{S}}_{l+1} \quad (2.17)$$

for the simple periodic chain. As we are working with a ferromagnetic chain, the spins are parallel and $J > 0$ [25, 39].

Before continuing, the properties of a single spin operator $\hat{S} := \hat{S}_l$ are summarized. The origin of these magnetic moments has been topic of Sec. 2.1.1, where quantum numbers were also introduced. We use z as the quantization axis. With the quantum numbers S and M , and the eigenstate $|\varphi\rangle$, the spin operators \hat{S} then obey⁴

$$\hat{S}^2 |\varphi\rangle = S(S+1) |\varphi\rangle \quad (2.18)$$

$$\text{and } \hat{S}^z |\varphi\rangle = M |\varphi\rangle \quad (2.19)$$

which is also why we can describe the eigenstate by $|\varphi\rangle = |S, M\rangle$ [31]. Here, $M \in \{-S, -S+1, \dots, S\}$, which means, a single spin has $2S+1$ states.

Furthermore, we denote the commutation relations⁴

$$[\hat{S}_k^x, \hat{S}_l^y] = i\delta_{kl}\hat{S}_k^z \quad \text{and cyclical} \quad (2.20)$$

$$\Rightarrow [\hat{\mathcal{H}}, \hat{S}^\eta] = 0 \quad \eta \in \{x, y, z\} \quad (2.21)$$

from which follows that our Hamiltonian (2.17) is compatible with the spin operators sharing their eigenvectors [31, 41].

Lastly, we define the ladder operators

$$\hat{S}^\pm = \hat{S}^x \pm i\hat{S}^y \quad (2.22)$$

which make the system jump from a state with M to one with $M \pm 1$ [31, 39, 41]:⁴

$$\hat{S}^\pm |S, M\rangle = \sqrt{S(S+1) - M(M \pm 1)} |S, M \pm 1\rangle \quad (2.23)$$

$$\hat{S}^+ |S, M = +S\rangle = 0, \quad \hat{S}^- |S, M = -S\rangle = 0 \quad (2.24)$$

Now, we come back to describing the ferromagnetic chain. We assume each spin to have same amplitude and therefore $\hat{S} := \hat{S}_l$. Then the state of the entire system $|\psi\rangle$ can be formulated as

$$|\psi\rangle := |M_1, M_2, \dots, M_N\rangle . \quad (2.25)$$

⁴ Many definitions include a factor \hbar here. We have defined \hat{S} as normalized by that factor in order to keep J in dimension of energy.

Next, we rewrite the Hamiltonian (2.17) to

$$\begin{aligned}\hat{\mathcal{H}} &= -J \sum_l (\hat{S}_l^x \hat{S}_{l+1}^x + \hat{S}_l^y \hat{S}_{l+1}^y + \hat{S}_l^z \hat{S}_{l+1}^z) \\ &= -J \sum_l \left[\frac{1}{2} (\hat{S}_l^+ \hat{S}_{l+1}^- + \hat{S}_l^- \hat{S}_{l+1}^+) + \hat{S}_l^z \hat{S}_{l+1}^z \right]\end{aligned}\quad (2.26)$$

using the ladder operators [25, 35, 39, 41]. Here, \hat{S}_l^\pm changes the value of M_l , when applied to $|\psi\rangle$. The derivation of (2.26) can be found in [21, 39].

The intuitive ground state is all spins pointing along the same direction. Here, we use z as quantization axis, so we choose all spins pointing downwards. This state has minimum energy. It can be written as

$$|\psi_0\rangle := | -s, \dots, -s \rangle . \quad (2.27)$$

As $\hat{S}_l^- | -s, \dots, -s \rangle = 0$ for all l , it is obvious that $|\psi_0\rangle$ is an eigenstate of $\hat{\mathcal{H}}$. By taking the expectation value $\langle \psi | \hat{\mathcal{H}} | \psi \rangle$ it also becomes clear that $|\psi_0\rangle$ is the lowest energy state of the system with

$$E_0 := \langle \psi_0 | \hat{\mathcal{H}} | \psi_0 \rangle = -JNS^2 \quad (2.28)$$

[39, 41].⁴ Both is again explicitly shown in appendix A.1.

The intuitive approach to an excited state is to increase the magnetic quantum number M of a single spin by one. We define

$$|n\rangle := |M_1, \dots, M_{n-1}, M_n, M_{n+1}, \dots, M_N\rangle = | -S, \dots, -S, -S+1, -S, \dots, -S \rangle \quad (2.29)$$

where the angular momentum of the n -th spin is excited by $1\hbar$ [39]. Surprisingly, this state is not an eigenstate of the Hamiltonian. We calculate

$$\hat{\mathcal{H}} |n\rangle = -J (S |n-1\rangle + S |n+1\rangle + (NS^2 - 2S) |n\rangle) \quad (2.30)$$

in the appendix A.2 and see clearly, that $|n\rangle$ is not an eigenvector.

In search for the first excited state, the Fourier-transform

$$|k\rangle := \frac{1}{\sqrt{N}} \sum_n e^{ikna} |n\rangle \quad (2.31)$$

parameterized by the wave vector k is taken. It is in compliance with the translational symmetry with respect to the lattice constant a and represents a smeared out spin excitation [25, 35, 39].

As proved in the appendix A.3, $|k\rangle$ is an eigenstate of the Hamiltonian (2.17). It has the eigenvalue

$$\hat{\mathcal{H}} |k\rangle = E(k) |k\rangle = E_0 + \hbar\omega(k) \quad (2.32)$$

where

$$\omega(k) = \frac{JS}{\hbar} (2 - 2 \cos(ka)) \quad (2.33)$$

is the dispersion relation for single-magnon states in a periodic, ferromagnetic chain.

The wave vector k takes discrete values, which is shown in the appendix A.3. This dispersion relation has also already been found by Bloch in 1930 [42].

By calculating the expectation value $\langle k | \hat{S}_l^z | k \rangle$, we see the angular momentum of each spin deviates by \hbar/N from the ground state. The collective one-magnon-state $|k\rangle$ is a deviation of the system by $1\hbar$ spread over all N lattice points. Because of its collective nature, this elementary excitation is called spin wave since it behaves very much like a plane wave. As both the energy of a spin wave $\hbar\omega(k)$ and its angular momentum are quantized, they are also called magnons which can be compared to the quasi particles of lattice vibration called phonons. Because of their integer quantization, magnons are bosons [35, 39, 41].

A semiclassical representation of the results is shown in the following section.

When handling more-dimensional structures, the dispersion relation is calculated as a sum $\omega \propto \sum_l (1 - \cos(\vec{k} \cdot \vec{r}_l))$ over all lattice vectors r_l which connect the treated atom to its neighbours [34].

Relation to classic spin models

Because the simulations performed for this thesis are based on a classical model, it is essential to discuss the connection between the quantum mechanical and the classical model [39].

For that, the quantum mechanical dynamics are replaced by the Landau-Lifshitz-Gilbert (LLG) equation and the operators are replaced by variables containing their expectation values.

Spin waves in the classical model are described with an amplitude S_l at position r_l for the ferromagnetic chain above by

$$S_l := S_l^x + iS_l^y = |S_l| e^{i\varphi_l} \quad (2.34)$$

which represents the in-plane component of the spin at index l with its phase of oscillation φ_l [39].

Therefore, in the semiclassical vector model, the spin wave derived above can be understood as N spins precessing with a phase shift to each other defined by the wave vector k . A single spin \vec{S}_l with the length $\hbar S$ precesses around the z -axis where its projection on it is $\hbar(-S + 1/N)$. This collective movement describes a plane wave [41]. It is schematically shown in Fig. 2.3.

The amplitude of the spin wave can also be Fourier transformed into momentum space

$$\tilde{S}_{\vec{k}} = \frac{1}{\sqrt{N}} \sum_{n=1}^N S_n e^{-i\vec{k}\vec{r}_n} \quad (2.35)$$

and the time evolution of the system without damping or magnon-magnon interactions then is

$$\tilde{S}_{\vec{k}}(t) = \tilde{S}_{\vec{k}}(t=0) \cdot e^{i\omega(\vec{k})t} \quad (2.36)$$

with the initial condition $\tilde{S}_{\vec{k}}(t=0)$ and the dispersion relation $\omega(\vec{k})$. In the classical limit, this dispersion relation is the same as the quantum mechanical one. This is shown in detail in chapter II.2.2.3. in [39]. Here, the classical limit corresponds to

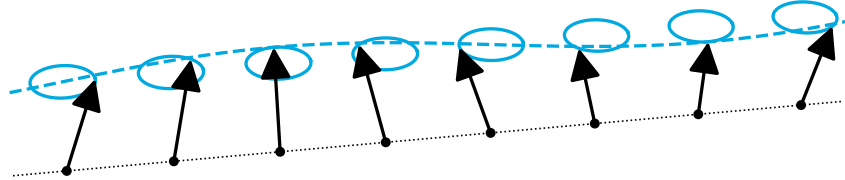


Figure 2.3: Illustration of a spin wave in a ferromagnetic chain (semiclassical vector model).

$S \rightarrow \infty$, which causes the number of quantum levels of M to become large enough to interpret it as continuous. By $S \rightarrow \infty$, we mean that we have large atomic magnetic moment μ_S .

Classical spin waves act similar to quantum mechanical ones in many ways. The obvious difference is that the quantities that were discrete before are continuous in the classical model. As we have seen, with a large number of spins, this difference continues to become negligible.

Furthermore, the occupation of magnon states differ between the quantum mechanical and the classical model. In the quantum mechanical case, a Bose-Einstein distribution

$$\langle n_{\vec{k}} \rangle^{\text{qm}} = \frac{1}{\exp\left(\frac{\hbar\omega}{k_B T}\right) - 1} \quad (2.37)$$

describes the occupation number of magnons with wave vector \vec{k} in thermal equilibrium. Here, k_B is the Boltzmann-constant and T is the temperature [25, 29, 34, 41]. In contrast to that, in the classical model using the LLG equation, the occupation number of the magnon states is given by the Rayleigh-Jeans distribution

$$\langle n_{\vec{k}} \rangle^{\text{cl}} = \frac{k_B T}{\hbar\omega}. \quad (2.38)$$

This dissimilarity causes the magnetization to not be well modelled classically at very low temperatures, while still being accurate up to the critical temperature T_C , where ferromagnetic materials become paramagnetic. At low temperatures, the slope of the magnetization is flat in quantum mechanical models, while the classical model shows a linear decrease [29, 39].

Surprisingly, in contrast to the wrong low-temperature modelling of the magnetization, zero temperature can be handled classically without error, as long as non-linear contributions to the Hamiltonian are small [39].

Even though the classical model fails in regard of the thermal occupation at low (non-zero) temperatures causing wrong predictions for e.g. the magnetization, it is still applicable for this work. This is because the classical model can still be a very useful tool for dynamics in this low-temperature regime, especially when thermal effects are minor and therefore the amplitude of spin waves is small [21, 29, 39].

Especially advantageous is the fact, that the classical model allows numerical treatment of a very large number of spins (up to 10^8), while this is not possible for full quantum systems [39].

Antiferromagnetic magnons

The introduction to this section was done with a ferromagnet because of the straightforward calculations and the simplicity. As this work is about a model for an alter-magnet (AM), which is described in section 2.2, a very small introduction to a similar type of magnet is presented here: an antiferromagnet (AFM)

Antiferromagnets are often described in terms of sublattices (SLs), where each sub-lattice contains spins aligned in the same direction: spins are aligned parallel within a SL (intra-SL), but antiparallel between different SLs (inter-SL). With the Heisenberg model (2.4), this can be achieved with a negative exchange interaction [43].

A quantum formulation of magnons in AFMs can be found in [43].

As it turns out, magnons have different properties in AFMs compared to FMs. The main difference is the chirality of magnons. Ferromagnetic magnons always have right-handed chirality and carry a spin angular momentum reducing the ground-state ordering. Antiferromagnetic magnons on the other hand have two distinct eigenmodes which carry opposite angular momentum. These are illustrated for a collinear easy-axis AFM in Fig. 2.4 and titled α for the right-handed mode (RHM) and β for the left-handed mode (LHM) [43, 44]. The RHM refers to a counterclockwise precession, when looking from above. Spin canting, for example because of DMI, qualitatively does not affect the oscillation of the magnetic moments except for the oscillation becoming elliptical [44].

This gives antiferromagnetic magnons a polarization-like degree of freedom in contrast to ferromagnets [39] and gives them the ability to carry magnetization with different signs.

The ratio of the in-plane magnetization amplitudes of the up and down spin differs for both modes, depending on the exchange and the easy-axis anisotropy energy [43]. In the α -mode, the precession amplitude of the up spin is larger as visible in Fig. 2.4, in contrast to the β -mode. Therefore, the RHM (α) carries negative angular momentum. The dispersion relation of both magnon modes in one-dimensional AFMs is qualitatively proportional to $|\sin(ka)|$ with the wave vector k and the lattice constant a [34].

The easy-axis anisotropy smooths the dispersion relation near the Γ -point ($k = 0$)

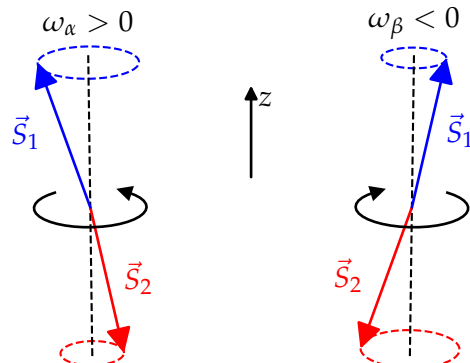


Figure 2.4: Illustration of the precession of magnon eigenmodes in collinear easy-axis antiferromagnets. The RHM (α) precesses in opposite direction compared to the LHM (β). The anisotropy is along the z -axis.

creating a band gap and a minimum energy required for ($k = 0$)-magnons. Furthermore, both magnon modes $\omega_\alpha(k)$ and $\omega_\beta(k)$ are degenerate without an external magnetic field. We can define $\omega_\alpha > 0$ and $\omega_\beta < 0$ with respective energies $\hbar |\omega_{\alpha,\beta}|$. When introducing a (constant) magnetic field along the easy-axis (+z-direction) with its respective Zeeman term (2.5), the degeneracy is lifted: The frequency of the RHM ω_α shifts up by $\mu_s B$ while the absolute value of the frequency of the LHM ω_β shifts down [43, 45, 46].

Lastly, it will be mentioned, that thermally driven AFM magnons are incoherent [44]. This means that both magnon modes are excited by a temperature bath.

2.2 Altermagnetism

Different materials can broadly be classified by their microscopic reaction to an external magnetic field. In diamagnetic and paramagnetic bodies, there is no spontaneous order without an external field but they react to one by inducing or aligning magnetic moments (anti-)parallel to the field [34].

In contrast, there are materials with a spontaneous magnetic order below a specific temperature, which can be called ‘magnetic’ [47]. In a simple ferromagnet (FM), magnetic moments are ideally aligned parallel or at least all have a component in the same direction. Therefore, FMs have a finite magnetization, at least within domains [34, 48]. In the Heisenberg model (2.4), this behaviour occurs when the nearest-neighbour exchange interaction is $J > 0$.

Furthermore, there are ferrimagnetic materials which have a finite magnetization, but not all magnetic moments have a component in the same direction [34]. They behave similar to ferromagnets in many aspects [43].

In antiferromagnets (AFM), spins are ordered but have total magnetization of zero. Often, AFMs are described with sublattices (SLs) encompassing spins aligned in the same direction. Then the intra-sublattice exchange is positive while the inter-sublattice exchange is negative [43]. With the magnetic moments \vec{S}_A and \vec{S}_B for each sublattice, collinear AFMs can be described using the Néel vector as an order parameter. It is defined as

$$\vec{n} = \frac{\vec{S}_A - \vec{S}_B}{2} \quad (2.39)$$

and quantifies the antiparallel orientation of the spins [44].

Recently, a new distinct magnetic phase has been proposed, reconciling apparently contradicting FM- and AFM-type phenomena in materials [9]. This distinct class of collinear magnets has been termed altermagnet (AM) and has net zero magnetization. It is characterized by its alternating non-relativistic spin-splitting of the electron band structure and broken time-reversal symmetry (TRS) [8, 9, 47]. A comparative table of known phenomenological similarities and differences between AMs, FMs and AFMs can be found in Ref. [47].

One differentiating aspect of AMs is the anisotropic spin density in real space. FMs and AFMs have isotropic spin densities on the other hand as can be seen in Fig. 2.5(a). As a result, the spin splitting in momentum space is also anisotropic and the spin-split Fermi surfaces remind of a *d*-, *g*- or *i*-wave parity. The alternating sign of the spin polarization across the Brillouin zone (BZ) is where altermagnets get

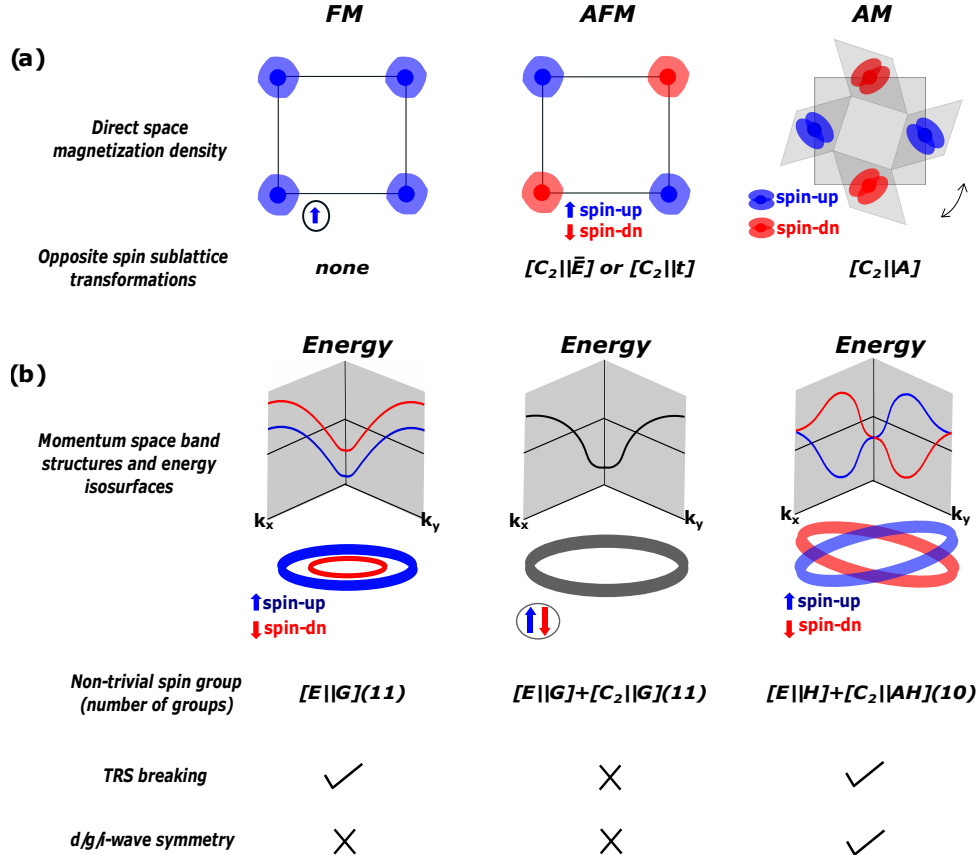


Figure 2.5: (a) Representational comparison of spin densities in real space: FMs and AFMs have isotropic spin densities while AMs have anisotropic spin densities. The colours represent up and down spin. The double-headed arrow indicates the symmetry operation between the SLs which is $[C_2]||C_{4z}t]$ here. This is short for a twofold rotational symmetry in spin space and a fourfold real-space rotation (nonsymmorphic with translation labelled by t) [9]. (b) Comparison of the electronic band structures with the iso-surfaces below the diagrams. FMs have constant spin-splitting in the momentum space and AFMs have no splitting. The electronic structure of AMs show alternating spin-splitting.
This figure is reproduced from Refs. [9, 10] as it appears in [8], and is licensed under the Creative Commons Attribution 4.0 International License (available at <https://creativecommons.org/licenses/by/4.0/>).

their name from. The corresponding model band structures of AMs, FMs and AFMs can be found in Fig. 2.5 (b) [8, 9].

To distinguish the three distinct phases of collinear magnetism, a spin symmetry classification is considered. In this nonrelativistic spin group description, $[R_i||R_j]$ denotes a transformation R_i which only acts in spin space and a decoupled transformation R_j which only acts in real space. A complete description of the three phases and its associated symmetry operations can be found in Ref. [9]. To summarize, the three phases of collinear magnetism can be described as follows: The ferromagnetic phase has one spin lattice or opposite-spin sublattices not connected by any symmetry transformation. The antiferromagnetic phase has its opposite-spin sublattices connected by translation or inversion. Lastly, the altermagnetic phase has opposite-spin sublattices connected by rotation (proper or improper and symmorphic or nonsymmorphic). Here, the sublattices are specifically not connected by translation or inversion [9].

Šmejkal et al. [9] proposed a set of criteria and an algorithm to identify AMs. The criteria are [8, 9]:

- The number of magnetic atoms in a unit cell is even.
- There is no inversion center between the magnetic atoms with opposite spin.
- The opposite-spin SLs are surrounded by different arrangements of neighbouring atoms. This structural inequivalence means that the magnetic anisotropy of each SL's local atomic motif cannot be transformed into that of the other by any crystal symmetry.
- The opposite-spin SLs are connected by rotation (in spin and real spaces), possibly combined with translation or inversion symmetry, mirror, glide, or screw.

There are a wide range of materials which can intrinsically exhibit altermagnetism [8, 9].

Lastly, we will make a few remarks about magnons. In AFMs, the degeneracy of opposite-chirality magnons, which have been introduced in Sec. 2.1.4, is protected because of the translation or inversion symmetry. In AMs these symmetries are broken, and analogous to the electronic band structure, the degeneracy of magnons band with opposite chirality is expected to be lifted [9]. This has also been observed by Rabea Schmidhuber [21] in the model used for this bachelor's thesis which is presented in the following section.

2.2.1 Altermagnetic toy model

In the following, the toy model, which is used to model altermagnetic properties for this work is described. Developed in collaboration with the HUN-REN Wigner Research Centre for Physics, it was used in Schmidhuber's bachelor's thesis [21] before, although the directional dependence of the exchanges has been slightly adjusted to correct a discrepancy in her work.

The configuration can schematically be seen in Fig. 2.6. The model consists of a two-dimensional square lattice with two distinct sublattices (SLs). They are labelled as 'A' and 'B' and are colour-coded blue and red respectively. In each unit cell, there are a total of two atoms, each of which is assigned to a sublattice (SL). They are located at $\vec{r}_A = a \begin{pmatrix} 0 \\ 0 \end{pmatrix}$ and $\vec{r}_B = a \begin{pmatrix} 1 \\ 0 \end{pmatrix}$ in the unit cell.

Both atoms are magnetic and have a magnetic moment (spin). At zero temperature in the ground state, the spins of the two sublattices are oriented antiparallel to each other. Atoms in SL A have spins pointing along the $+z$ -axis and atoms in SL B have spins aligned along $-z$.

The primitive translation vectors of the lattice in direct space are defined as

$$\vec{a}_1 = a \begin{pmatrix} 1 \\ 1 \end{pmatrix} \quad \text{and} \quad \vec{a}_2 = a \begin{pmatrix} 1 \\ -1 \end{pmatrix} \quad (2.40)$$

and can also be seen in Fig. 2.6. Furthermore, the unit cell in the form of the Wigner-Seitz cell is shown. One can clearly see that the chosen definitions of the translation vectors and the unit cell define the whole lattice [34].

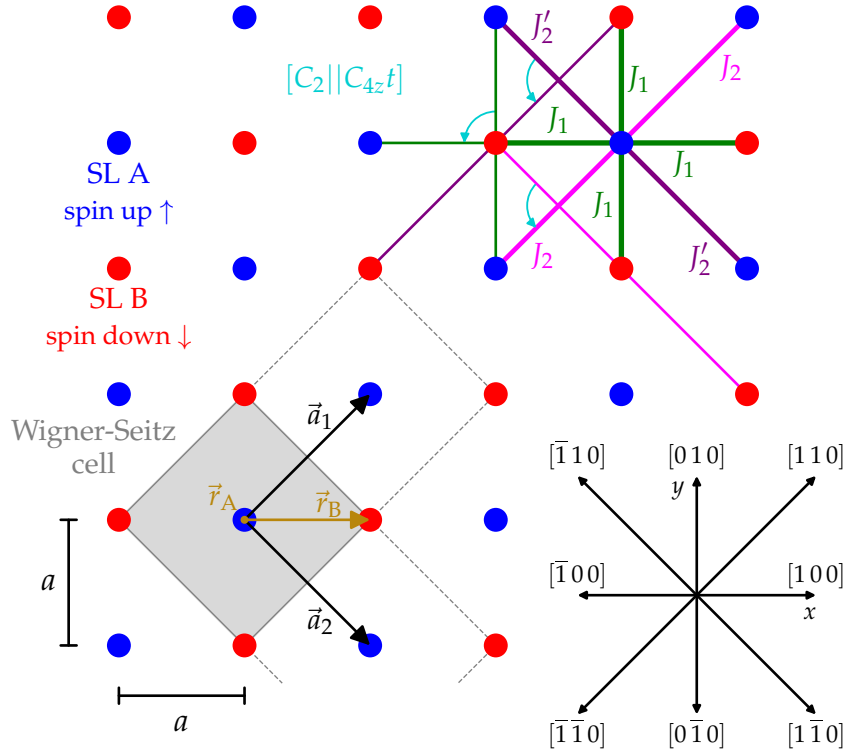


Figure 2.6: Schematic depiction of the AM toy model on a two-dimensional square lattice, which was used for this work. Each lattice point is indicated by a dot which is either blue or red depending on the SL. On the left bottom corner, the primitive translation vectors and the locations of the atoms within each Wigner-Seitz unit cell are shown. On the bottom right, the crystallographic directions, which will be used in this work are indicated. The exchange interactions are suggested in the top right corner. The exchange interaction J_1 acts between nearest neighbors of different SLs. Beware of different intra-SL exchange interactions along the diagonal directions. Along direction $[1\bar{1}0]$, exchange energy J_2 is relevant for SL B, and J'_2 dictates interactions for SL A. In the $[110]$ direction, this behaviour is reversed with exchange energy J_2 determining interactions for SL A. Lastly, the symmetry is indicated in cyan as described in Sec. 2.2.

The corresponding reciprocal lattice vectors are given by

$$\vec{b}_1 = \frac{\pi}{a} \begin{pmatrix} 1 \\ 1 \end{pmatrix} \quad \text{and} \quad \vec{b}_2 = \frac{\pi}{a} \begin{pmatrix} 1 \\ -1 \end{pmatrix}. \quad (2.41)$$

The exchange interactions between the different atoms along different directions can also be seen in Fig. 2.6. Each atom interacts with four atoms of different sublattices with exchange energy J_1 . Interesting about this model are the two distinct exchange interactions J_2 and J'_2 , which are reversed in SL B compared to SL A.

With this exchange geometry, one finds $[C_2 || C_{4z}t]$ to describe the symmetry of the configuration. This is indicated in cyan in Fig. 2.6. If the spins are rotated by 180° and there is a fourfold rotation along the z-axis in real space with an added translation, the configuration stays the same. There is no inversion centre and the number of magnetic atoms in a unit cell is even. According to the criteria from previous Sec. 2.2, this shows that the utilized model indeed is an altermagnet. This has also been confirmed by the properties of the dispersion relation for this model [21].

2.2.2 Introduction of DMI

This work furthermore studies the relativistic Dzyaloshinskii-Moriya interaction (DMI), which was introduced in section 2.1.2. We institute nearest-neighbour DMI, i.e. the DM-vector is only nonzero for nearest neighbours. In the presented model in Fig. 2.6, this corresponds to a vector $\vec{D}_{A,B}$ where the subscript refers to the interaction between two neighbouring spins with SL A and SL B. As introduced in (2.7), the Hamiltonian for this interaction then is

$$\mathcal{H}_{\text{DMI}}^{A,B} = -\vec{D}_{A,B} \cdot (\vec{S}_A \times \vec{S}_B) . \quad (2.42)$$

We define the DM-vector

$$\vec{D}_{A,B} := \begin{pmatrix} D \\ 0 \\ 0 \end{pmatrix} \quad (2.43)$$

for this model to point in x -direction, where D is its constant length. Conversely, $\vec{D}_{A,B} = -\vec{D}_{B,A}$ applies as explained in Sec. 2.1.2. This implementation is in accordance with that shown in Fig. 2.1b with DM-vector in x -, and canting in the $-y$ -direction to minimize the energy of the Hamiltonian.

During the creation of this work, communications with Levente Rózsa⁵ revealed that this implementation destroys the altermagnetic symmetry. This becomes apparent when considering the symmetry operation $[C_2||C_{4z}t]$. If we apply the real space rotation of the DM-vector by 90° , we obtain $(0 \ D \ 0)^T$ which only contains a component in the y -direction. Consequently, the DM-vector is not invariant under this rotation, even when including the translational part of the operation, which can only introduce a sign change here.

As an additional example, consider a two-fold rotational symmetry in real space. In this case, only the sign of the DM-vector changes; however, this transformation would contradict the spin-space rotational symmetry C_2 . In summary, an analysis of this toy model reveals that there is no implementation of canting-inducing DMI that remains consistent with the altermagnetic symmetry.

A recent, yet unpublished, study [49] has successfully implemented DMI in a comparable lattice spin model with an in-plane ground state. With an in-plane spin configuration, the out-of-plane DM-vector is invariant under the symmetry operation $[C_2||C_{4z}t]$, thus conserving the altermagnetic symmetry.

2.3 Spin currents

Here, the concept of a spin current is introduced, which describes a net flow of spin angular momentum [50]. Spin currents can be created by a number of phenomena, a direct approach being spin pumping, where magnons are induced via resonance effects [44]. In this work, magnonic spin currents caused by thermal effects are treated. There exists also a short range spin current stemming from conduction electrons, which will not be discussed [51]. The studied effects generating spin currents are the spin Seebeck effect (SSE) and the spin Nernst effect (SNE), which are explained in sections 2.4 and 2.5.

⁵currently at the HUN-REN Wigner Research Centre for Physics, orcid.org/0000-0001-9456-5755

An intuitive approach to define any kind of particle current, is to sum over all allowed wave vectors \vec{k} of the number of particles $n_{\vec{k}}$ multiplied by the group velocity $\vec{v}_{\vec{k}}$ and the unit $m_{\vec{k}}$ transported by a single particle. This can be expressed as

$$\vec{j} = \left\langle \sum_{\vec{k}} m_{\vec{k}} \cdot n_{\vec{k}} \vec{v}_{\vec{k}} \right\rangle \quad (2.44)$$

where we optionally average over time [29, 51].

In the case of ferromagnets this would already be the definition of a spin current with $m_{\vec{k}} = \pm \hbar = \text{const.}^6$ [29], as there is only one magnon-chirality in ferromagnets.

In magnetic systems with magnons carrying different angular momentum, one has to consider all eigenmodes. Therefore, after normalization of spins to unit length, the spin current is expressed as

$$\vec{j}(\vec{r}) = \sum_{\vec{k}} n_{\vec{k}}^{\alpha}(\vec{r}) \cdot \vec{v}_{\vec{k}}^{\alpha} - n_{\vec{k}}^{\beta}(\vec{r}) \cdot \vec{v}_{\vec{k}}^{\beta} \quad (2.45)$$

where α and β denote right- and left-handed magnon chirality and $n_{\vec{k}}^{\alpha/\beta}$ denotes the number of magnons with given chirality at position \vec{r} . The group velocity is defined as $\vec{v}_{\vec{k}}^{\alpha/\beta} = \partial \omega_{\vec{k}}^{\alpha/\beta} / \partial \vec{k}$ for each chirality [23, 51].

In the spin dynamics simulations performed here, the number of magnons or their group velocity is not explicitly computed. Therefore, we desire an expression dependent on the spins $S_x^A(\vec{r}_l)$ and $S_y^B(\vec{r}_l)$ with the different sublattices (SLs) A and B at the position \vec{r}_l of unit cell l . In appendix B.1, formulas which can be used to calculate the spin current in different crystallographic directions based on the specific spin configuration are derived. The derivation is analogous to that of [23] which was inspired by [29].

For the crystallographic directions $\theta = [100]$ and $\theta = [010]$,

$$\begin{aligned} j^{\theta}(\vec{r}) = & -\frac{\gamma_e}{\mu_B} a J_1 \left(\left\langle S_x^A(\vec{r}) \cdot S_y^B(\vec{r} + a \cdot \vec{e}_{\theta}) - S_y^A(\vec{r}) \cdot S_x^B(\vec{r} + a \cdot \vec{e}_{\theta}) \right\rangle \right. \\ & \left. + \left\langle S_x^B(\vec{r}) \cdot S_y^A(\vec{r} + a \cdot \vec{e}_{\theta}) - S_y^B(\vec{r}) \cdot S_x^A(\vec{r} + a \cdot \vec{e}_{\theta}) \right\rangle \right) \end{aligned} \quad (2.46)$$

can be used to determine the spin current. Here, a is the lattice constant, μ_B is the Bohr magneton, γ_e is the electron magnetic ratio, J_1 is the nearest neighbour interaction, and the subscripts and superscripts denote the components and SLs. The vector \vec{r} points to the respective spin. The unit vectors \vec{e}_{θ} are along the straight directions: $\vec{e}_{[100]} = \begin{pmatrix} 1 \\ 0 \\ 0 \end{pmatrix}$ and $\vec{e}_{[010]} = \begin{pmatrix} 0 \\ 1 \\ 0 \end{pmatrix}$.

For the diagonal directions we use unit vectors $\vec{e}_{[1\bar{1}0]} = \frac{1}{\sqrt{2}} \begin{pmatrix} 1 \\ -1 \\ 0 \end{pmatrix}$ and $\vec{e}_{[110]} = \frac{1}{\sqrt{2}} \begin{pmatrix} 1 \\ 1 \\ 0 \end{pmatrix}$. The equations are

$$\begin{aligned} j^{[1\bar{1}0]}(\vec{r}) = & -\frac{\gamma_e}{\mu_B} \tilde{a} \left(J'_2 \left\langle S_x^A(\vec{r}) \cdot S_y^A(\vec{r} + \tilde{a} \cdot \vec{e}_{[1\bar{1}0]}) - S_y^A(\vec{r}) \cdot S_x^A(\vec{r} + \tilde{a} \cdot \vec{e}_{[1\bar{1}0]}) \right\rangle \right. \\ & \left. + J_2 \left\langle S_x^B(\vec{r}) \cdot S_y^B(\vec{r} + \tilde{a} \cdot \vec{e}_{[1\bar{1}0]}) - S_y^B(\vec{r}) \cdot S_x^B(\vec{r} + \tilde{a} \cdot \vec{e}_{[1\bar{1}0]}) \right\rangle \right) \end{aligned} \quad (2.47)$$

⁶Sign dependent on ground state.

and

$$\begin{aligned} j^{[110]}(\vec{r}) = & -\frac{\gamma_e}{\mu_B} \tilde{a} \left(J_2 \left\langle S_x^A(\vec{r}) \cdot S_y^A(\vec{r} + \tilde{a} \cdot \vec{e}_{[110]}) - S_y^A(\vec{r}) \cdot S_x^A(\vec{r} + \tilde{a} \cdot \vec{e}_{[110]}) \right\rangle \right. \\ & \left. + J'_2 \left\langle S_x^B(\vec{r}) \cdot S_y^B(\vec{r} + \tilde{a} \cdot \vec{e}_{[110]}) - S_y^B(\vec{r}) \cdot S_x^B(\vec{r} + \tilde{a} \cdot \vec{e}_{[110]}) \right\rangle \right) \end{aligned} \quad (2.48)$$

where $\tilde{a} = \sqrt{2}a$ is the lattice constant in the diagonal direction, as discussed in Sec. 3.3. The exchange constants J_2 and J'_2 are introduced in Sec. 2.2.1.

The formulas all associate neighbouring spins along a specific direction with another. This interchange is identified as a spin current. The dimension of the spin current here is $L T^{-1}$ because the spins are normalized to unit length and dimensionless. This definition is valid for our use case. A more practical, measurable quantity is obtained by for example multiplying with the magnetic moment of a single spin. As explained in the following sections, spin currents are expected as part of the spin Seebeck effect (SSE) and the spin Nernst effect (SNE).

2.4 Spin Seebeck effect

The Seebeck effect, which has been known for well over 200 years [52], describes the generation of electric voltage due to a temperature gradient in a conductor.

An analogous effect was observed in a conductor by Uchida et al. [53] in 2008, where a spin voltage resulting in a spin current was measured as a result of a temperature gradient. This phenomenon has been coined spin Seebeck effect (SSE) and opened the field of ‘spin caloritronics’, which explores the interplay between spin and heat transport phenomena.

Notably, the SSE is able to generate spin currents even over macroscopic distances (several millimeters), far exceeding the typical spin-flip diffusion length of conduction electrons in metals [53], calling into question whether electrons are the primary mediators of this effect [51]. In addition, SSE has been universally observed in semiconductors [54], and, strikingly also in magnetic insulators [50]. The fact, that heat flow is converted into a spin voltage despite the absence of conduction electrons, proves spin waves as the primary force of spin current [51]. Additionally, there are phononic effects, which can play crucial roles at low temperatures [51]. As we are only looking at the purely magnonic contribution in this work, the role of phonons will not be discussed here.

When subjecting a material to a heat bath, spin waves are excited, and a higher temperature causes a higher magnon population. A temperature gradient in the material therefore leads to an imbalance which results in a net flux of magnons along the temperature gradient $-\nabla T$, which can be observed as a spin current [29, 51, 55]. Depending on the boundary conditions of the material, this propagation of magnons can cause an accumulation of spins in the cold region [29]. The magnon accumulation can be defined as the deviation of the local magnetization $\vec{S}(\vec{r})$ from its equilibrium value $\vec{S}_0(\vec{r})$ [29, 55], given by

$$\Delta \vec{S}(\vec{r}) = \vec{S}(\vec{r}) - \vec{S}_0(\vec{r}). \quad (2.49)$$

This definition can also be used sublattice-wise. Generally, the magnon accumulation is present in the region of the temperature gradient. An exponential decay can be used to give an estimate for the longest propagation length of the spin waves [29].

To discuss the connection between the SSE and different materials, we will shortly mention different peculiarities. As discussed before in Sec. 2.1.4, magnons in FMs have a well-defined chirality and carry spin currents. Therefore, a temperature gradient creates a magnon accumulation and reduces the local magnetization compared to the ground state [23, 29]. In AFMs, the net magnetization and excitation vanish, as both sublattices compensate each other. There is no net spin current [23, 51, 55]. Hence, magnon currents carrying a spin angular momentum require an externally applied field or higher-order exchange interactions like the Dzyaloshinskii-Moriya interaction.

Lastly, we look at the behaviour of AMs regarding the SSE. For this model, a net magnon accumulation has been confirmed along the diagonal directions of the model shown in Fig. 2.6 [21]. A spin current was also found by Weissenhofer and Marmodoro in spin dynamics simulations [23].

In previous investigations, the influence of specific quantities on the spin Seebeck effect have been inspected. It has been established, that a higher temperature gradient ∇T is proportional to a higher spin current [50, 53] and magnon accumulation [29, 55]. Additionally, the peak magnon accumulation increases with a lower damping coefficient for a temperature step [21, 29].

In this work, we will further investigate the relationship between the magnon dispersion relation and magnonic transport, specifically also for an external magnetic field.

2.5 Spin Nernst effect

In addition to the longitudinal spin Seebeck effect (SSE), we also study a transverse spintronic effect, which is called spin Nernst effect (SNE). The SNE refers to a transverse pure spin current as a result of longitudinal temperature gradient [56, 57]. It is schematically depicted in Fig. 2.7. The SNE is one of many transverse transport effects, which can occur in the solid state [57]. Its name is in reference to the Nernst effect, which describes the generation of a charge current perpendicular to a temperature gradient in longitudinal direction, when a transversal magnetic field is present [58].

The SNE has first been predicted in a series of theoretical publications since 2008 [56, 59–63]. Qualitatively, these articles predicted that electrons with different spins would be subject to different transverse forces under thermal drive, the ultimate origin of the electronic SNE being spin-orbit interaction [57, 61–63]. The electronic SNE can be divided into an intrinsic and extrinsic contribution. The extrinsic contribution can mainly be attributed to spin-dependent scattering of electrons, for example at impurities [56]. The intrinsic contribution can be connected to the so-called Berry curvature [63].

In 2016, two independent groups achieved experimental observation in platinum [57] and tungsten [64], proving the existence of the electronic SNE.

The remaining question is, whether there is a SNE in magnetic insulators. There have been a number of theoretical predictions of a magnon-mediated SNE in collinear AFMs with DMI [14, 65–67]. AFMs are obvious candidates to realize a magnon SNE, as there are two magnon modes with opposite angular momentum, in contrast to FMs. Because of that internal degree of freedom, magnons can be expected to fulfil similar roles as spin- $\frac{1}{2}$ electrons [14, 66]. It was found, that the magnon modes with

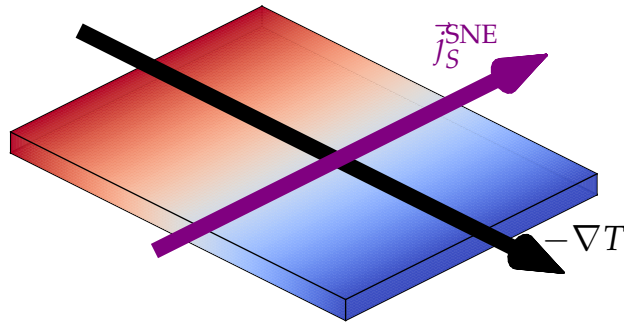


Figure 2.7: Schematic depiction of the SNE with a temperature gradient ∇T and a perpendicular pure spin current j_S^{SNE} .

opposite chirality are driven oppositely by a temperature gradient which yields a net transverse magnon spin current [65, 66]. The physical mechanism was identified to be the aforementioned Berry-curvature, here, of magnon bands [14, 65, 66]. For AFMs, the higher-order DMI also plays a vital role, as it causes a symmetry breaking and a population imbalance between magnons with opposite wave vector \vec{k} , which ultimately leads to a transverse current for each spin species [66].

There have been experimental results consistent with the predicted magnon SNE [13], but the results are still ambiguous because of challenges regarding the separation of the SNE from other effects [14].

Altermagnets are of special interest regarding the SNE, because of their unique band structure for magnons without any relativistic effects like DMI [23]. A recent analytical paper suggests the existence of magnon SNE without DMI [22]. Furthermore, a simulation work on an AM has found a transverse spin current as a result of a longitudinal temperature gradient [23].

In this work, the altermagnetic toy model will be used to further investigate the spin Nernst effect (SNE). For that, the transversal spin current and spin accumulation at the transverse edges are of interest, as these can occur as a result with the correct boundary conditions [14, 68].

Chapter 3

Methods of Simulation

After having established the theoretical basis for this work, we need to consider *how* to get simulation results of the phenomena we want to study. The foundation for this lies in the stochastic Landau-Lifshitz-Gilbert (LLG) equation (2.13), which has to be solved for a system of spins. After setting the basis on how differential equations can be solved numerically, we introduce the specific implementation of the spin system in this work.

3.1 Numerical solving of stochastic differential equations

As mentioned, the goal is to solve the LLG equation (2.13) with thermal noise (2.16) numerically. With the introduction of noise, this becomes a stochastic differential equation (SDE).

To begin, we first only consider an ordinary differential equation (ODE) and cite Refs. [69–72]. Specifically, we have an initial value problem (IVP)

$$\begin{cases} y'(t) = f(t, y(t)) \\ y(t_0) = y_0 \end{cases} \quad (3.1)$$

which we want to solve on an interval $[t_0, t_{\max}]$ to get to the solution $y(t)$. Here, f is a continuously differentiable function which depends on the model of the system and y_0 is the initial condition. In the case of the LLG, y corresponds to a vector containing the 3 components of all N spins of the system (i.e. $y \in \mathbb{R}^{3N}$) and $f : \Omega \rightarrow \mathbb{R}^{3N}$ ($\Omega \subset \mathbb{R}^{3N+1}$ open) is the right side of Eq. (2.13) for each component of each spin.

To solve numerically, we discretize t into equidistant steps

$$t_j := t_0 + j \cdot \Delta t \quad (3.2)$$

with $j = 1, 2, \dots, n$ and $t_n \geq t_{\max}$ with step size Δt . The idea is, to determine an approximation η_j for the solution $y(t_j)$ at position t_j .

The most intuitive approach to solving this IVP is to take the difference quotient $(y(t_j + \Delta t) - y(t_j)) / \Delta t$ and assume it to be equal to $y'(t_j) = f(t_j, y(t_j))$. We use this to get the approximation η_j for $y(t_j)$. Rearranging gives us

$$\eta_{j+1} = \eta_j + \Delta t \cdot f(t_j, \eta_j) . \quad (3.3)$$

This procedure is called explicit (forward) Euler method and allows us to determine η_1, η_2, \dots successively. The implicit (backward) Euler method uses $f(t_{j+1}, \eta_{j+1})$ instead of $f(t_j, \eta_j)$, which can yield more stable results but requires to solve the implicit equation numerically, as η_{j+1} is on both sides of the equation.

This procedure can be generalized to one-step methods. Here we calculate the approximate solution to an IVP with

$$\eta_{j+1} = \eta_j + \Delta t \cdot \Phi(t_j, \eta_j, \eta_{j+1}, \Delta t) \quad (3.4)$$

where Φ is an appropriate method function. The explicit Euler method is a one-step method with $\Phi = f(t_j, \eta_j)$. One can further define the local discretization error and the consistency of the procedure. For the explicit Euler method e.g., the error decreases linearly with decreasing step size and it is consistent as the error goes towards 0 for $\Delta t \rightarrow 0$.

We consider Heun's method with method function

$$\Phi(t_j, \eta_j, \Delta t) := \frac{1}{2} [f(t_j, \eta_j) + f(t_j + \Delta t, \eta_j + \Delta t \cdot f(t_j, \eta_j))] \quad (3.5)$$

which is an explicit one-step method. It can be interpreted as the average of the explicit and implicit Euler method. Instead of actually calculating η_{j+1} for the backward Euler method, we use the forward Euler method as a predictor formula

$$\tilde{\eta}_{j+1} = \eta_j + \Delta t \cdot f(t_j, \eta_j). \quad (3.6)$$

Because the value for η_{j+1} is first predicted via the forward Euler method, and then this information is used to refine ('correct') the numerical η_{j+1} , this method is a predictor-corrector method [12, 73].

All of the mentioned procedures are Runge-Kutta methods. These methods take multiple slope evaluations within a step and then compute a weighted average of those slopes to produce a more accurate update [69–72].

The choice of iteration scheme is dependent on the desired computational cost, the accuracy of the result, and therefore also on the preferred step size. There are methods with adaptive step size control, which estimate the current error and adjust the step size accordingly [73].

By incorporating thermal noise (2.14) into the LLG equation, it becomes a stochastic differential equation (SDE). The differential equation then looks like

$$y'(t) = f(t, y(t)) + g(t, y(t)) \xi(t) \quad (3.7)$$

where f and g are given functions depending on the specific problem and $\xi(t)$ is white noise [12, 74]. Because of the inherent randomness in the noise, trajectories with the same starting conditions differ. Hence, an average over these trajectories is taken for specific quantities of interest. The method is called Langevin dynamics simulation [12]. As the thermal average of the (quasi-) equilibrium result is the same for different paths, we do not need to average over the trajectories for this work.

In the case of the LLG equation with thermal multiplicative noise, a problem called Itô-Stratonovich dilemma arises. It is caused by mathematically consistent definitions of stochastic integrals which generally lead to different results for different time discretization schemes [12, 74, 75]. Equation (3.7) is not well defined [75]. The Itô interpretation of the stochastic integral includes noise at the beginning of each time step, making it 'non-anticipating': The trajectory $y(t)$ only depends on $\xi(t')$ for $t' < t$. In contrast, the Stratonovich interpretation evaluates it at the midpoint between the current step and the next one, anticipating the next step. This can make sense in continuous processes [76]. Hence, the use of the Stratonovich interpretation has been well established in many physics contexts, like the stochastic LLG [12, 75],

76].

The easiest implementation of the Stratonovich method uses the aforementioned Heun discretization scheme (3.5) [12]. The result is

$$\eta_{j+1} = \eta_j + \frac{1}{2} [f(t_j, \eta_j) + f(t_{j+1}, \tilde{\eta}_{j+1})] \Delta t + [g(t_j, \eta_j) + g(t_{j+1}, \tilde{\eta}_{j+1})] \tilde{\xi}_j \quad (3.8)$$

where the predictor $\tilde{\eta}_{j+1}$ is calculated via the Euler method

$$\tilde{\eta}_{j+1} = \eta_j + f(t_j, \eta_j) \Delta t + g(t_j, \eta_j) \tilde{\xi}_j. \quad (3.9)$$

Here, $\tilde{\xi}_j$ are random numbers from a Gaussian distribution with zero mean and a variance $\propto \Delta t$ [12].

The stochastic Heun method is used in the simulations performed for this work. Additionally, a projection method is used, as the Heun method does not conserve spin length [77, 78].

3.2 Implementation of the spin system

The preferred numerical method for solving SDEs must now be implemented on some kind of processing device. The simulations done for this thesis were performed on a program called cuLLG, which was initially developed by Andreas Donges as a part of his dissertation [77]. It was later expanded by other researchers [39].

The program leverages the NVIDIA CUDA application programming interface (API) to run highly parallelized software on graphics processing units (GPUs), simulating atomistic spin dynamics by implementing the LLG. For a full description of CUDA, we refer to the official documentation [79]. The software for this work is programmed in C++, although CUDA provides support for a number of languages, such as FORTRAN or even Python [80].

In contrast to central processing units (CPUs), which are able to perform more complex calculations sequentially, GPUs excel at performing thousands of calculations in parallel [80]. For the large number of spins, which are simulated, the utilization of GPUs therefore provide a substantial performance improvement [77].

In the program, each atom is given a position (see Sec. 3.3) and a normalized magnetic moment (spin). The spin \vec{S} has components S^x , S^y and S^z . By default, the initial spin configuration is paramagnetic, but it can also explicitly be set. An easy-axis checkerboard AFM for example, typically has a starting configuration of $S^x = S^y = 0$ and $S^z = \pm 1$ depending on the SL.

3.3 Structure definition

The first step of implementing the toy model, which was introduced in Sec. 2.2.1, is to define the basic structure in the cuLLG software. As the program returns data for each layer, as explained in Sec. 3.7.1, it is necessary to implement a structure with the conventional orientation and in a rotated orientation. These configurations can be seen in Figs. 3.1 and 3.2 respectively.

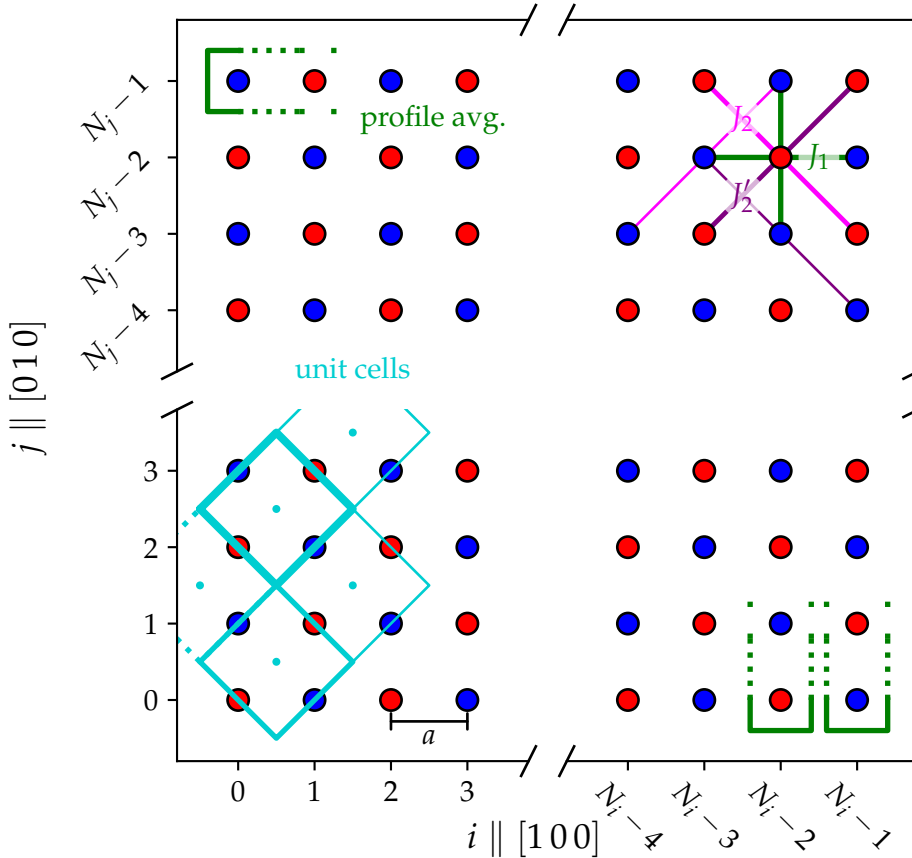


Figure 3.1: Schematic depiction of the implementation of the ‘nontilted’ configuration, which is a direct translation from the toy model in Fig. 2.6. The depicted lattice has grid dimensions of $N_i \times N_j \times N_k$. The green markings and the unit cell definition are discussed in Secs. 3.7.1 and 3.7.2 respectively.

Each particular structure is defined by implementing a C++ header file, which is imported by the project. This file is responsible for setting relevant parameters and most importantly, defines the rules that describe the structure itself [78].

The foundation of the structure is a grid, where each point corresponds to an atom of a specific SL or an empty lattice site. Moreover, the number of grid sites in each direction within a unit cell and the physical lattice constant are defined. As all considered energy contributions are independent of the distances between the magnetic moments, the lattice constant can be chosen arbitrarily for this work. It is set to be in the orders of angstrom.

Depending on the specific definitions, the lattice is filled with spins of corresponding SLs. Each lattice point is referenced by the coordinates i, j, k , which uniquely define its position. Here, i is the index in x -direction, j in y -direction and k in z -direction. This coordinate system can be seen in Figs. 3.1 and 3.2.

The nontilted configuration can be seen in Fig. 3.1 and is the intuitive implementation of the toy model structure. Here, N_η specifies the number of lattice points in η -direction. The markings and legends are discussed in the subsequent sections.

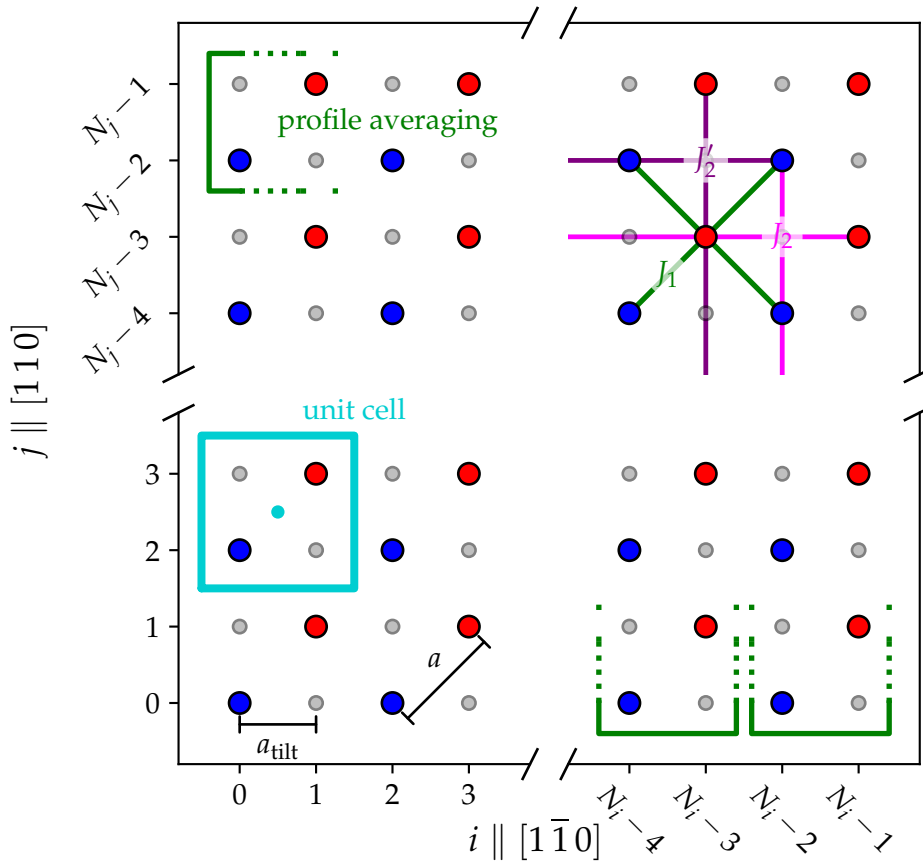


Figure 3.2: Schematic depiction of the implementation of a ‘tilted’ configuration, which can be understood as a counterclockwise rotation of 45° of the nontilted configuration. The depicted lattice has grid dimensions of $N_i \times N_j \times N_k$, with $N_{i/j}/2$ unit cells fitting next to each other in i/j -direction. The green markings and the unit cell definition are discussed in sections Secs. 3.7.1 and 3.7.2 respectively.

As mentioned, a system which is rotated by 45° , as shown in Fig. 3.2, must be implemented as well to obtain data along the diagonal crystallographic directions. In this implementation, a modified lattice constant

$$a_{\text{tilt}} := \frac{a}{\sqrt{2}} \quad (3.10)$$

is used, which is in accordance with the nomenclature of [21]. Furthermore,

$$\tilde{a} := 2 \cdot a_{\text{tilt}} = \frac{2}{\sqrt{2}} a \quad (3.11)$$

is defined as the width of a unit cell.

The intuitive approach would be to place the atoms at positions i and j which are multiples of $\frac{1}{2}$. In contrast, the implementation on grid structures on GPUs only allows integer grid points. Hence, the system is scaled by a factor of two and empty lattice points are introduced. They can be seen as smaller gray dots. It should be noted that this scaling factor causes the simulation to run with one half of the atoms in the tilted system compared to the conventional configuration with the same grid

dimensions.

Note, that the crystallographic directions in the tilted setup differ from the previous work [21] to fix a slight discrepancy in the model.

So far, we have ignored the layers in k -direction. In the discussed figures, this corresponds to the out of plane direction. In this work, we simulate a two-dimensional material, but it is still necessary to introduce at least two layers in direction of the third dimension because of boundary constraints. For that, we simply layer the discussed structure on top of another. The material is still two-dimensional because the exchange energy between spins with different k -index will be set to zero. The actual implementation of the altermagnetic structure is part of the following section, where the implementation of exchange energies is introduced.

3.4 Exchange files

After the realization of the checkerboard lattice, the exchange parameters for the Heisenberg model (see Sec. 2.1.2) are implemented. This is done by creating files which contain magnetic material parameters and an exchange list. These files are then imported at runtime.

The header of the file is used to define the values of the gyromagnetic ratio γ in units of the electron gyromagnetic ratio γ_e , the magnetic moment μ_s in units of the Bohr magneton μ_B and parameters for magnetic anisotropies. In our case, we only use and define the easy-axis anisotropy d_z . The specific values chosen for this work can be extracted from Table 3.1. The software allows to set a single scalar exchange constant J_{ij} or a 3×3 tensor \tilde{J}_{ij} [78]. As we also consider the second order DM interaction, we need to define the complete exchange matrix instead of only setting a scalar interaction constant between neighbors.

Due to the use of two sublattices (SLs), two exchange files are defined. The first nearest neighbour interaction with differences in i or j values of ± 1 are the same for both SLs. Because of the nature of this toy model, the directional dependence of the second nearest neighbour interaction is opposite for the different SLs.

Specifically, the nearest neighbour interaction matrix can be defined as

$$\tilde{J}_1 := \begin{pmatrix} \tilde{J}^{xx} & \tilde{J}^{xy} & \tilde{J}^{xz} \\ \tilde{J}^{yx} & \tilde{J}^{yy} & \tilde{J}^{yz} \\ \tilde{J}^{zx} & \tilde{J}^{zy} & \tilde{J}^{zz} \end{pmatrix} = \begin{pmatrix} J_1 & 0 & 0 \\ 0 & J_1 & \pm D \\ 0 & \mp D & J_1 \end{pmatrix}. \quad (3.12)$$

Here, D is the length of the DM-vector (2.43). For simulations without the DMI, D is zero. The sign before D in the matrix is dependent on whether the exchange interaction is implemented in the exchange list for SL A (upper sign) or SL B (lower sign). This is also explained in Sec. 2.1.2 and becomes clear, as the cross product is

Table 3.1: Material and exchange parameters used in this work.

Parameter	Value	Parameter	Value
gyromagnetic ratio γ	$1.0 \gamma_e$	exchange constant J_1	-20 meV
Gilbert damping α	0.02	exchange constant J_2	15 meV
magnetic moment μ_s	$1.0 \mu_B$	exchange constant J'_2	5 meV
anisotropy d_z	2 meV	DM exchange constant D	0, 2, 5 meV

anti-commutative. In the Appendix B.2 it is shown, that this interaction matrix is equal to a nearest neighbour exchange energy and a nearest neighbour DMI term by explicit calculation.

The second nearest neighbour interaction has a direction dependency which is opposite for the different SLs. The interaction matrices can be defined as

$$\mathfrak{J}_2 := \text{diag}(J_2, J_2, J_2) \quad \text{and} \quad \mathfrak{J}'_2 := \text{diag}(J'_2, J'_2, J'_2) \quad (3.13)$$

with only nonzero entries on the diagonals. The values of the exchange constants used in simulations for this thesis are listed in Table 3.1.

There are no exchange constants defined for neighbors with different k value, even though a minimum of two layers are simulated. This results in each layer to be completely independent of another.

It is necessary to create separate files for the tilted and nontilted system. This is because the nearest neighbors have different relative i and j coordinates in the tilted system, as described in the previous section.

It must be mentioned that when studying real materials, exchange constants which stem from experimental sources or a priori calculations are used. In this case however, a toy model is used which does not directly come from an actual material. Therefore, the interaction values are kept such to keep a finite Néel temperature and the qualitative properties of the simulated material are mainly of interest.

3.5 Boundary conditions

Since a finite number of spins are simulated, the question arises as to how edges are handled. One possibility is to use periodic boundary conditions, which were introduced in Sec. 2.1.4 about magnons. We can for example set periodic boundary conditions in $x \parallel i$ direction. As a result, there is a nearest neighbour interaction of a spin with index $i = N_i$ and $i = 1$ for example. Spin $(N_i + 1)$ corresponds to spin 1. In the program this is achieved by extending the grid by a halo in each direction. This halo contains virtual neighbouring cells, with which the spins at the edges can interact. Its size is dependent on the maximum interaction distance of the Heisenberg exchange interactions and determined at runtime [77].

The other option is to use open boundary conditions. In this case spins at the edges have fewer spin with which they interact. This abrupt cut can cause spin waves to reflect at the boundaries, travelling back in opposite direction. Hence, interference of reflected spin waves can occur [39]. The extent of this is governed by the propagation length of the spin wave, which is smaller for larger Gilbert damping parameters [21]. It can therefore be sensible to set the system size large in comparison to the spin propagation length or have a comparable damping to limit the propagation length.

If periodic boundary conditions are unwanted, absorbing boundary conditions (ABCs) can be applied to reduce the amount of spin wave reflection. These conditions create a buffer region, where the Gilbert damping parameter α is modified with the goal of absorbing spin waves in this area [39]. There are a number of models available, such as constant damping offset, a linear increase or an exponential increase of α .

Because the aim is to decrease reflections at the boundaries, a steady increase in contrast to an abrupt change is advantageous. Here, we choose a tangens hyperbolic

function to reduce unwanted reflections, which has been shown to be effective [81]. Specifically, the function is of form

$$\alpha(r) = \alpha_0 + \alpha_{\max} \cdot \frac{1}{2} (1 - \alpha_0) \left[\tanh \left(\frac{\frac{1}{2}d - r}{\Delta} \right) + 1 \right] \quad (3.14)$$

where r is the distance of the spin to the boundary. With the size of the boundary region d , this ABC is then applied for $r \leq d$ for the specified directions. Here, Δ is the width of the function and describes how abruptly the Gilbert damping parameter α increases. The parameter α_0 should be set to the damping value of the system, ensuring a smooth increase to the maximum value of α_{\max} . The region d and the width Δ should be large enough to guarantee a slow increase with $\Delta \ll d$ to make sure the maximum damping value α_{\max} is (nearly) reached at the boundary $r = 0$. At $r = d/2$, the Gilbert damping parameter is halfway up to α_{\max} with $\alpha(d/2) = \alpha_0 + \frac{1}{2} \alpha_{\max}$ and at $r = d$ the function is close to the offset α_0 .

For most simulations the following values were used, when applying ABCs: $\alpha_0 = 0.02$, $\alpha_{\max} = 1.0$, $d = 100$ or 50 lattice points and $\Delta = 10$ or 5 lattice points. These values ensure a steady increase from the damping base value α_0 , minimizing spin wave reflections at the boundaries while requiring only a small number of lattice points.

With appropriate parameters, this ABC causes a high damping near the edge which leads to enhanced dissipation [39]: Because of the slow change of α , this hyperbolic ABC effectively minimizes reflections [81].

3.6 Thermal models

Thermal excitation has been discussed in Sec. 2.1.3 about the stochastic LLG. A more complete discussion of the used temperature model can be found in the work of Ritzmann [29].

In this work, the model is kept deliberately simple: electron and phonon temperatures are not distinguished, and energy dissipation between the subsystems is neglected.

We consider two simple models. The first sets a constant equilibrium temperature for the whole lattice. It is used to determine properties of ground states with different parameters. Results can for example be found in Sec. 4.1.

On the other hand, a temperature model, which sets the temperature dependent on the lattice position is used. The temperature is specifically set according to a step function. One side of the crystal then is in a temperature bath with temperature T_1 , while the other side is at a lower temperature T_0 . This model is used, to consider transport phenomena, specifically the SNE and SSE. The program allows us to set the temperature step along a desired axis (x , y or z).

3.7 Simulation output

Lastly, a few different types of output files of the cuLLG program are mentioned and discussed. The simplest type of file storing spin orientation data is a bulk file, which contains various parameters averaged over the entire lattice at certain time steps in a

whitespace-delimited file. Most importantly, it contains the average spin orientation for each SL at certain time steps.

The duration of a time step is set when the simulation is started. Furthermore, the number of time steps between saving the average configuration is defined. This is helpful to ensure a high accuracy of the simulation while minimizing the time spent writing data to the hard drive. If necessary, the number of time steps between each iteration of saving data can be lowered to increase the time resolution of the resulting available data.

A more detailed file containing data for the described time steps are files containing a magnetic profile, which is explained in the following.

3.7.1 Layer-wise magnetisation output

The magnetic profile files contain layer-wise output. The structure is separated into layers along a certain direction. If the profile direction x is chosen, the layers in the y - z -plane are averaged, yielding the average spin configuration along the x -axis.

To be more precise, the simulation creates one profile file per SL, in this case for SL A and SL B. Each file then contains the averaged spin components $\langle S^x \rangle_l$, $\langle S^y \rangle_l$ and $\langle S^z \rangle_l$ every few time steps as explained above. Here, l specifies the index of the layer, which was used to compute the average.

It has to be noted, that not every layer is created equally. For that we take a look at Figs. 3.1 and 3.2 which show the nontilted and tilted spin configuration. The green markings indicate what constitutes a layer. In the nontilted case, a layer has the width of one spin, i.e. one lattice constant a . For the tilted system, the width of one layer is two spins which corresponds to \tilde{a} with the modified lattice constant $\tilde{a} = \sqrt{2} \cdot a$ as defined in Eq. (3.11).

The different widths of the layers when averaging require double the number of points in the profile direction to have the same number of layers compared to the nontilted configuration. This setup makes sense, as only half the grid points actually correspond to magnetic moments in the tilted setup.

3.7.2 Spin configuration output

When starting the simulation, it is moreover possible to define the number of time steps, after which spin configuration files are written. A configuration file contains the spin orientation of every single spin, which is why it is unfeasible to create one as frequently as magnetic profiles are saved.

The file is structured as a whitespace separated table with seven columns. The first three columns specify the index coordinates i, j, k , which were also used in Figs. 3.1 and 3.2 to describe the configuration. The fourth column specifies the SL of each magnetic atom and the last three columns contain the three spin components S^x , S^y and S^z .

For analysis, this data is read via Python and saved in a five-dimensional NumPy [82] array for further processing. The tools which were used for analysis can be found in the [Tools Used](#) section after the [References](#) and will not be discussed further here.

The usage and presentation of this data is far from trivial. One possibility would be to simply plot the magnetization S^z along the easy axis of every single spin as a

two-dimensional color plot. Most of the time however, this approach does not yield very helpful results and the amount of detail hinders understanding. The solution is local averaging.

As an example, consider the tilted configuration in Fig. 3.2. Here, it is intuitive to define the unit cell as shown, as the whole grid can be covered with unit cells without issue as the primitive lattice vectors are parallel to $[1\bar{1}0]$ and $[110]$. For representing the spin configuration, each unit cell can be used to average the information within. It has to be noted that the unit cell has a width and height of two grid points, which is why only $N_{i,j}/2$ can be placed next to another in i/j -direction.

The situation is more complex for the conventional orientation in Fig. 3.1. Here, it is not as trivial to choose a sensible unit cell which can be used for averaging. For most use cases, the cells marked in cyan will be used. They are to be interpreted as containing half of different grid points. This definition has the advantage of making the cells isotropic in contrast to for example placing the unit cells a little bit to the left to contain exactly two spins. The natural problem for the nontilted configuration is the handling of boundaries, as it is impossible (for any valid unit cell) to properly cover all spins at all edges. Depending on the physical problem, the cell which is marked with dotted lines can also be considered. In this case, the most outmost spins make up the average of the whole cell and therefore have more ‘weight’. Neglecting the dotted cell causes the outmost spins to be only counted half. It has to be evaluated, which case is more favourable dependent on the situation.

This dilemma can be solved for one axis/direction but not both axes at the same time. By taking the mean similarly to the profile averaging, it is possible to fix the problem for a chosen direction.

Apart from presenting the complete configuration data, the data is also very useful to do manual averaging in a specific region. When using the magnetic profile file as explained in Sec. 3.7.1, averaging over whole crystal layers takes place. Using a spin configuration file, one can for example only consider spins in the cold region and take appropriate averages there. This can be very useful but has the disadvantage, that only a single time step can be considered, as configuration files cannot feasibly be created en masse, in contrast to using profile files where different time steps can be used for averaging. Therefore, one may end up with more noise. An attempt of resolving this issue, is to increase the number of layers in z -direction, as they are independent of each other anyway. This can help to have more data for averaging and to reduce noise.

Chapter 4

Results

In this chapter, we present the results stemming from simulations of the altermagnetic toy model introduced in Sec. 2.2.1. The validity of this model has been shown in the previous work by Schmidhuber [21], where the equilibrium state and the spin Seebeck effect (SSE) has been studied without an external magnetic field.

In this work, the equilibrium and SSE results with a Zeeman term are discussed. Subsequently, the spin Nernst effect (SNE) investigated, and lastly, the effect of the Dzyaloshinskii-Moriya interaction (DMI) on the equilibrium state and the SSE is examined.

4.1 Equilibrium properties

Equilibrium results like the Néel temperature and dispersion relation of the altermagnetic toy model without an external field can be found in Ref. [21]. The validity of this toy model has been established and the dispersion relation retrieved from the spin simulations are in agreement with the analytical results.

4.1.1 Introduction of a static magnetic field

To further study the equilibrium properties of AMs, we introduce an external magnetic field

$$\vec{B} = B \cdot \vec{e}_z \quad (4.1)$$

along the easy axis.

To start, the change in magnetization with different magnetic field strengths B is considered. For that, simulations at a set temperature $k_B T = 2 \text{ meV}$ with periodic boundary conditions are performed. The simulation parameters can be found in Table 3.1. In the following, this temperature was always used unless specified otherwise.

The resulting macroscopic magnetization averages for each sublattice and the normalized net magnetization are depicted in Fig. 4.1 for different field strengths B .

It is visible that the absolute value of the normalized magnetization S_B^z for SL B decreases while S_A^z increases with higher magnetic fields. Meanwhile, the average of the normalized net magnetization

$$S_{\text{net}}^z = \frac{S_A^z + S_B^z}{2} \quad (4.2)$$

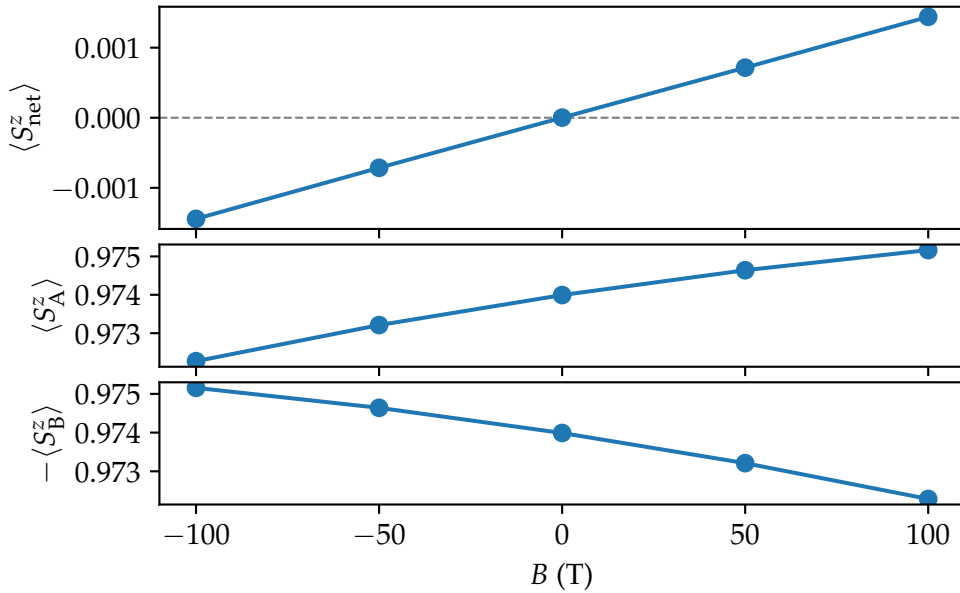


Figure 4.1: Field dependence of the average SL and net ground state magnetization along the easy axis for $k_B T = 2$ meV.

is linearly proportional to B . Often, we will just write S^z instead of S^z_{net} .

This behaviour can be explained by considering the Hamiltonian for the extended Heisenberg model Eq. (2.9). The system tries to minimize the total energy. Therefore, the system decreases the magnetic moments S^z_B along the $-z$ -direction and increases S^z_A along the $+z$ -direction for $B > 0$, in order to minimize the contribution from the Zeeman term Eq. (2.5). The antiferromagnetic exchange interactions and the easy axis anisotropy term on the other hand, are minimized by having the magnetic moments of both SLs antiparallel. This prevents the magnetic moments from pointing along \vec{B} like in the paramagnetic case.

Note, that Fig. 4.1 is the behaviour at a finite temperature below the Néel temperature. The thermal perturbation is necessary for this behaviour, as spin waves are excited and the spins have in-plane components. Because of the positive magnetic field, the in-plane amplitude at a given time decreases for SL A and increases for SL B, respectively.

The linear behaviour of the magnetization far below the spin-flop transition is supported by experimental results on an AFM [83].

Note, that the magnetic field strengths which were used here appear to be very large. Nonetheless, a spin-flop transition is not observed, i.e. the antiparallel ordering stays persistent as seen in Fig. 4.1. The high absolute values of B will not be further addressed and are attributed to the use of a toy model, which has, for example, a very high anisotropy of 2 meV. Additionally, AFMs tend to show a small dependence on external fields before the spin-flop transition, as experimental data suggests [83].

To further investigate the ground state, the dispersion relation is determined along the crystallographic directions $[1\ 0\ 0]$, $[0\ 1\ 0]$, $[1\ \bar{1}\ 0]$, and $[1\ 1\ 0]$ for the case with and without an external magnetic field. The resulting magnonic dispersion relations can be found in Fig. 4.2.

The basis for the shown dispersion relations are simulations with dimensions of

$1024 \times 1024 \times 16$ for the nontilted directions and $2048 \times 2048 \times 4$ for the tilted directions. The high number of $N_x = 1024$ unit cells along x and y ensures a high resolution for the k -vector and periodic boundary conditions prevent boundary effects. The simulations were set to save the magnetic profile every 50 simulation steps, which corresponds to a time resolution of $\Delta t = 5\text{ fs}$, enabling the detection of high frequencies. To also ensure a high frequency resolution, $N_t = 300\,000$ time steps are considered.

Basis for the dispersion relations from simulation data is to find a term for the magnon density $n(\omega, k)$ based on simulation quantities. For that, the variables

$$S^\pm(t, x) = S^x(t, x) \pm iS^y(t, x) \quad (4.3)$$

are considered. Ritzmann [29] shows that the absolute square of the Fourier transform of S^\pm corresponds to the magnon density.

Therefore, we utilize the two-dimensional Fourier transform

$$\tilde{S}^+(\omega, k) = \int \int S^+(t, x) \cdot e^{-i(\omega t + kx)} dt dx. \quad (4.4)$$

Considering we only know the sample points $t = n_t \Delta t$ and $x = n_x \Delta x$ (for $n_t = 0, 1, \dots, N_t - 1$ and $n_x = 0, 1, \dots, N_x - 1$), we set

$$\omega_{m_t} = \frac{2\pi}{N_t \Delta t} m_t, \quad m_t = 0, 1, \dots, N_t - 1 \quad (4.5)$$

and

$$k_{m_x} = \frac{2\pi}{N_x \Delta x} m_x, \quad m_x = 0, 1, \dots, N_x - 1 \quad (4.6)$$

to accompany the discrete nature of the lattice and the time steps. Here, Δx is the respective lattice constant a or \tilde{a} for the nontilted or tilted system. Inserting this into the integral results in

$$\tilde{S}^+(\omega_{m_t}, k_{m_x}) \propto \sum_{n_x=0}^{N_x-1} \sum_{n_t=0}^{N_t-1} S^+(n_t \Delta t, n_x \Delta x) \cdot \exp \left[-i 2\pi \left(\frac{n_t m_t}{N_t} + \frac{n_x m_x}{N_x} \right) \right], \quad (4.7)$$

ignoring the constant factor $\Delta x \Delta t$. This definition exactly corresponds to the discrete Fourier transform, implemented by the Python package NumPy [82, 84–86]. This double sum is referred to by $n(\omega, k)$ and plotted as a function of ω and k in the colourplots in Fig. 4.2. Note that the colourbar is capped at 10^{-2} and 4×10^5 , respectively, to ensure that finer details remain discernible. The triangular markers at the ends of the colourbar indicate this capping.

Figure 4.2 consists of eight dispersion relations which were created as described. Each row corresponds to a different crystallographic direction, as denoted on the left. For a temperature of $k_B T = 2\text{ meV}$, the left column contains the dispersion relations in equilibrium without an external magnetic field, while the right depicts dispersion relations for a system with a magnetic field of $B = 100\text{ T}$ along the easy axis as in Eq. (4.1).

First of all, we focus on the dispersion relations which have been observed before [21]. As already discussed in Sec. 2.1.4 about AFMs, magnon modes with left- and right-handed precession can be observed. Here, the positive and negative frequencies correspond to the RHM and LHM respectively.

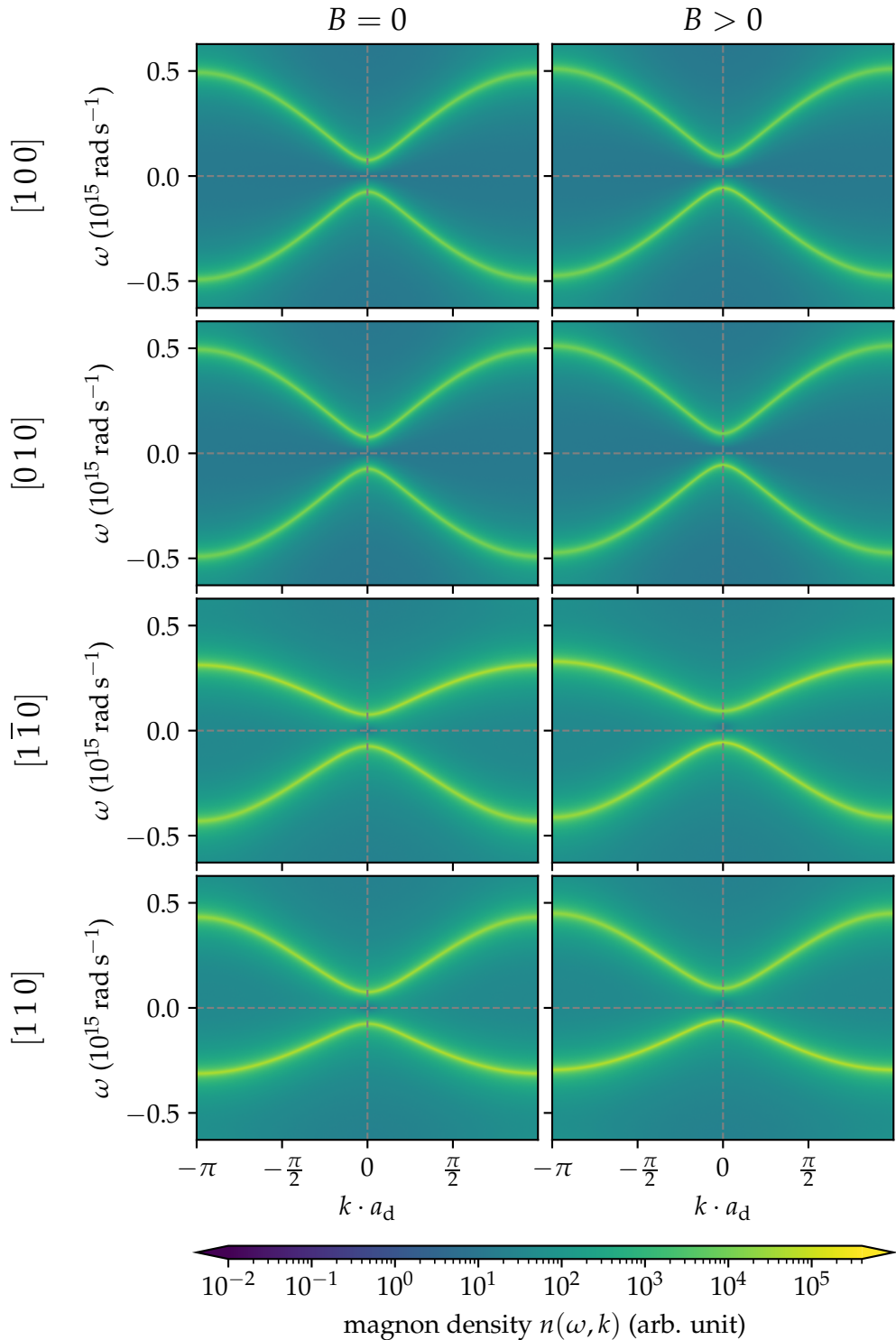


Figure 4.2: Magnonic dispersion in equilibrium for different crystallographic directions with and without an external magnetic field B . Here, $a_d = a$ for $[100]$ and $[010]$, and $a_d = \tilde{a}$ for $[1\bar{1}0]$ and $[1\bar{1}\bar{0}]$.

All magnon dispersion relations show symmetry regarding the Γ -point ($k = 0$), where the modes are degenerate. Both branches also contain magnons with both propagation directions, which can be verified by considering the group velocity $\frac{\partial\omega}{\partial k}$.

The dispersion relations for the directions [1 0 0] and [0 1 0] are in line with those of AFMs as described in Sec. 2.1.4. This is expected, as these directions contain uniform exchange energies for both SLs.

Conversely, for the directions [1 $\bar{1}$ 0] and [1 1 0], the degeneracy is lifted for $|k| > 0$. Two distinct magnon bands are visible, which both occupy lower energies compared to the directions [1 0 0] and [0 1 0]. This is explained by the smaller absolute values of J_2 and J'_2 compared to J_1 . Moreover, the mirroring of the magnon bands for directions [1 $\bar{1}$ 0] and [1 1 0] can be attributed to the opposite roles of J_2 and J'_2 in the different directions.

As an example, let us further consider direction [1 $\bar{1}$ 0] in detail. In this case, J'_2 describes the interaction between spins of SL A, while J_2 connects spins of SL B with $J'_2 < J_2$. Using the convention in Fig. 2.4, the LHM ($\omega < 0$) is the mode in which the down-spin sublattice carries the larger oscillation amplitude. For [1 $\bar{1}$ 0] this leads to a larger mode energy $\hbar|\omega|$ for the LHM. This finding is consistent with the larger exchange on SL B: because oscillations primarily involve B spins (which have the stronger coupling J_2), those oscillations cost more energy and therefore appear at higher precession frequencies. In other words, the mode dominated by the SL with the larger exchange constant reaches higher frequencies $|\omega|$.

This argument is plausible, as spin waves which are mainly carried in one of the SLs can be expected to behave similar to ferromagnetic spin waves. Their dispersion relation is also directly proportional to the exchange energy [34].

Since the different modes correspond to precession dominated by one of the SLs, we also refer to the right-handed (RH) magnons as SL A magnons, and to the left-handed (LH) magnons as SL B magnons. Analogously, we also call the frequency of the RHM $\omega_A > 0$ and the frequency of the LHM $\omega_B < 0$.

The SL A magnons carry negative angular momentum, as the up spins have a higher precession amplitude. Conversely, the SL B magnons carry positive angular momentum.

As already outlined in Sec. 2.1.4, the easy-axis anisotropy causes a band gap in the magnon bands, which can also be observed here. This means, a finite energy is required to excite spin waves.

Note, that in Ref. [21] the dispersion relations are vertically flipped. Even though the opposite is stated in their methodology (Eq. (6.1.3)), this might for example be attributed to a flipped sign in the Fourier transform.

In this classical simulation, incoherent spin waves are excited according to a Rayleigh-Jeans distribution as explained in Sec. 2.1.4. This explains, why a broad range of frequencies is excited. Along [1 $\bar{1}$ 0] the occupation of SL A magnon modes is higher than that of SL B. In the perpendicular direction [1 1 0] the effect is reversed, and the two contributions cancel, so no net magnetization appears in the equilibrium state.

Now, we consider the introduction of the external magnetic field, as seen on the right side in Fig. 4.2. Qualitatively, the dispersion relations look similar, but they show a small shift upwards, i.e. the energy of the LHM branch decreases and of the RHM increases. The degeneracy is therefore also lifted for the [1 0 0] and [0 1 0] directions, especially at the Γ -point. There, it can also be observed that the gap between the signed frequencies stays essentially constant. This is difficult to discern but has been confirmed by further numerical analysis.

Note that a positive (negative) magnetic field shifts the ('signed') magnon bands uniformly up (down) in frequency. As a result, two dispersion branches can intersect at a finite wavevector k (a band crossing), producing degeneracy at $\pm k$ away from the Γ -point. Because the Zeeman shift is k -independent, the dispersions remain symmetric in k .

The observed shift can be explained in the classical picture in a similar way as the general structure was above. The introduction of the positive magnetic field keeps the SL A up spins even closer aligned with the easy axis. At the same time, a greater deviation from the antiparallel configuration is energetically beneficial for the SL B down spins. This interpretation makes it plausible that it is easier to excite magnon modes where spins of SL B have a larger oscillation amplitude. This is exactly what is visible in the dispersion relations: The LHM requires less energy to be excited in contrast to the RHM, where the magnon energy increases.

From this explanation, a magnetic field in the opposite, $-z$ -direction, is expected to cause a shift in the dispersion relation downwards. This is exactly what can be observed in Fig. 4.3.

Here, the dispersion relation is plotted for the magnetic field strengths $B = -100$ T, $B = 0$ T and $B = +100$ T exemplary for direction $[1\bar{1}0]$. It was generated in the same way as the other plots.

The shift downwards for $B < 0$ is consistent with the explanation provided above: In this case, a deviation from the antiparallel ground state requires less energy for spins of SL A, while more energy is needed for SL B. Therefore, the RHM, in which the up spins carry a larger oscillation amplitude, is easier to excite.

The results presented here are consistent with the experimental and numerical findings reported in Ref. [46], which show changes in the resonance frequencies of the two magnon modes with the same signs as observed here. In particular, they report a linear dependence of the resonance frequency on the applied magnetic field.

4.1.2 Surface effects

We will shortly consider surface effects in the equilibrium. Boundary effects are mainly of interest for us to compare with the magnon accumulation stemming from the SNE, as discussed in Sec. 4.3.1.

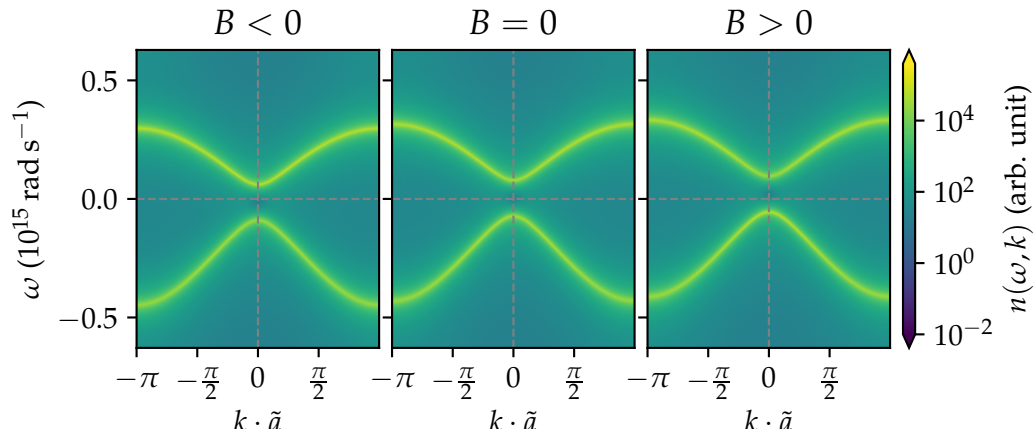


Figure 4.3: Magnonic dispersion in equilibrium along direction $[1\bar{1}0]$ for an external magnetic field along $-z$, no external field, and a field along $+z$.

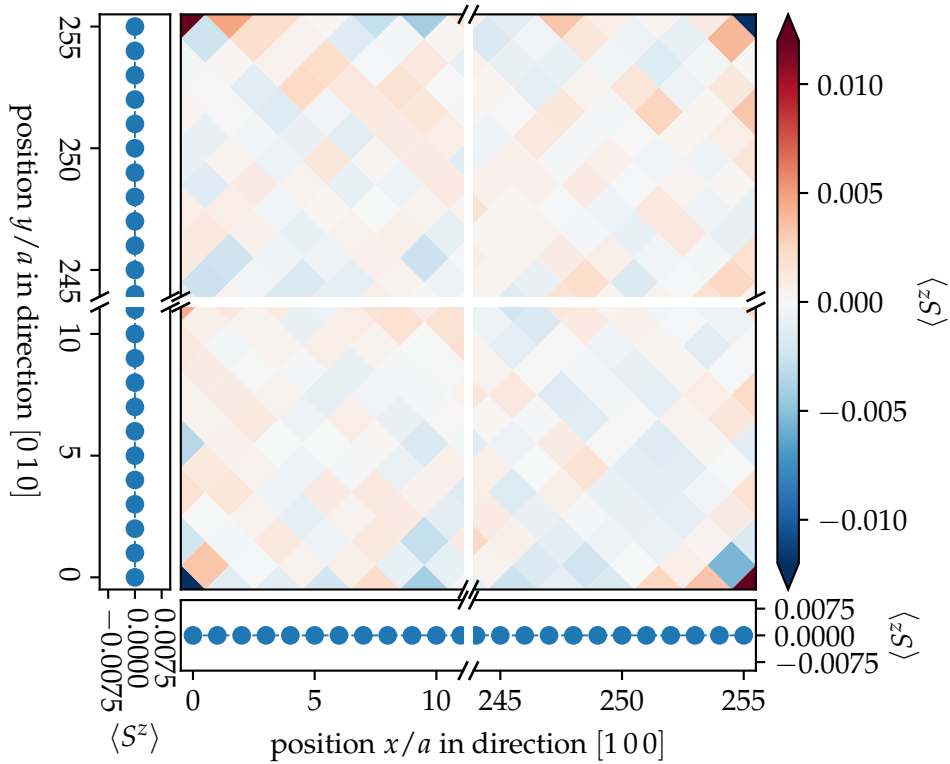


Figure 4.4: Spin configuration of the nontilted setup as presented in Fig. 3.1 near the open edges. Note, that unit cells at the edges contain fewer atoms, as indicated with a dotted line in Fig. 3.1. The left and lower plot show magnetic profile averages.

For that, we consider Figs. 4.4 and 4.5. The colourplots with broken axes in the center show the spin configuration near the edges at a set time step. The squares are placed according to the unit cell definitions in Figs. 3.1 and 3.2. Each cell contains the average normalized magnetization $\langle S^z \rangle$. Here, an average over two simulations and the 256 z-layers is performed to reduce noise.

Note, that for the nontilted configuration in Fig. 4.4, the unit cells at the edges contain fewer atoms than the cells in the center. Especially the unit cells in the corners each only contain a single atom. To prevent skewing of the colourmap, only these four cells have higher absolute magnetization than visible on the colourbar.

Additionally, Figs. 4.4 and 4.5 show the magnetic profiles on the left and bottom according to their definitions shown in Figs. 3.1 and 3.2. A time average over approximately 10 000 time steps is performed.

Both configurations show statistical noise away from the edges. In the time average or space average, the magnetization in these regions is zero however. More interesting are the boundaries. For the nontilted ('aligned') layout, no boundary effects are visible. The magnetization $\langle S^z \rangle$ is zero on average, even on the outmost layers.

For the tilted configuration shown in Fig. 4.5 conversely, boundary effects are visible. One denotes positive magnetizations at the edges in directions $[1 1 0]$ and $[\bar{1} 1 0]$. At the opposite edges, the magnetization is negative.

This can be explained by considering the tilted setup shown in Fig. 3.2. Consider the left edge, i.e. surface $(\bar{1} 1 0)$. Because of the specific geometry, the layer directly

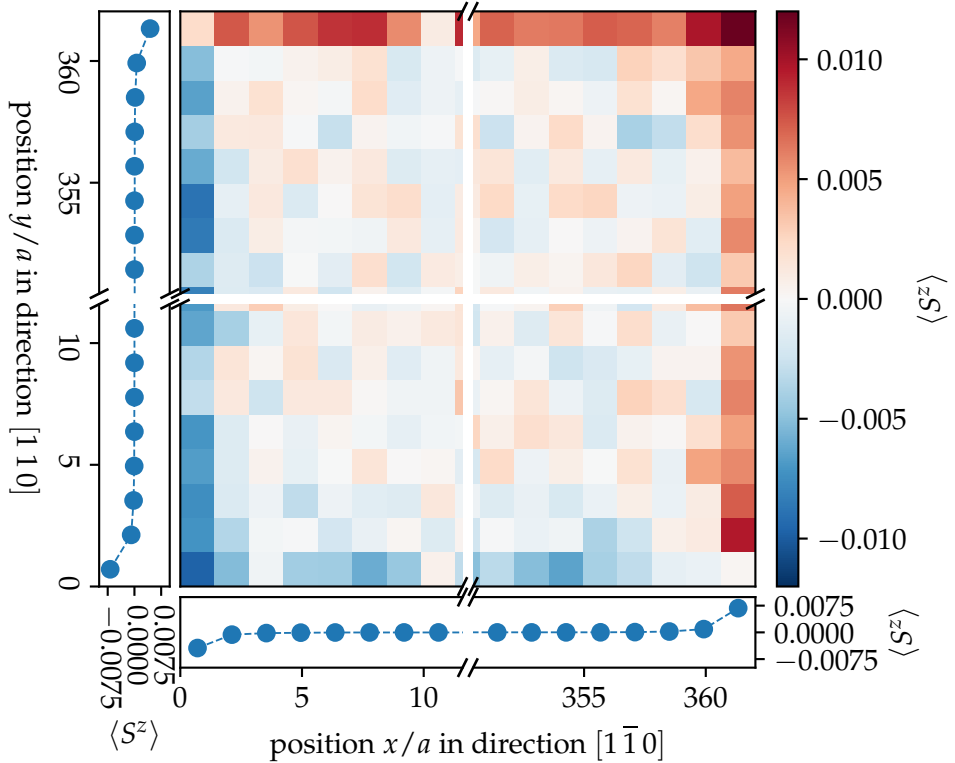


Figure 4.5: Spin configuration of the tilted setup as presented in Fig. 3.2 near the open edges. The left and lower plot show magnetic profile averages of the net magnetization.

at this edge consists only of up (SL A) spins. These spins are therefore missing the nearest neighbour interaction J_1 to the left. The next layer, however, only consists of SL B spins. They are not missing this interaction. Therefore, compared to the spins at the utmost edge, they are more closely aligned with the easy axis and have a smaller deviation from it. As a result, the absolute magnetization of the SL A spins is smaller as they can precess more freely. Thus, the average magnetization in the unit cells at this edge is negative.

This argument can be performed for every boundary. In the nontilted case in Fig. 4.4, the boundary layers consist of both up and down spins, which is why both SLs are affected by this geometry in the same way. The result is zero net magnetization.

Taking a closer look at Fig. 4.5 for the tilted setup, it is visible that the absolute magnetization $|\langle S^z \rangle|$ is greater for the boundaries in directions $[1\bar{1}0]$ and $[\bar{1}\bar{1}0]$. To explain this, the second nearest neighbour interactions have to be considered. In these cases, the spins at the utmost edge experience a weaker (J'_2) interaction along the boundary and a stronger interaction (J_2) perpendicular to it. The weaker interaction results in a higher number of spin waves due to lower dispersion bands, which causes a higher deviation and finally a higher absolute magnetization $|\langle S^z \rangle|$.

Lastly, we emphasize that the boundary effects are very much temperature dependent, as the deviations and precession of the spins increase with greater temperature. At the other extreme of $T = 0$ K, no boundary effects for any region can be observed, as the spins are never excited out of their antiparallel ground state. This has also been observed as a simulation result but is not specifically shown here.

Surface effects will be discussed further in regard to the SNE, specifically magnon spectra at the surfaces are shown in Fig. 4.15.

4.2 Spin Seebeck effect

In this section, the spin Seebeck effect (SSE) will be studied by applying a temperature step approximately in the center of the sample. This has already been examined for different parameters by Schmidhuber [21]. This work provides a more comprehensive explanation of the SSE in this material, focussing on the transport of magnons. Additionally, the SSE is further studied under the influence of an external magnetic field.

4.2.1 Introduction of a static magnetic field

To study the influence of a static external magnetic field along the z -axis according to definition (4.1), simulations are performed for different magnetic field strengths B .

Initially, the focus is on the SSE along the crystallographic directions $[1\bar{1}0]$ and $[110]$, as it has been found that these directions exhibit the SSE without an external field [21].

For that, a number of simulations on the tilted configuration in Fig. 3.2 are performed. The simulations use a sample with 256 unit cells along the direction of the temperature step (' x'). The temperature step is placed between the layer with index 125 and 126. Profile layers with index $i \leq 125$ are in a temperature bath with $k_B T_1 = 2$ meV while the cold region for $i \geq 126$ is set to be at absolute zero $k_B T_0 = 0$ meV. ABCs are enforced at the upper boundary in direction $-\nabla T$ to ensure no backflow of spin waves, although it has been established that the Gilbert damping is high enough to prevent this by itself.

The perpendicular direction (' y ') consists of 128 profile layers with periodic boundary conditions to prevent surface effects. Additionally, 128 layers are stacked in z -direction to decrease the amount of noise after averaging.

In Fig. 4.6, these time averaged spatial profiles have been plotted for a number of different magnetic field strengths and the directions $[1\bar{1}0]$ (solid lines) and $[110]$ (dashed lines). The position of the temperature step has been marked by a vertical grey, dashed line. We only show these directions, as they are the ones exhibiting the SSE without an external field.

For a better geometric understanding, we also refer to Fig. 4.12, where instead of the profiles, the complete configuration is shown. This figure is discussed in Sec. 4.3.1.

Additionally, the magnon accumulation $\langle \Delta S^z \rangle$ according to Eq. (2.49) is depicted in Fig. 4.7. To calculate the accumulation, the area left of the temperature step was subtracted by the average equilibrium value with the same parameters and a temperature of $k_B T_1 = 2$ meV, the area on the right conversely by the equilibrium value for $T_0 = 0$ K.

To explain the dominating phenomena, firstly the SSE without an external magnetic field ($B = 0$), i.e. the orange lines, will be discussed. The effect can be seen here as a finite magnon accumulation around the temperature step. Exemplary, we consider direction $[1\bar{1}0]$.

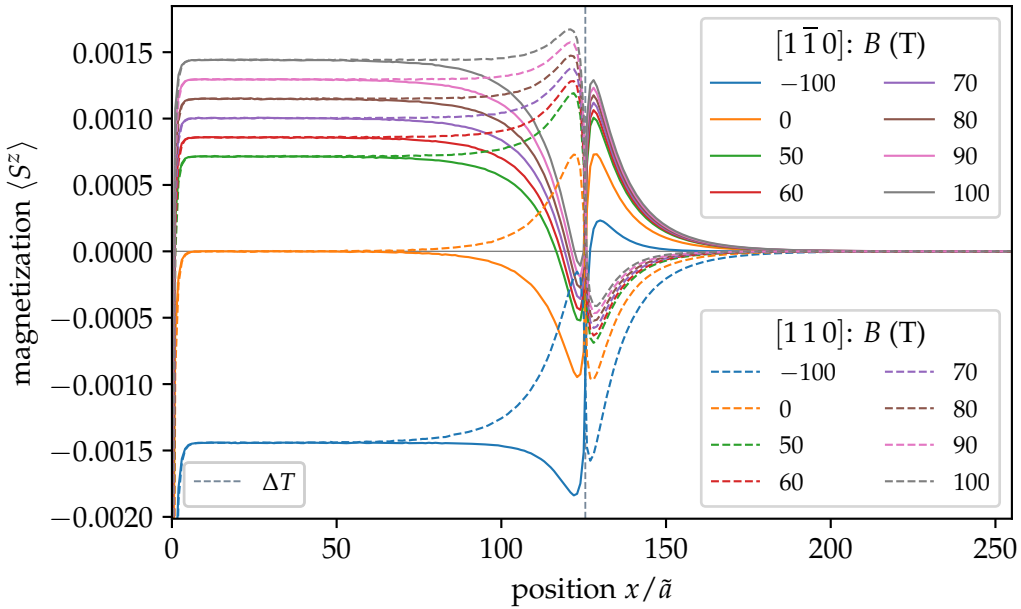


Figure 4.6: Magnetization profile in quasi-equilibrium for different magnetic field strengths. The temperature step of $k_B\Delta T = 2$ meV is marked by the grey, dashed line, with the higher temperature on the left.

Recall that here, right-handed (RH) magnons with $\omega_A > 0$ exhibit a higher amplitude in the precession of the SL A spins than of the SL B spins. Conversely, left-handed (LH) magnons ($\omega_B < 0$) show a larger precession amplitude in SL B. Therefore, we also describe RH magnons as SL A magnons and LH magnons as SL B magnons.

The RHM carries negative, while the LHM carries positive angular momentum.

Previously [21], the SSE has been explained by an imbalance in magnon populations along $[1\bar{1}0]$ ¹. Specifically, it has been explained by a higher population of SL B magnons in the warm region, which then results in more positive angular momentum carrying magnons travelling over the temperature step.

Conversely, our findings oppose this explanation, as SL B magnons occupy a higher energy band, as visible in Fig. 4.2, i.e. $|\omega_B(k)| > \omega_A(k)$ for $k \neq 0$ along $[1\bar{1}0]$, and are therefore more difficult to excite according to the Rayleigh-Jeans distribution Eq. (2.38).

This observation is supported by the findings of Weißenhofer and Marmadoro [23] on the altermagnetic rutile phase of RuO₂, also based on spin dynamics simulations. Their dispersion relation along $[110]$ ($\Gamma \rightarrow S$) shows that the mode carrying positive spin has higher energy. In this direction, they then observe the SSE, with a negative net magnetization before ($T > 0$) the temperature step, and a positive magnetization after ($T = 0$) it.

This aligns with our findings: The mode carrying positive spin is the SL B mode, which has higher energy in the direction $[1\bar{1}0]$. In this direction, we also see negative magnetization before the temperature drop and positive magnetization behind it. The signs of S^z due to the SSE is the same as for Weißenhofer [23] with a similar

¹As mentioned in Secs. 2.2.1 and 3.3, the crystallographic direction $[1\bar{1}0]$ ($[110]$) here is equivalent to the direction $[110]$ ($[\bar{1}10]$) in their work [21] to correct for inconsistencies.

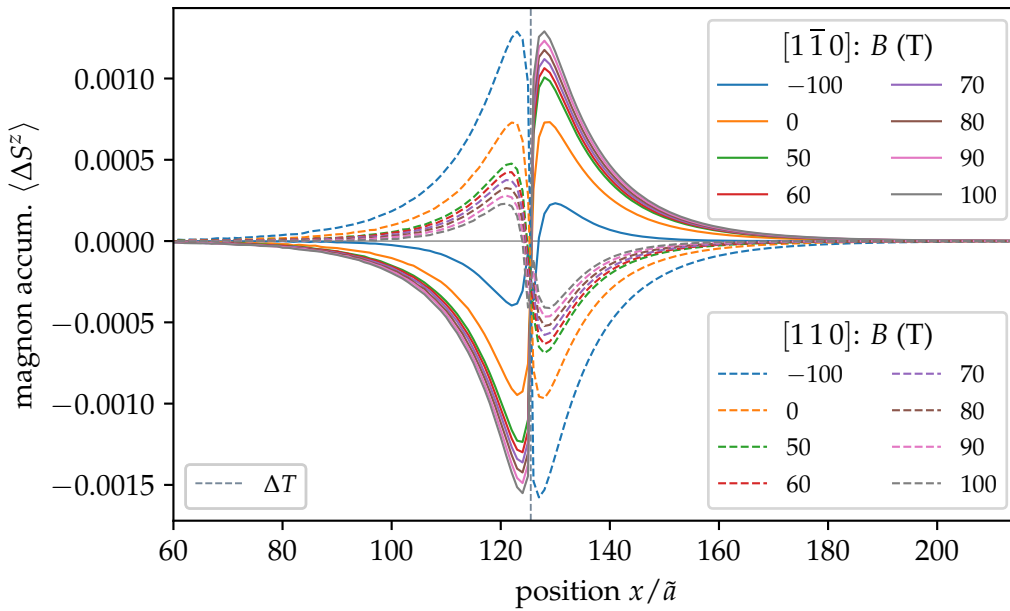


Figure 4.7: Magnon accumulation profile in quasi-equilibrium for different magnetic field strengths.

dispersion relation.

We therefore attribute this effect to a stronger transport of one mode compared to the other. In the specific case of $[1\bar{1}0]$, the stronger exchange interaction J_2 in SL B contributes to a greater transport of these spin waves along the temperature step, resulting in the observed magnetization profile. Notably, we know that the population of SL A magnons is higher in the warm region (for $[1\bar{1}0]$), but the increased transport still empowers the SL B magnons to dominate.

We now turn the focus on the field dependency of the SSE, as seen for exemplary field strengths in Figs. 4.6 and 4.7.

In the magnetization profiles in Fig. 4.6, a finite magnetization $\langle S^z \rangle$ is visible in the hot region. Comparing these values with Fig. 4.1 reveals, that these are exactly the equilibrium values. The values in the cold region all go towards zero magnetization, their ground state. This shows that the modes have a finite propagation length and the temperature gradient does not affect these regions any more.

Furthermore, a surface effect is visible in the hot region for $x \rightarrow 0$. In the cold region at absolute zero, the spins are in ground state, and no thermal perturbation takes place, thus there are no boundary effects. Additionally, ABCs would prevent an accumulation of spin waves.

Looking at the magnon accumulation $\langle \Delta S^z \rangle$ in Fig. 4.7, the profiles vary for different magnetic fields. It becomes clear that the absolute magnon accumulation is increased for direction $[1\bar{1}0]$ for positive fields. This behaviour is reversed for direction $[110]$ or negative fields due to the specific anisotropy of this model.

The magnetic field causes a shift in the bands, a positive field resulting in higher energy RH magnons on SL A. Conversely, the LHM is lowered. Considering the Rayleigh-Jeans distribution Eq. (2.38) of this classic simulation, we therefore expect a lifted number of SL B magnons, while the number of SL A magnons is lowered. Thus, more spin waves of SL B and fewer of SL A compared to the case without

magnetic field propagate along the temperature gradient. The result is a higher (or lower) magnon accumulation.

Additionally, LH (RH) magnons might carry a larger (smaller) angular momentum, as a greater deviation from the ground state is energetically less (more) costly than in the absence of a positive magnetic field.

With a negative field, the same arguments can be applied, yielding the higher magnon accumulation for the SSE along [110].

Contrary to the SSE without external field [21, 23], with $B \neq 0$, we also observe the effect in the [100] (and [010]) direction. This can be seen in Fig. 4.8, where the magnetization and magnon accumulation is plotted at a fixed magnetic field $B = 100$ T for different directions.

The argumentation to why the [100] now shows a SSE is similar to the change in magnon accumulation with the introduction of a magnetic field for the diagonal directions. Without external field, [100] shows behaviour expected from an AFM, as this direction contains uniform exchange energies for both SLs. The magnon bands are degenerate and the incoherently excited magnon modes are expected to have equal occupation. This degeneracy is lifted however, when a finite Zeeman term is introduced. In this case, one mode is easier to excite and more populated, hence resulting in a net transport along a temperature gradient. To be specific, in the case of $B > 0$, the LHM has lower energy and is more easily excited. Therefore, a positive angular momentum is transported along the temperature step.

We note that the magnon accumulation along [100] exhibits fundamentally different properties than the accumulation along the diagonal directions. For [100], both magnon modes of the AFM direction have nearly the same propagation length, even with a static magnetic field. Thus, we just see an exponential decay. For the diagonal AM directions however, the absolute magnon accumulation grows for a few lattice

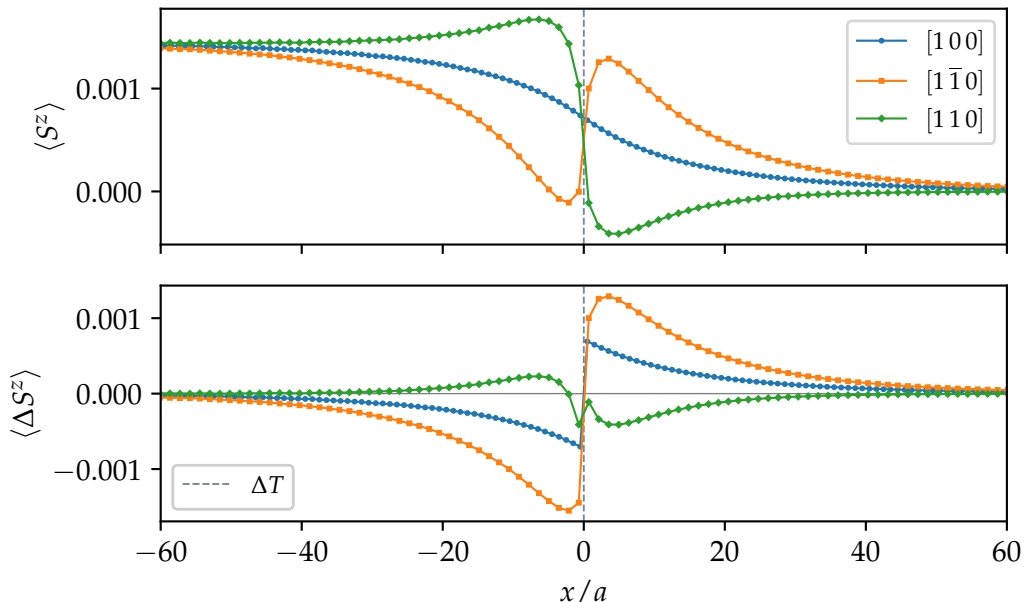


Figure 4.8: Magnetic profiles for directions [100], [110] and [110] with an external magnetic field $B = 100$ T and a temperature step marked by a vertical dashed, grey line.

points, only showing an exponential decrease further away. This hints towards two magnon modes with different propagation lengths competing.

Magnon propagation length

The propagation lengths of the different magnon modes is determined for directions $[1\bar{1}0]$ and $[110]$ for different fields.

In order to obtain the propagation lengths, the function

$$\Delta S^z(x > x_0) = A_\beta \exp\left(-\frac{x - x_0}{\xi_\beta}\right) - A_\alpha \exp\left(-\frac{x - x_0}{\xi_\alpha}\right) \quad (4.8)$$

was fitted to the magnon accumulation $\langle \Delta S^z \rangle$ behind the temperature step at x_0 . The expression is inspired by Boltzmann transport theory [23]. Here, $A_{\alpha/\beta}$ can be interpreted as the absolute magnon accumulation of a specific mode right behind the temperature step. The propagation length $\xi_{\alpha/\beta}$ is expected to differ for the different chirality magnons. All fit parameters are plotted in Fig. 4.9 for the directions $[1\bar{1}0]$ and $[110]$. The respective errors of the parameters are not shown, as they are very minute relative to the values.

We first turn our attention to the propagation lengths. At $B = 0$, we see that for direction $[1\bar{1}0]$, the SL B (β) mode has a propagation length about ten times as large as the one of the RHM. This is consistent with the magnon accumulation peaks being a few lattice points behind the temperature step, as both modes compete near the temperature drop. Further in the cold region, the RHM is practically not existent. The higher propagation length may be explained by the substantially larger exchange interaction in SL B compared to SL A.

Comparing the dispersion relations of both bands in Fig. 4.2, we additionally notice different slopes for the different bands. The slope corresponds to the group velocity

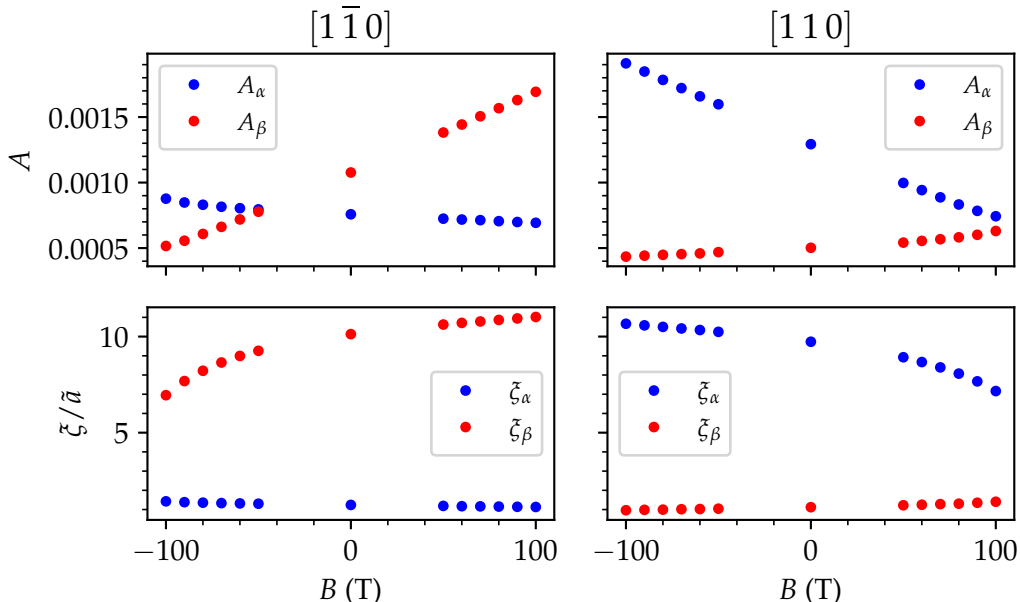


Figure 4.9: Mode specific magnon accumulation and propagation length for different field strengths along directions $[1\bar{1}0]$ and $[110]$.

$v_g = \frac{\partial\omega}{\partial k}$ and is proportional to the propagation length [87]. In $[1\bar{1}0]$ e.g., the β -mode exhibits higher group velocities for $k \cdot \tilde{a} \approx \pm \frac{\pi}{2}$, which is consistent with higher propagation lengths, as seen in Fig. 4.9.

Moreover, the propagation length of the β -mode (LHM) increases with larger magnetic field, while it decreases for the α -mode (RHM). This is plausible, as a positive magnetic field reduces the energy cost to excite the LHM. In particular, the magnetic field counteracts the effect of the Gilbert damping in the LLG for SL B spins, slowing the return to the ground state in the cold region, and thereby increasing its lifetime τ . Thus, the SL B spin waves can propagate over a larger distance, as $\xi \propto \tau$ [87]. For the α -mode, this behaviour is exactly reversed.

Note, that the rate of change of the respective modes differ significantly for the different crystallographic directions and also for different field ranges.

It is also visible that the absolute value of the propagation length is slightly higher for $[1\bar{1}0]$ compared to $[110]$. This is explained by the geometry of the lattice, specifically the placement of the temperature step. In the tilted configuration Fig. 3.2, the temperature step is always placed in a way, that the last warm layer consists only of SL B spins, while the first cold layer only consists of SL A. This can result in surface effects, especially since these layers directly interact via antiferromagnetic exchange interaction J_1 . This is supported by the fact, that the difference approximately is $\tilde{a}/2$, i.e. a single lattice point.

Now, the upper two plots in Fig. 4.9 regarding A_α and A_β are discussed. These quantities can be interpreted as the mode specific absolute magnon accumulation directly behind the temperature step.

We see here, what has previously been discussed: a magnetic field increases the magnon accumulation for the LHM. This is due to the shift in the band gap and a lower energy cost to excite these SL B spin waves. Conversely, the band of the RHM has been shifted up for $B > 0$, therefore the magnon population is smaller.

For a magnetic field strength of $B = 0$, more β -mode magnons travel over the temperature step than α -magnons for $[1\bar{1}0]$. For $[110]$, this behaviour is reversed. Reason for the stronger transport over the step can be found in a higher intrasublattice exchange in the respective SLs along the respective directions in addition to the greater propagation length. Both directions $[1\bar{1}0]$ and $[110]$ qualitatively show analogous progression of the respective field dependent mode-specific magnon accumulations A , i.e. A_α shows the same behaviour as A_β in the other direction, just flipped horizontally.

However, there is a notable shift of the absolute values of A between the different directions. This becomes even more notable, when considering the peak magnon accumulation in Fig. 4.10. The peaks were determined by taking the minimum and maximum values of the magnon accumulation, respectively, in the cold region. The peak values show a linear relation, undermined by linear fits (black), in regard to B , which is explained in the previous paragraphs.

These peaks reveal a higher absolute peak value for direction $[1\bar{1}0]$ compared to $[110]$. When comparing to Fig. 4.9, this becomes clear: the peak values are just the maxima and minima of Eq. (4.8). As the A_α (A_β) has higher (lower) absolute values for $[110]$ compared to A_β (A_α) for $[1\bar{1}0]$ but the propagation lengths do not show a large difference, the peak values are larger for $[110]$.

We believe that just like the small shift of the propagation lengths between $[1\bar{1}0]$ and $[110]$, the shift in A can be explained by the boundary at the temperature step.

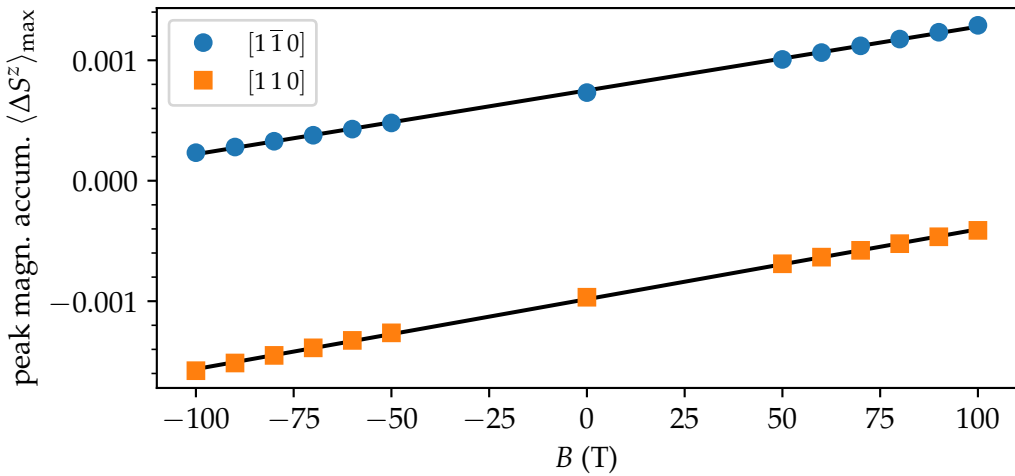


Figure 4.10: Peak magnon accumulation in the cold region for different fields and directions.

The SL A spins additionally directly interact with SL B spins in the warm region via J_1 . Because the intrasublattice interactions and dispersion relations are direction dependent however, this causes different amounts of excitation.

To paint a complete picture regarding the magnon accumulations in Fig. 4.7, we summarize the examined properties and behaviour.

In the hot region, thermal perturbation excites spin waves of different modes. At the temperature step, spin waves travel into the cold region due to an imbalance of magnon populations. We observe that the stronger exchange interaction in one SL is linked to a stronger transport of the magnon mode, which predominantly shows precession in said SL. This is quantified by the mode of stronger transport having a significantly longer propagation length. The result is a net magnetization transported into the cold region with a magnetization peak a few lattice points away from the temperature step. The magnitude of the SSE is further influenced by an external field, which causes a change in the magnon populations due to a band shift. It incites an additional change in the propagation lengths due to a change in magnon life times.

4.2.2 Spin currents

One substantial property of the SSE is the generation of spin currents along the temperature gradient. The measured spin current is shown in Fig. 4.11.

We use simulations with ABCs along the direction of the temperature step to prevent reflection of waves. The perpendicular has periodic boundary conditions to prevent surface effects. To ensure a result with low noise, the number of layers in z-direction has been set to 128.

The spin currents were determined by applying Eqs. (2.46) to (2.48) respectively. The expressions correlate neighbours along a specific direction with another. It is essential to correctly apply the average after calculating the cross product, as it is no linear operation. Thus, the configuration file was used to manually determine the current between individual neighbouring spins instead of relying on profiles.

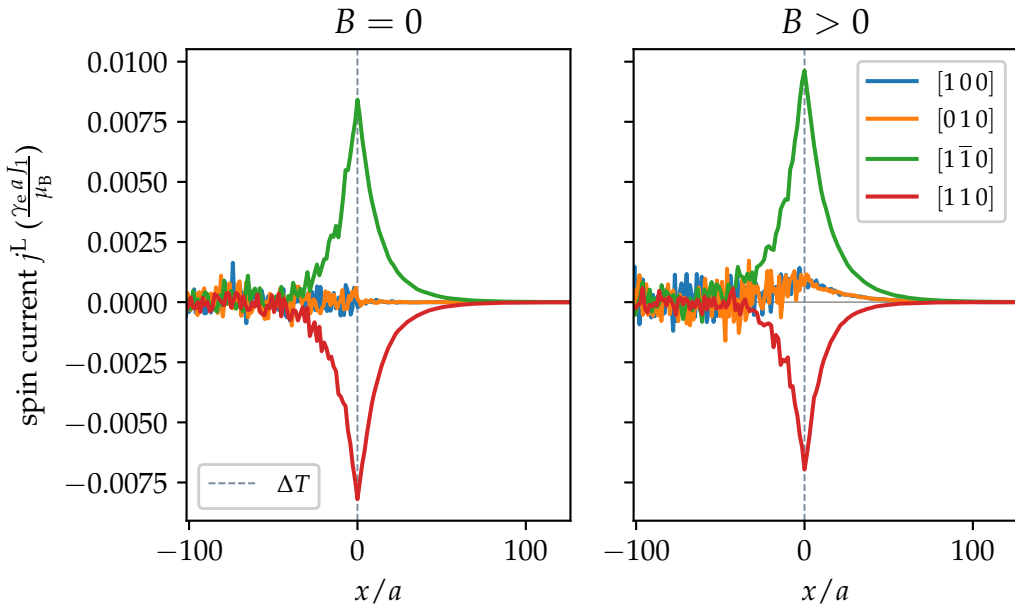


Figure 4.11: Generated spin currents due to the SSE around the temperature step with and without an external magnetic field.

Values were averaged over planar layers perpendicular to $-\nabla T$, yielding a one-dimensional profile of the longitudinal spin current along the temperature gradient at a specific time step.

The fluctuations in the warm region are attributed to thermal noise.

Without an external magnetic field, Fig. 4.11 shows spin currents for directions $[1\bar{1}0]$ and $[110]$ near the temperature step, while $[100]$ and $[010]$ show zero current. This concurs with the magnon accumulation in Fig. 4.7. Specifically, we see a positive longitudinal spin current in the case of a positive accumulation in the cold region ($[1\bar{1}0]$).

As discussed regarding Fig. 4.8, introduction of a magnetic field $B = 100$ T also enables a spin accumulation for the directions $[100]$ and $[010]$. This is visible here as the generation of a small current near the temperature step. Additionally, the magnitudes of the spin currents for the orthogonal directions change. Due to the higher magnon population in the LHM because of the band shift, a greater transport of angular momentum takes place. Conversely, the effect is reduced for $[110]$. It can be predicted that with $B < 0$ along $[110]$, one can see a similar impact as $[1\bar{1}0]$ for $B > 0$.

To summarize, we successfully observe the generation of spin currents in the presence of a temperature gradient. This provides further evidence of the SSE in the diagonal directions without external fields and in all crystallographic directions with an external field.

4.3 Spin Nernst effect

As a novel effect, the magnonic spin Nernst effect (SNE) was studied in the context of an altermagnet (AM). For that, we attempt to find a spin accumulation in forms of a net magnetization at the borders and a spin current in transversal direction.

4.3.1 Spin accumulation

To first get a better understanding of the underlying geometry of the SNE, we consider Fig. 4.12. Similar to the boundary plots in Sec. 4.1.2, we see an excerpt of the configuration in the center and appropriate magnetic profiles below and on the left. The excerpt focuses on the area around a temperature step $\Delta T = 2 \text{ meV}$ (dashed, green) in direction $-\nabla T \parallel [1\bar{1}0]$.

In the longitudinal x -direction, the graph of the magnetization is governed by the SSE, as discussed in Sec. 4.2.

The SNE now takes place in the perpendicular transversal y -direction. Considering the theoretical findings covered in Sec. 2.5, we are either in search of spin currents in this transversal direction, when we have periodic boundaries, or are looking for a net magnetization at the transversal edges due to an accumulation of magnons. We will first discuss the accumulation, which has been plotted for different directions in Fig. 4.13.

The plots are each characterized by a temperature gradient in the directions which have been examined for the SSE. They then show the average magnetization $\langle S^z \rangle$ along the transversal direction. A broken axis plot is used, as the boundaries are of interest: the transversal SNE current is expected to drive a spin accumulation at the surfaces in quasi-equilibrium [68].

We observe a SNE for temperature gradients along $[100]$ and $[010]$. For a temperature step along $[100]$, the plane (010) at a surface shows a negative magnetization in the order of 10^{-4} and $(0\bar{1}0)$ a positive magnetization conversely. For a temperature step along $[010]$, the signs of the surface magnetizations in transversal direction

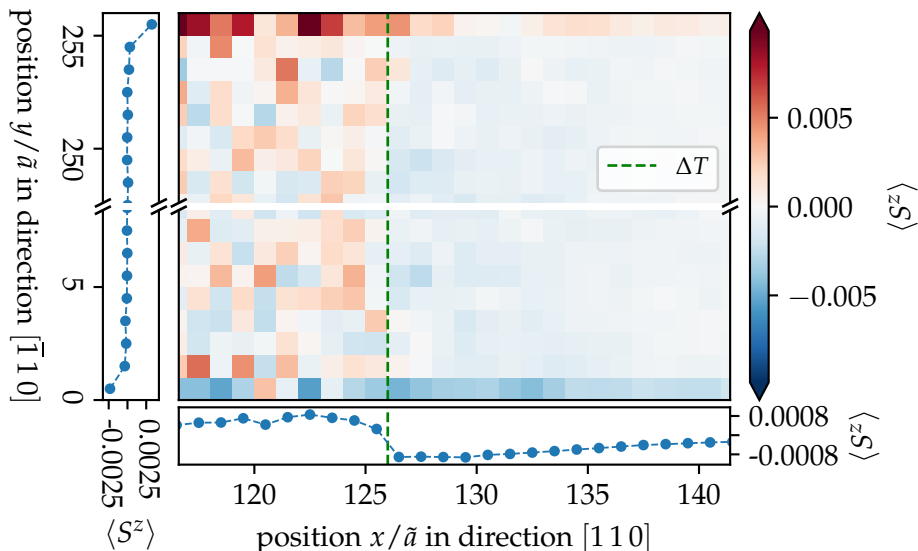


Figure 4.12: Spin configuration (of the tilted setup) with a temperature step. The left region is at $k_B T = 2 \text{ meV}$, the right region at $T = 0$.

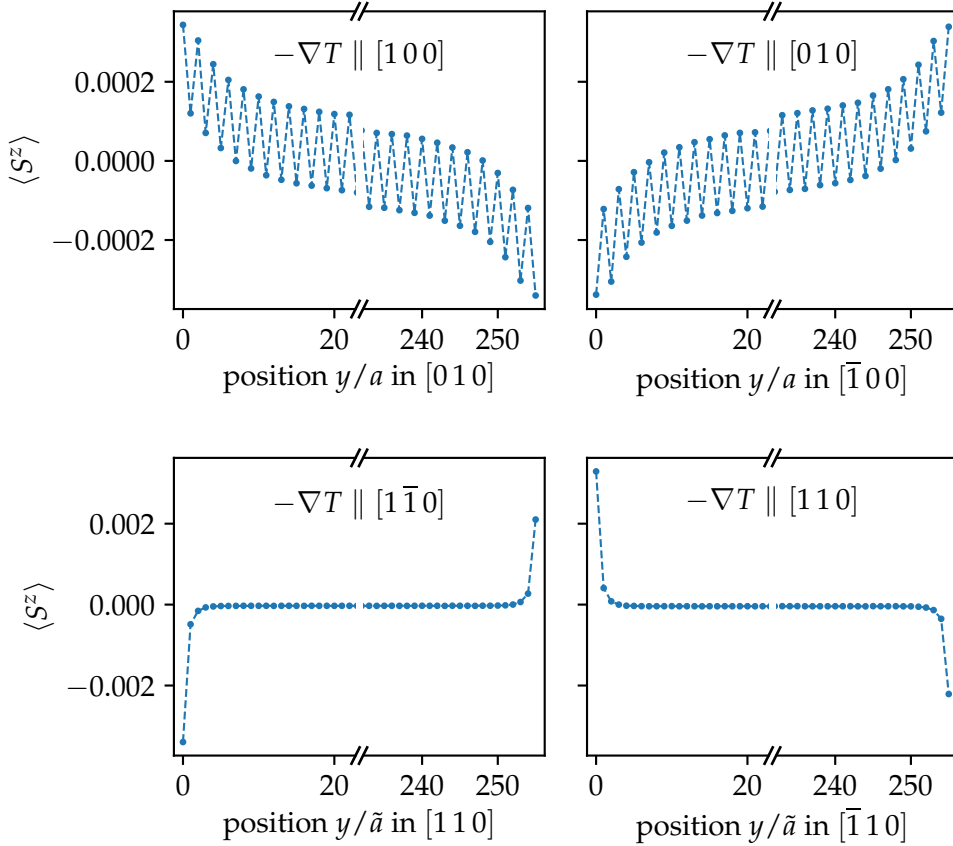


Figure 4.13: Magnetization profiles in transversal directions for temperature steps in $[100]$, $[010]$, $[1\bar{1}0]$, and $[110]$.

are reversed. This strongly indicates that the anisotropic intrasublattice exchange interactions are responsible for this effect.

If we consider our toy model in Fig. 2.6 and the information, we have gained from the study of the SSE (in Sec. 4.2), this can be explained by considering the diagonal directions. A temperature step along $[100]$ also causes spin wave propagation along $[1\bar{1}0]$ and $[110]$. Along $[1\bar{1}0]$, the stronger intrasublattice interaction for the SL B spins is linked to a higher propagation length and a larger transport for the LHM. This mode carries positive angular momentum, which finally accumulates at the $(0\bar{1}0)$ surface. Conversely, at the (010) surface, the RHM accumulates. The same logic applies for a temperature step in direction $[010]$, only that the direction dependent exchange interactions are reversed here.

Along the high-symmetry AFM directions $[100]$ and $[010]$, zero net magnetization can be expected and the small magnetization of 10^{-4} could be attributed to thermal fluctuations. We reiterate, that the sign convention exhibited by the SSE is conserved however, even though the magnitude is smaller. This indicates that the SNE is the reason for the net magnetization, opposed to thermal fluctuations.

Notably, a spatial oscillation in the magnetization is visible. We attribute this to be caused by the open boundaries; it reminds of a standing wave for example.

Looking at the transversal profiles for temperature gradients in $[1\bar{1}0]$ and $[110]$, an

accumulation at the boundaries is visible as well. This magnetization, however, can entirely be attributed to the surface effects explained in Sec. 4.1.2. This can also be seen in the configuration in Fig. 4.12. The surface effects are visible in the hot region. Notably, the high population of a specific mode in the surface layer also drives a strong SSE at the surface, as can be seen in the cold region. The layer average in transversal (y) direction is then visible in Fig. 4.13.

For directions $[1\ 0\ 0]$ and $[0\ 1\ 0]$ no surface effects occur, thus the net magnetization can entirely be attributed to a purely magnonic SNE.

4.3.2 Spin currents

So far, we have only indirectly shown the SNE. Now, we consider a transverse spin current as a direct proof.

For that, we consider periodic boundaries in the transverse directions, in order to enable a free current without backflow.

We calculate the spin currents as explained in Sec. 4.2.2 according to Eqs. (2.46) to (2.48). In contrast, we are not calculating the spin current in the direction of the temperature step, but in the transverse direction. The results can be seen in Fig. 4.14.

The transverse direction here refers to the direction, achieved through a counter-clockwise rotation in regard to the longitudinal direction of $-\nabla T$. These are exactly the same directions as in Fig. 4.13.

In Fig. 4.14, we see spin currents in the warm region due to thermal fluctuations. Near the temperature step in directions $[1\ 0\ 0]$ and $[0\ 1\ 0]$, a small transversal spin current is visible. It decreases in the cold region with an increasing distance to the temperature step. Directions $[1\bar{1}\ 0]$ and $[1\ 1\ 0]$ also show a small signal, which is attributed to noise, as we are only considering the correlation between spins in a single time step.

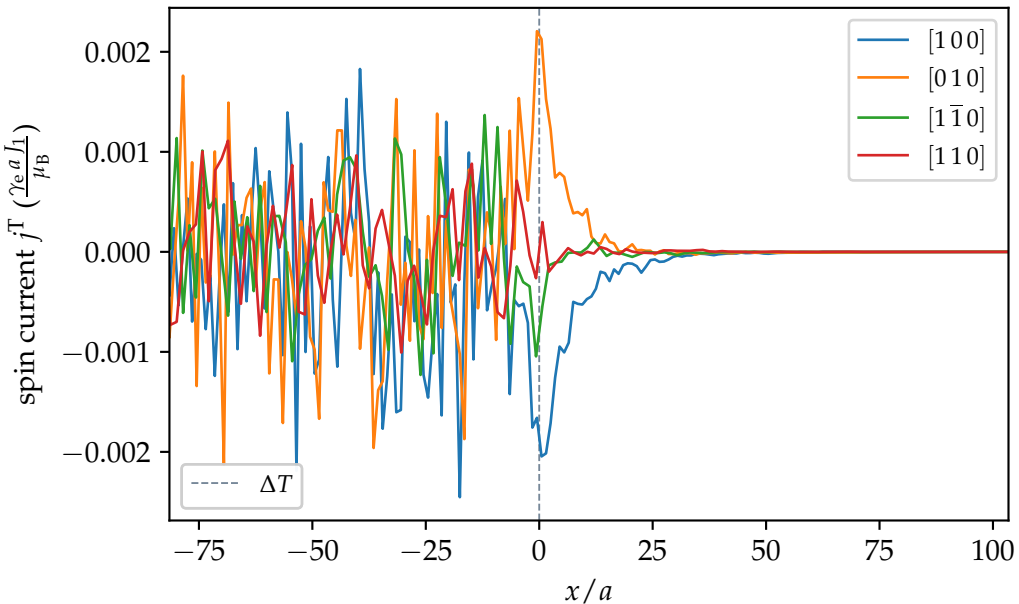


Figure 4.14: Transversal spin currents perpendicular to temperature steps along $[1\ 0\ 0]$, $[0\ 1\ 0]$, $[1\bar{1}\ 0]$, and $[1\ 1\ 0]$.

The observed transversal spin currents here support the claims made in regard to the boundary magnetization in Sec. 4.3.1. Considering a temperature step in [1 0 0], we have a strong SL A interaction in direction [1 1 0] and thus a strong transport of a negative angular momentum. As the transversal spin current is in [0 1 0] and correlates neighbouring spins, we can interpret the signal as a projection of the [1 1 0]-current along [0 1 0]. Similarly, a positive transport along [1 1 0] also results in a negative current in [0 1 0].

For the temperature step in [0 1 0] and its transversal direction [1 0 0], analogous arguments can be applied resulting in a positive spin current. The results are aligned with the boundary accumulations visible in Fig. 4.13.

These results concur with the results by Weissenhofer and Marmadoro [23]. They also find SSE in the diagonal crystallographic directions, and SNE in analogous directions as ours in the altermagnetic rutile phase of RuO₂.

In this toy model, we find transversal spin currents of a factor 5 smaller for the SNE compared to the SSE. The resulting net magnetization is about half in magnitude.

4.3.3 Magnon spectra

To further investigate the SNE and the surface effects discussed in Sec. 4.1.2, we consider magnon spectra in setups similar to the one presented in Fig. 4.12.

The magnon spectra are calculated according to the explanation in Sec. 4.1. A Fourier transform similar to Eq. (4.4) is performed only in the time domain to gain spectra at specific layers in the material. They are displayed in Fig. 4.15.

Basis for the data are simulations similar to the ones used for Fig. 4.13, only that they also provide a high time resolution. As before, 300 000 time steps were used to calculate the spectra.

Figure 4.15 shows three rows for temperature steps in different crystallographic directions, specifically [1 0 0], [1 1 0], and [1 1 0]. The three columns refer to different positions along the transversal directions as previously defined in Figs. 4.13 and 4.14. Each cell of the table then contains a magnon spectrum at the specific transversal layer. The first and last column show spectra at the opposite surfaces, while the centre column provides a spectrum in the center of the material.

To discuss these spectra, we also refer to the magnon bands depicted in Fig. 4.2. The band gap frequency corresponds to the first prominent peak observed after $\omega = 0$. Modes below this frequency are suppressed due to the material's anisotropy and nearest-neighbour antiferromagnetic exchange interactions. The highest allowed frequency is identified as the last distinct peak, beyond which all modes rapidly decay in amplitude. The range of frequencies which can be excited are direction dependent, as can be seen in the dispersion relation.

We consider the first row of Fig. 4.15, which shows spectra along [0 1 0] for a temperature step in [1 0 0]. In the previous sections, it has been discussed, that this geometry shows a clear SNE. In the center region, the spectrum shows an equal magnon density for the RHM and LHM. This is caused by equal excitation in the warm region and the governing AFM J_1 interaction.

Additionally, we expect the SNE currents to take place in the diagonal directions, the transverse current then being the projection on these directions. The spectra, however, are of the transverse directions, not showing the modes of the diagonal directions.

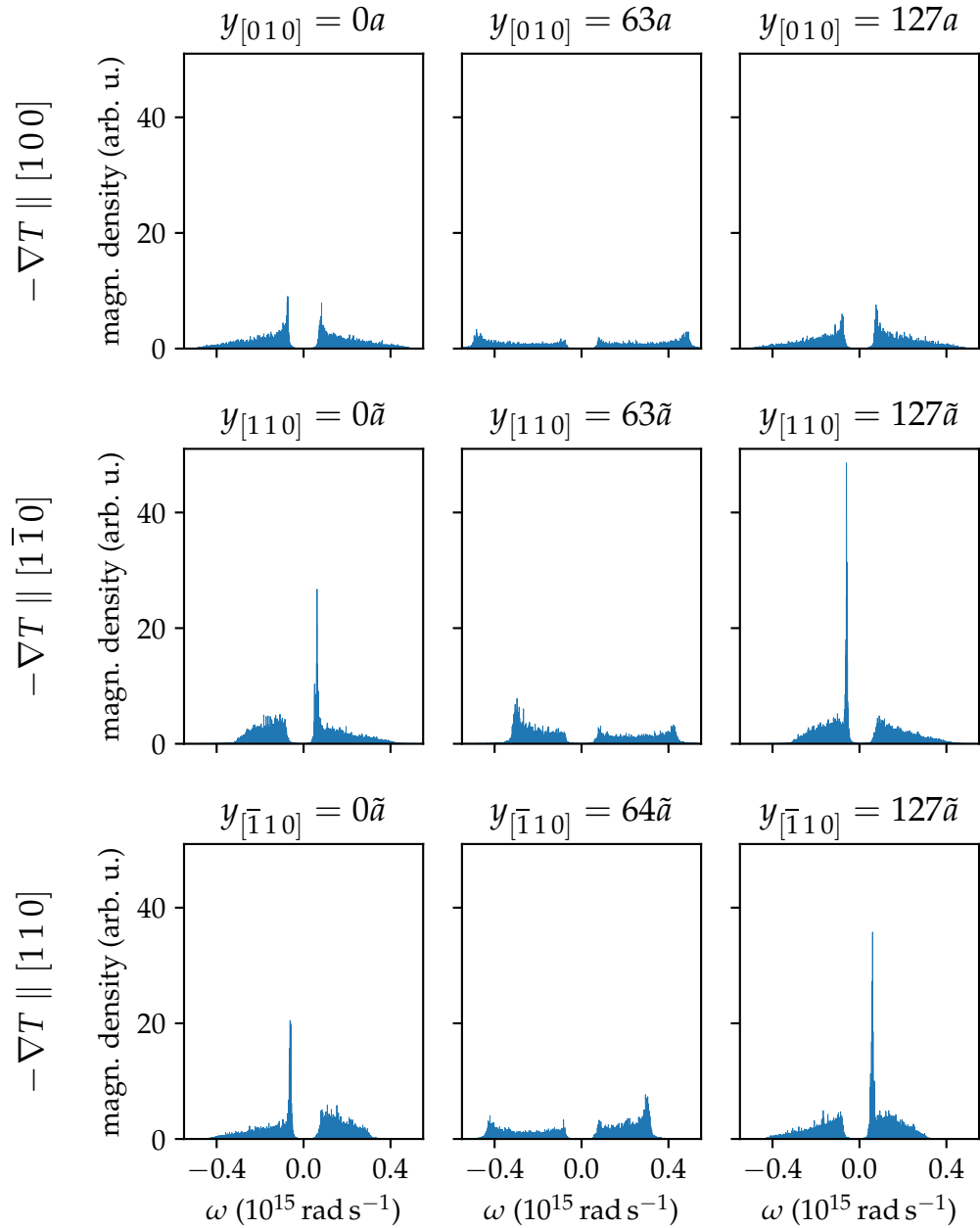


Figure 4.15: Magnon spectra at specific layers in transversal directions for temperature steps in different crystallographic directions.

The transversal surface layers however show a difference in magnon density between $y_{[010]} = 0a$ and $y_{[010]} = 127a$. The $(0\bar{1}0)$ surface has a higher magnon density of the LHM. This aligns with the positive accumulation at this edge, as visible in Fig. 4.13. Conversely, at (010) , a higher population of the RHM is linked to the negative magnetization. We note, that in both cases a high density can be observed for low frequencies, while at $y_{[010]} = 63a$, the magnon density is nearly constant, showing a small increase at the highest allowed frequencies, after which the amplitude decays rapidly.

Now we consider the situation for temperature steps in the diagonal directions $[1\bar{1}0]$ and $[\bar{1}10]$. Here, the magnon accumulation at the boundary visible in Fig. 4.13, as well as the spectra shown in Fig. 4.15 are attributed to surface effects in the tilted

setup instead of the SNE. As before, the spectra in Fig. 4.15 concur with the dispersion relations depicted in Fig. 4.2, as the highest excited frequencies and the band gap are the same. In the center region, the magnon density of the highest frequencies is greater than for the other frequencies, being particularly large at the highest allowed frequency of the lower band. This behaviour is no longer symmetric for $\pm\omega$, as the modes are non-degenerate at the edge of the BZ, in contrast to the [0 1 0] direction.

At the surfaces, the spectra exhibit a prominent peak at the lowest allowed frequency of different bands. If we consider for example $y_{[110]} = 0$, the peak is visible in the lowest allowed frequency of the RHM. This mode carries negative angular momentum, which explains why the magnon accumulation at this boundary is negative.

4.4 Relativistic effects: Dzyaloshinskii-Moriya interaction

As weak ferromagnetism due to the Dzyaloshinskii-Moriya interaction (DMI) plays a role in many materials, simulations with this second order exchange as explained in Sec. 2.2.2 have been performed.

We reiterate that our simple toy model cannot incorporate DMI without breaking the altermagnetic symmetry, as further explained in Sec. 2.2.2. The following results therefore have to be considered with care.

4.4.1 Equilibrium properties

First, the effect of the DMI on the equilibrium state is considered. For that, simulations at a temperature of $k_B T = 2 \text{ meV}$ with periodic boundary conditions are compared.

In Fig. 4.16, the average spin orientation for each SL is depicted for different system parameters. The average x -component is always zero and not shown here.

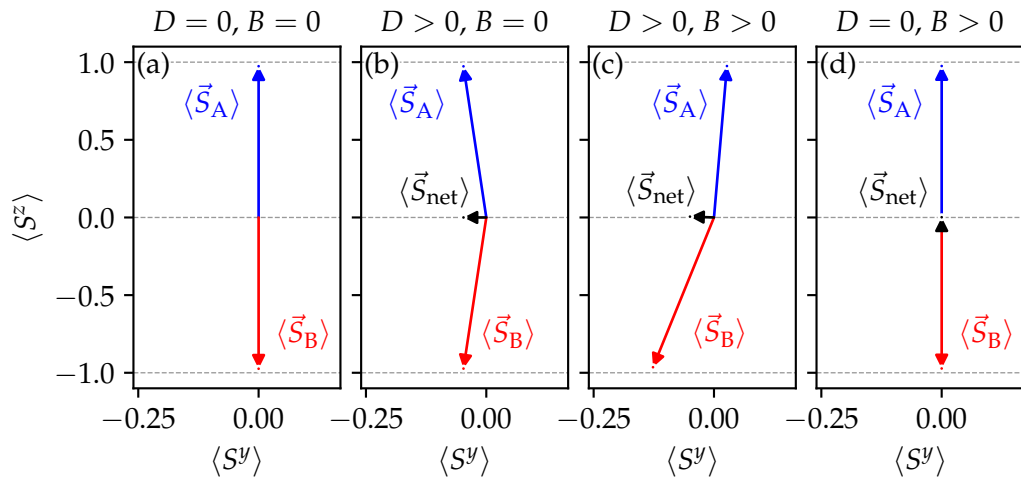


Figure 4.16: Schematic vector representation of the average spin components for different system parameters. For $D > 0$, $D = 2 \text{ meV}$ is used.

Without external magnetic field and antisymmetric exchange, the model shows no net magnetization in y -direction as visible in (a). The spins precess around the easy axis, and the in-plane components are zero in average. Because of thermal perturbation, the spins are deviated from their ground state and their absolute z -components are slightly below 1.

With the introduction of DMI with $\vec{D} = D \cdot \vec{e}_z$, we see a canting in $-y$ -direction as seen in (b). This canting was expected, as the system tries to minimize the energy Eq. (2.9). As a result, a small net magnetization in $-y$ -direction is observed, displaying weak ferromagnetism [36]. Due to the canting, the absolute values of the averaged z -components slightly decrease.

Window (c) shows the case with DMI and an external magnetic field. In this case, the averaged SL A spin has a positive component along positive y , while the SL B spin has an even greater negative y -component. This behaviour can be explained by the interaction between the DMI and Zeeman term. The system balances the easy-axis anisotropy, the y -canting, and the magnetic field, which results in the shown configuration. Without magnetic field, DMI causes a tilting, until the easy-axis anisotropy and DMI energy terms are of same magnitude. With an external field $B > 0$, positive z -components are more energetically beneficial, resulting in a decrease in the negative z -component of SL B and an increase in SL A. The result is the configuration which is shown. Note, that the canting angle between SL A and B stays the same, the directions relative to the easy-axis are just rotated. This setup results in a magnetization in the y - z -plane.

To compare this situation, the fourth window (d) shows the case without DMI but with an external magnetic field. Here, there is a small net magnetization as also shown in Fig. 4.1, which can be explained by different precession amplitudes due to the magnetic field. Notably, the net magnetization in z -direction is smaller in this case than when we consider the relativistic DM exchange. This is caused by the canting, which already allows a deviation from the antiparallel state.

All the explained effects are enhanced, when considering a higher relativistic interaction of $D = 5\text{ meV}$ instead of $D = 2\text{ meV}$.

Next, the magnon dispersion relation was determined according to the description in Sec. 4.1. They are depicted in Fig. 4.17 for the different crystallographic directions. The left column of the figure shows the dispersion relations without DMI, while the right column shows the dispersion relations with DMI.

The canted spins do not precess around the easy-axis any more. Before, their ground state orientation was along the easy-axis, now their ground states are slightly canted. This results in an elliptical precession around these directions [44, 88]. Therefore, as the precession no longer occurs around the z -easy-axis, the relevant in-plane components must be redefined with respect to the local canted equilibrium orientations rather than the canonical x and y axes, as described in Sec. 4.1. Thus, we redefine the in-plane components. As there is no canting along x , only the y -component is redefined using $S^y \mapsto \cos(\theta)S^y \pm \sin(\theta)S^z$, where θ is the deviation angle from the easy-axis and the sign \pm depends on the SL. It was found, that there is no notable difference in the dispersion, when considering the new in-plane components compared to just using the canonical components, as the deviation angle is below 7° for all DMI-strengths considered.

We first considered a DM-exchange of $D = 2\text{ meV}$, which proved to be too small to properly resolve splitting at the Γ -point, especially in regard to the strong easy-axis anisotropy of $d_z = 2\text{ meV}$. This is why we increased the relativistic exchange to

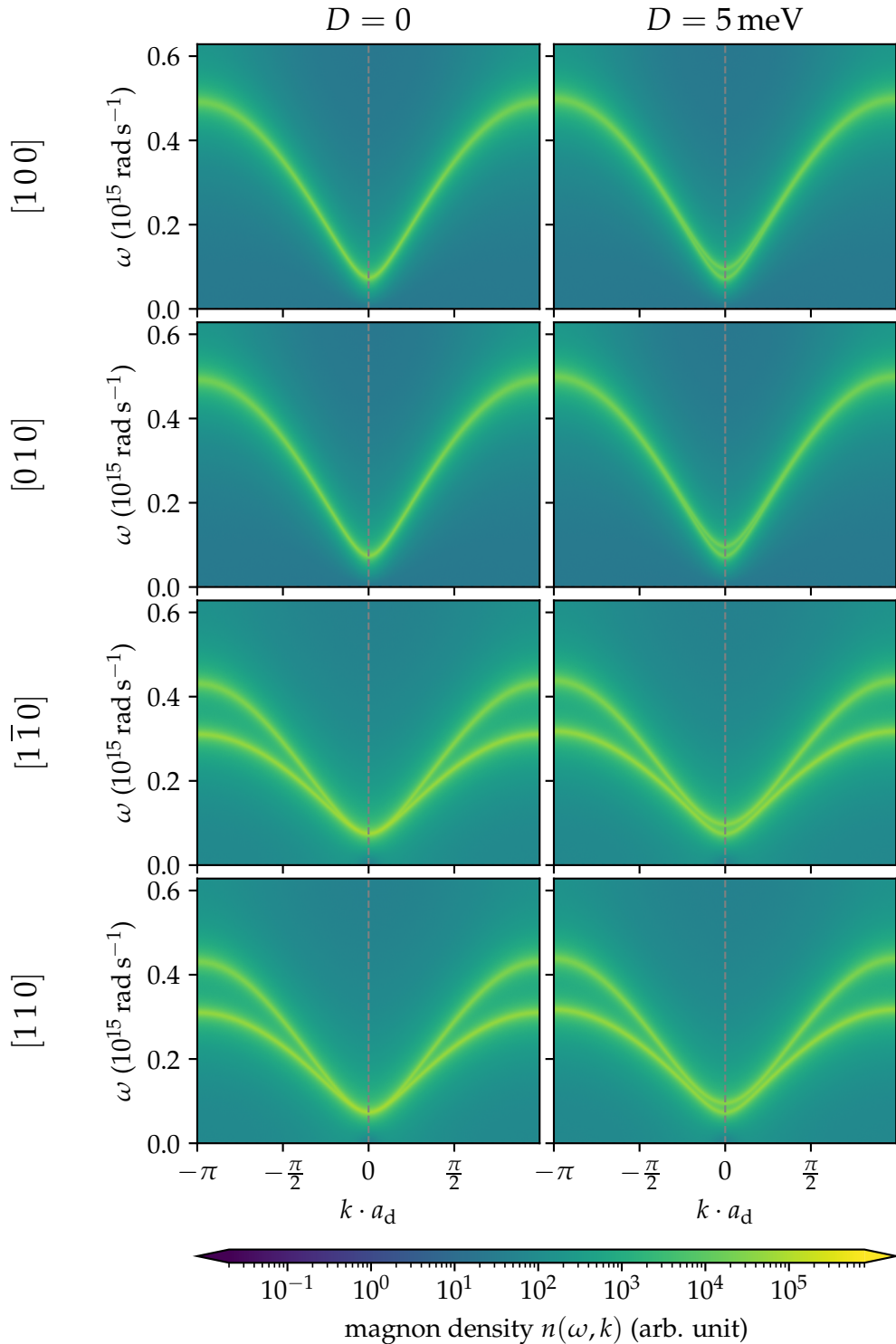


Figure 4.17: Magnonic dispersion relation in equilibrium for different crystallographic directions without DMI and with a DM exchange constant of $D = 5 \text{ meV}$. Here, $a_d = a$ for $[100]$ and $[010]$ and $a_d = \tilde{a}$ for $[1\bar{1}0]$ and $[110]$.

$D = 5 \text{ meV}$, which is the value used for Fig. 4.17.

To properly discern the effects exhibited by the sample with DMI, the depiction of the dispersion relations has been adjusted in Fig. 4.17, compared to for example

Fig. 4.2. Instead of showing different signs for the frequencies, which is helpful for assigning bands to different modes, here the absolute frequencies are shown. Methodically, this was done, by adding the magnon densities of the same absolute frequency, i.e. $n(\omega \geq 0) \mapsto n(+\omega) + n(-\omega)$. Consequently, the magnon density caps have been adjusted, as visible from the colourbar in Fig. 4.17.

Comparing the dispersions along the different directions with and without DMI, the most prominent effect is splitting at the Γ -point ($k = 0$), lifting the degeneracy. The direct comparison shows, that the source of this splitting is spin-orbit coupling, implemented with the relativistic DMI. With greater distance to the Γ -point, the relativistic splitting decreases, which can be clearly seen considering directions [1 0 0] and [0 1 0], where the AFM bands are degenerate again for larger k -values. The altermagnetic directions [1 $\bar{1}$ 0] and [1 1 0] exhibit splitting near the Γ -point due to DMI, and further away due to the anisotropic, altermagnetic exchange interactions.

These results concur with an analysis of altermagnetic splitting in hematite, based on linear spin-wave theory [89], where they also find splitting at the Γ -point, when considering the DMI.

The relativistic splitting here lifts a specific band near the Γ -point. Specifically, the minimum energy to excite magnons, i.e. the band gap stays constant for the studied strengths of antisymmetric exchange. For [1 $\bar{1}$ 0], the LHM is slightly lifted up, and for [1 1 0], the RHM is lifted up. Moreover, specifically considering $k \rightarrow \pm\pi/a_d$, a slight increase in energy of all modes is visible compared to the case with no DMI present.

We do not observe, nonreciprocity $\omega(k) \neq \omega(-k)$, which can occur due to DMI [90, 91].

Importantly, we find that the effects of DMI do not obscure the altermagnetic splitting [89].

4.4.2 Spin Seebeck effect

Apart from the equilibrium configuration of the toy model with DMI, we also studied the effects on a dynamic effect: the SSE

Analogous to Sec. 4.2, we show profiles of the magnon accumulation. Figure 4.18 shows the z -component of the magnon accumulation according to definition Eq. (2.49) for six different cases. The first column is without relativistic interactions, the second and third column are for different strengths D of the DMI.

The cases without DMI have been thoroughly discussed in Sec. 4.2. We will therefore consider the magnon accumulation with DMI. Its profile qualitatively looks the same as without DMI. For the cases with DMI, faster exponential decays of the magnon accumulation in the cold region can be observed. This effect is far more pronounced in the case with greater DMI of $D = 5$ meV.

We observe the same peak heights for all cases. This is attributed to the absolute reduction of the spin z -component of the different SLs compensating. The cause of the SSE can then still be attributed to different amounts of transport due to the specific anisotropy of the intrasublattice exchange interactions and different propagation lengths. Particularly, DMI does not enable a magnon accumulation in the z -component for any direction, which previously did not show SSE already.

Notable differences between the plots for different strengths of the relativistic effect are visible, when we consider a magnetic field $B > 0$. The DMI seems to increase

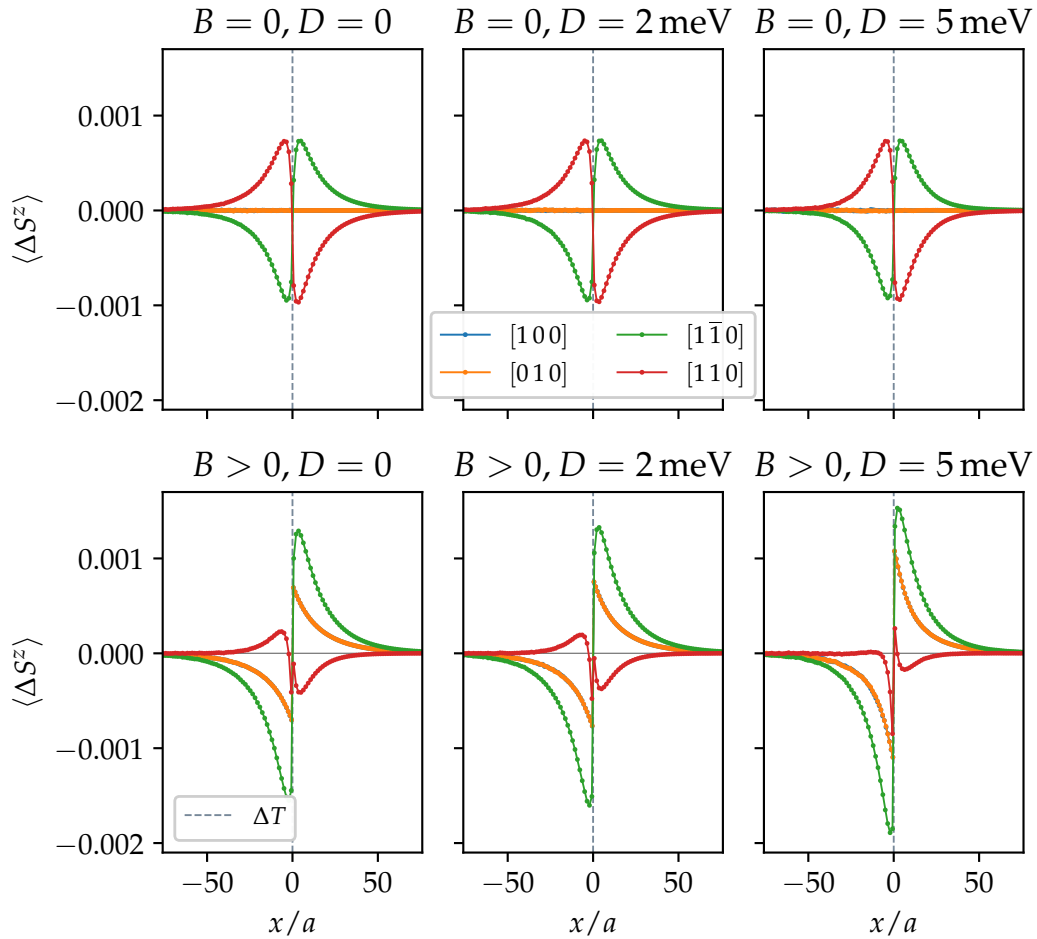


Figure 4.18: Averaged z -component of magnon accumulation in quasi-equilibrium for different parameters along different crystallographic directions.

the effect of the external magnetic field. With DMI, we observe an increase in peak magnon accumulations for directions $[1\ 0\ 0]$, $[0\ 1\ 0]$, and $[1\bar{1}\ 0]$ which already show greater accumulations compared to the case without external field. Direction $[1\ 1\ 0]$ shows lower magnon accumulations with an external field. With DMI, this effect is enlarged. For $D = 5$ meV, one even observes a suppression of the positive accumulation on the left.

Before explaining the graphs of the case with magnetic field and DMI, we will shortly repeat the explanation for the behaviour without DMI. With an external magnetic field, the population of the LHM, which carries positive angular momentum, is increased, while the population of the RHM is decreased due to the band shift. This results in an increased transport for $[1\bar{1}\ 0]$, as LH magnons are predominantly responsible for the magnon accumulation here. In the case of $[1\ 1\ 0]$, the RHM is responsible, which is why the magnon accumulation is decreased, and for the $[1\ 0\ 0]$ and $[0\ 1\ 0]$, the imbalance in magnon populations in the warm region enables SSE in the first place.

The DMI seems to further enhance the impact of this effect. The precession in one SL is further suppressed compared to the other SL, which then results in an enhanced SSE in one direction, and a smaller SSE in the perpendicular direction.

As DMI enables a finite canting in $-y$ -direction, and thus, a net magnetization, the SSE is also observable in the y -component. Qualitatively, the same effects have been observed for $D = 2$ meV and $D = 5$ meV. In Fig. 4.19, we show the spatial profile for $D = 5$ meV as the effect is more pronounced.

Without canting due to DMI, there is no net magnetization in x - or y -direction in average. With DMI, the material shows weak ferromagnetism in y -direction [36].

Ferromagnets are well known to exhibit a SSE [29] due to the well-defined chirality of their magnons. Similarly, excited spins precess around their ground state orientation, effectively reducing their absolute average y -component. Thus, both magnon modes carry a positive y angular momentum. As magnons are only excited in the hot region on the left due to thermal perturbation, the transport over the temperature step results in a positive magnon accumulation in the cold region, while the deficit is visible by the negative sign.

Note, that we consistently see a high net magnetization difference $\langle \Delta S^y \rangle$, which is larger for the y component than for the z component for many directions. Here, this is explained by the fact that all magnons carry positive y angular momentum across the temperature step and the canting is quite substantial for $D = 5$ meV. For different system parameters, especially a smaller relativistic influence with $D = 2$ meV, the magnon accumulation in the z -component is larger.

Taking a closer look, specifically at the inset axes, it is visible that peak values are slightly larger for $[100]$ and $[010]$. In the previous study of the SSE, it became clear that the magnitude of magnon accumulation is connected to a stronger exchange interaction and a stronger transport of a specific mode. Here, these directions are governed by the AFM exchange constant J_1 , which is larger than the intrasublattice exchange energies. It is therefore plausible, that a greater transport across the temperature step takes place, and since all magnons carry the same amount of y angular momentum with the same sign, the peak magnon accumulation is larger.

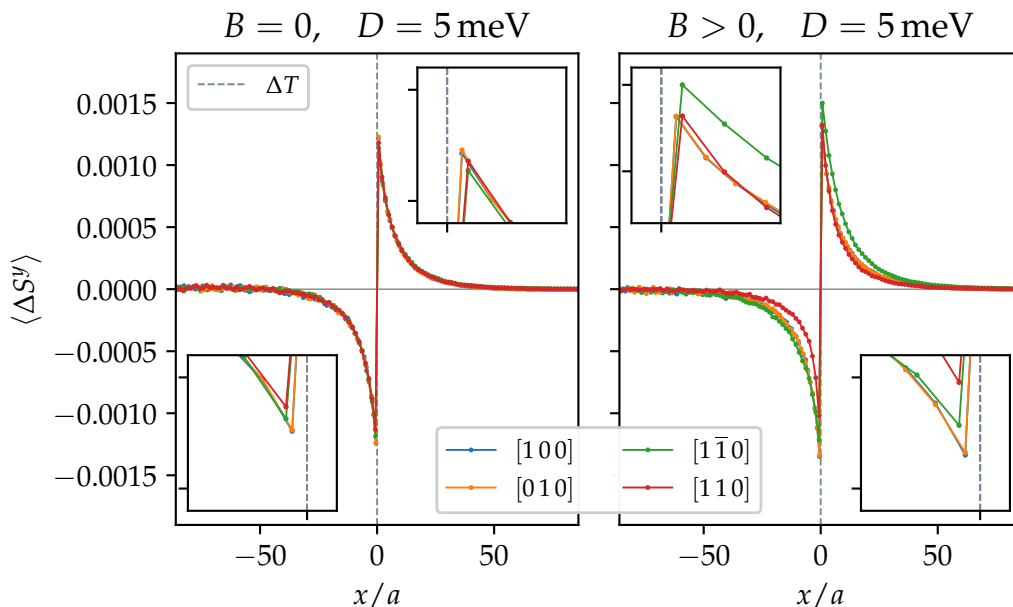


Figure 4.19: Averaged y -component of magnon accumulation in quasi-equilibrium with relativistic effects, with and without magnetic field, along different crystallographic directions.

We believe that the small peak difference for $[1\bar{1}0]$ and $[110]$ is attributed to the surface at the temperature step, which has been discussed before. The first cold layer consists only of SL B atoms, while the last warm layer only consists of SL A atoms. These are directly connected with exchange interaction J_1 .

When additionally introducing an external field, the magnon bands shift, resulting in a higher population of SL B magnons. This results in a higher transport and in an increased peak value for $[1\bar{1}0]$. The absolute value differs in the cold and warm region due to the aforementioned surface effect at the temperature step.

We generally observe higher peak values compared to the case without magnetic field. Considering Fig. 4.16, we note that the LH magnons carry a higher absolute y angular momentum compared to the RH magnons, as the deviation from the easy-axis is larger. Thus, the peak values are increased, as SL B magnons already govern the transport for $[1\bar{1}0]$, $[100]$, and $[010]$. As the transport along $[110]$ is governed by the SL A mode, the effect is decreased for this direction.

Chapter 5

Conclusion and Outlook

Altermagnets (AMs) are an emerging class of magnetic materials, exhibit antiferromagnetic and ferromagnetic properties, offering significant advantages in the field of spintronics [8–11].

The present work aims to provide useful insight into this new class of magnetic material by studying certain effects in a simplified model. Langevin dynamics simulations based on the stochastic Landau-Lifshitz-Gilbert equation are performed to study the altermagnetic model in different situations, providing insight in microscopic mechanisms behind spin excitations in altermagnets.

The two-dimensional altermagnetic toy model is based on a checkerboard lattice with two opposing sublattices with anisotropic intrasublattice exchange interactions, fulfilling the altermagnetic symmetry properties. This work links the direction dependent magnon dispersion relation to the anisotropic exchange interactions, providing an intuitive understanding of the direction-dependent splitting of magnon bands.

Introducing an external magnetic field parallel to the easy-axis, reveals a shift in the bands, thereby changing magnon populations of specific modes and resulting in a net magnetization of the material. The interplay between band shifts, magnon populations and different magnon modes can then be used to understand the fundamental cause of the spin Seebeck effect. Additionally, the magnon propagation lengths and the transport along a temperature step are studied for the different magnon modes along the directions exhibiting the effect in this altermagnetic material, further supporting the dominating role of a direction specific mode.

Furthermore, this thesis provides direct evidence of the spin Seebeck effect by determining a nonzero spin current when finite magnon accumulations build up around the temperature step.

Moreover, the novel spin Nernst effect is studied by means of atomistic spin dynamics simulations. The investigation yields nonzero magnon accumulations at surfaces corresponding to a magnon accumulation. By comparing with data on the edges of the material, the accumulation can be identified as a surface effect or as a result of the spin Nernst effect, depending on the direction. Additionally, this work provides direct proof of the effect by identifying a purely magnonic spin current, which is present for specific directions.

Lastly, this study considers the relativistic Dzyaloshinskii-Moriya interaction (DMI), analysing its influence on the equilibrium state and spin Seebeck effect, with and without an additional magnetic field. The specific implementation of the interaction in this work breaks the altermagnetic symmetry.

Future endeavours can focus on a number of topics, regarding the properties of altermagnets, the spin Seebeck effect and spin Nernst effect, and the influence of the

Dzyaloshinskii-Moriya interaction. Notably, establishing a direct link between the spin Nernst effect [14] in altermagnetic materials and the momentum-space Berry curvature that their symmetry-broken, spin-split bands produce [92] is a desirable goal.

Specifically, regarding this work, a more gradual temperature change instead of a temperature step can be of interest to reduce surface effects at the temperature step. Additionally, the effect of the Dzyaloshinskii-Moriya interaction on altermagnetic materials can further be studied without breaking the altermagnetic symmetry. This was already done in a similar model with an easy-plane, used in a recent paper [49].

An important goal is the conclusive experimental proof of the magnonic spin Nernst effect, as previous attempts [13] experienced difficulties unambiguously assigning signals to the effect [14].

Acknowledgements

I would like to thank everyone who has accompanied and supported me throughout the course of my degree.

I am very grateful to Prof. Dr. Ulrich Nowak for giving me the opportunity to carry out this scientific work within his group, and for the valuable discussions whenever I had new preliminary results to share.

My heartfelt gratitude goes to Moumita Kundu, my supervisor, for her continuous support and guidance over the past months. I greatly appreciate all the time she dedicated to answering my questions and helping me solve problems. Our discussions about various phenomena were not only enjoyable but also instrumental in strengthening my understanding of the subject. Thank you for proofreading my work, and for your understanding of my preference to work from home, especially during the writing process.

I would also like to thank all members of the Nowak Group for sharing the office with me and for taking an interest in my progress. The group excursion to the Seealpsee was a lot of fun, and I truly enjoyed getting to know some of you better.

I am very thankful to my friends for their support, even though I cannot name everyone here. A special thanks goes to Jermaine Breuer, who I can always count on for advice and a listening ear in both difficult and hopeful times. I would like to thank him, and all the people who have helped shape me into who I am, as well as those who have shared a part of their lives with me.

Finally, I would like to express my deepest gratitude to my family, especially my mother and brothers, for their constant understanding, support, stability, and love.

References

- ¹International Energy Agency, *Energy and AI*, <https://www.iea.org/reports/energy-and-ai>, IEA, Paris. Licence: CC BY 4.0, 2025.
- ²S. Bhat, *A Seminar Report on GPUs in AI: NVIDIA's Dominance and the Rising Competition* (Apr. 2025).
- ³S. A. Wolf, D. D. Awschalom, R. A. Buhrman, J. M. Daughton, S. von Molnár, M. L. Roukes, A. Y. Chtchelkanova and D. M. Treger, 'Spintronics: a spin-based electronics vision for the future', *Science* **294**, 1488–1495 (2001).
- ⁴A. Kirihara, K.-i. Uchida, Y. Kajiwara, M. Ishida, Y. Nakamura, T. Manako, E. Saitoh and S. Yorozu, 'Spin-current-driven thermoelectric coating', *Nature Materials* **11**, 686–689 (2012).
- ⁵G. E. W. Bauer, E. Saitoh and B. J. van Wees, 'Spin caloritronics', *Nature Materials* **11**, 391–399 (2012).
- ⁶S. R. Boona, R. C. Myers and J. P. Heremans, 'Spin caloritronics', *Energy Environ. Sci.* **7**, 885–910 (2014).
- ⁷V. Baltz, A. Manchon, M. Tsoi, T. Moriyama, T. Ono and Y. Tserkovnyak, 'Antiferromagnetic spintronics', *Rev. Mod. Phys.* **90**, 015005 (2018).
- ⁸R. Tamang, S. Gurung, D. P. Rai, S. Brahimi and S. Lounis, 'Altermagnetism and Altermagnets: A Brief Review', *Magnetism* **5**, 10.3390/magnetism5030017 (2025).
- ⁹L. Šmejkal, J. Sinova and T. Jungwirth, 'Emerging Research Landscape of Altermagnetism', *Phys. Rev. X* **12**, 040501 (2022).
- ¹⁰L. Šmejkal, J. Sinova and T. Jungwirth, 'Beyond Conventional Ferromagnetism and Antiferromagnetism: A Phase with Nonrelativistic Spin and Crystal Rotation Symmetry', *Phys. Rev. X* **12**, 031042 (2022).
- ¹¹I. Mazin, 'Altermagnetism Then and Now', *Physics* **17**, 4 (2024).
- ¹²U. Nowak, 'Classical spin models', in *Handbook of magnetism and advanced magnetic materials*, Vol. 2, edited by H. Kronmüller and S. Parkin (John Wiley & Sons, Chichester, 2007), pp. 858–876.
- ¹³Y. Shiomi, R. Takashima and E. Saitoh, 'Experimental evidence consistent with a magnon Nernst effect in the antiferromagnetic insulator MnPS₃', *Phys. Rev. B* **96**, 134425 (2017).
- ¹⁴H. Zhang and R. Cheng, 'A perspective on magnon spin Nernst effect in antiferromagnets', *Applied Physics Letters* **120**, 10.1063/5.0084359 (2022).
- ¹⁵T. Dietl, D. D. Awschalom, M. Kaminska and H. Ohno, eds., *Spintronics*, Vol. 82, Semiconductors and Semimetals (Academic Press, Amsterdam, 2008).
- ¹⁶E. Y. Vedmedenko, R. K. Kawakami, D. D. Sheka, P. Gambardella, A. Kirilyuk, A. Hirohata, C. Binek, O. Chubykalo-Fesenko, S. Sanvito, B. J. Kirby, J. Grollier, K. Everschor-Sitte, T. Kampfrath, C.-Y. You and A. Berger, 'The 2020 magnetism roadmap', *Journal of Physics D: Applied Physics* **53**, 453001 (2020).

- ¹⁷O. Fedchenko, J. Minár, A. Akashdeep, S. W. D'Souza, D. Vasilyev, O. Tkach, L. Odenbreit, Q. Nguyen, D. Kutnyakhov, N. Wind, L. Wenthaus, M. Scholz, K. Rossnagel, M. Hoesch, M. Aeschlimann, B. Stadtmüller, M. Kläui, G. Schönhense, T. Jungwirth, A. B. Hellenes, G. Jakob, L. Šmejkal, J. Sinova and H.-J. Elmers, 'Observation of time-reversal symmetry breaking in the band structure of altermagnetic ruo2', *Science Advances* **10**, eadj4883 (2024).
- ¹⁸A. Wilkins, 'The existence of a new kind of magnetism has been confirmed', *New Scientist* (2024), <https://www.newscientist.com/article/2417255-the-existence-of-a-new-kind-of-magnetism-has-been-confirmed/>.
- ¹⁹M. Bischoff, 'Altermagnetismus: Eine neue Form von Magnetismus wurde entdeckt', *Spektrum der Wissenschaft* (2024), <https://www.spektrum.de/news/altermagnetismus-eine-neue-form-von-magnetismus-wurde-entdeckt/2208043>.
- ²⁰V. Zota, 'Altermagnetismus: Forscher weisen neue magnetische Phase in Mangantellurid nach', *heise online* (2024), <https://www.heise.de/news/Neue-Art-des-Magnetismus-Altermagnetische-Zustaende-erstmals-sichtbar-gemacht-10199942.html>.
- ²¹R. Schmidhuber, 'Toy model for an altermagnet dispersion relation and spin Seebeck effect', Bachelor's Thesis (Universität Konstanz, 2025).
- ²²M.-H. Zhang, L. Xiao and D.-X. Yao, *Topological magnons in a collinear altermagnet*, 2024.
- ²³M. Weißenhofer and A. Marmodoro, 'Atomistic spin dynamics simulations of magnonic spin seebeck and spin nernst effects in altermagnets', *Phys. Rev. B* **110**, 094427 (2024).
- ²⁴S. Hunklinger, *Festkörperphysik*, German, 3rd ed. (Oldenbourg Wissenschaftsverlag GmbH, München, 2011).
- ²⁵S. Blundell, *Magnetism in Condensed Matter* (Oxford University Press, New York, London, 2001).
- ²⁶D. Meschede, *Gerthsen Physik*, German, 25th ed. (Springer-Verlag, Berlin Heidelberg New York, 2015).
- ²⁷T. Fließbach, *Quantenmechanik - Lehrbuch zur Theoretischen Physik III*, German, 6th ed. (Springer-Verlag, Berlin Heidelberg New York, 2018).
- ²⁸F. Schwabl, *Quantenmechanik (QM I) - Eine Einführung*, German, 7th ed. (Springer-Verlag, Berlin Heidelberg New York, 2007).
- ²⁹U. Ritzmann, 'Modeling spincaloric transport: magnon accumulation and propagation', PhD thesis (Universität Konstanz, 2015).
- ³⁰H. Haken and H. C. Wolf, *Atom- und Quantenphysik - Einführung in die experimentellen und theoretischen Grundlagen*, German, 8th ed. (Springer-Verlag, Berlin Heidelberg New York, 2004).
- ³¹J. J. Sakurai and J. Napolitano, *Modern Quantum Mechanics*, 3rd ed. (Cambridge University Press, 2020).
- ³²W. Demtröder, *Experimentalphysik 3 - Atome, Moleküle und Festkörper*, German, 5th ed. (Springer-Verlag, Berlin Heidelberg New York, 2016).
- ³³W. Heisenberg, 'Zur Theorie des Ferromagnetismus', *Zeitschrift für Physik* **49**, 619–636 (1928).

- ³⁴R. Gross and A. Marx, *Festkörperphysik*, German, 4th ed. (Walter de Gruyter GmbH, Berlin/Boston, 2023).
- ³⁵R. Skomski, *Simple Models of Magnetism* (Oxford University Press, New York, London, 2008).
- ³⁶I. Dzyaloshinskii, ‘A thermodynamic theory of “weak” ferromagnetism of anti-ferromagnetics’, *Journal of Physics and Chemistry of Solids* **4**, 241–255 (1958).
- ³⁷T. Moriya, ‘Anisotropic superexchange interaction and weak ferromagnetism’, *Phys. Rev.* **120**, 91–98 (1960).
- ³⁸L. D. Landau and E. M. Lifshitz, ‘On the theory of the dispersion of magnetic permeability in ferromagnetic bodies’, *Physikalische Zeitschrift der Sowjetunion* **8**, 153–169 (1935).
- ³⁹M. Evers, ‘Two antagonizing aspects of spin transport : spin-wave localization and spin superfluidity’, PhD thesis (Universität Konstanz, 2019).
- ⁴⁰T. L. Gilbert, ‘A phenomenological theory of damping in ferromagnetic materials’, *IEEE Transactions on Magnetics* **40**, Originally written in 1955; published as part of the Classics in Magnetics series, 3443–3449 (2004).
- ⁴¹W. Nolting, *Grundkurs Theoretische Physik 7 - Viel-Teilchen-Theorie* (Springer-Verlag, Berlin Heidelberg New York, 2014).
- ⁴²F. Bloch, ‘Zur Theorie des Ferromagnetismus’, *Zeitschrift für Physik* **61**, 206–219 (1930).
- ⁴³S. M. Rezende, *Fundamentals of Magnonics*, 1st ed., Vol. 969, Lecture Notes in Physics (Springer Cham, 2020).
- ⁴⁴J. Han, R. Cheng, L. Liu, H. Ohno and S. Fukami, ‘Coherent antiferromagnetic spintronics’, *Nature Materials* **22**, 684–695 (2023).
- ⁴⁵S. M. Rezende, A. Azevedo and R. L. Rodríguez-Suárez, ‘Introduction to antiferromagnetic magnons’, *Journal of Applied Physics* **126**, 151101 (2019).
- ⁴⁶Y. Shiota, T. Taniguchi, D. Hayashi, H. Narita, S. Karube, R. Hisatomi, T. Moriyama and T. Ono, ‘Handedness manipulation of propagating antiferromagnetic magnons’, *Nature Communications* **15**, 9750 (2024).
- ⁴⁷I. Mazin (The PRX Editors), ‘Editorial: Altermagnetism—a New Punch Line of Fundamental Magnetism’, *Phys. Rev. X* **12**, 040002 (2022).
- ⁴⁸H. Ibach and H. Lüth, *Festkörperphysik - Einführung in die Grundlagen*, German, 7th ed. (Springer-Verlag, Berlin Heidelberg New York, 2009).
- ⁴⁹S. Khatua, V. P. Kravchuk, K. V. Yershov and J. van den Brink, ‘Magnon topology driven by altermagnetism’, [arXiv, 10.48550/arXiv.2507.17822](https://arxiv.org/abs/10.48550/arXiv.2507.17822) (2025).
- ⁵⁰K. Uchida, J. Xiao, H. Adachi, J. Ohe, S. Takahashi, J. Ieda, T. Ota, Y. Kajiwara, H. Umezawa, H. Kawai, G. E. W. Bauer, S. Maekawa and E. Saitoh, ‘Spin Seebeck insulator’, *Nature Materials* **9**, 894–897 (2010).
- ⁵¹H. Adachi, K.-i. Uchida, E. Saitoh and S. Maekawa, ‘Theory of the spin Seebeck effect’, *Reports on Progress in Physics* **76**, 036501 (2013).
- ⁵²Oersted, ‘Notiz von neuen electrisch - magnetischen Versuchen des Herrn Seebeck in Berlin’, *Annalen der Physik* **73**, 430–432 (1823).
- ⁵³K. Uchida, S. Takahashi, K. Harii, J. Ieda, W. Koshibae, K. Ando, S. Maekawa and E. Saitoh, ‘Observation of the spin Seebeck effect’, German, *Nature* **455**, 778–781 (2008).

- ⁵⁴C. M. Jaworski, J. Yang, S. Mack, D. D. Awschalom, J. P. Heremans and R. C. Myers, ‘Observation of the spin-Seebeck effect in a ferromagnetic semiconductor’, *Nature Materials* **9**, 898–903 (2010).
- ⁵⁵U. Ritzmann, D. Hinzke and U. Nowak, ‘Thermally induced magnon accumulation in two-sublattice magnets’, *Phys. Rev. B* **95**, 054411 (2017).
- ⁵⁶K. Tauber, M. Gradhand, D. V. Fedorov and I. Mertig, ‘Extrinsic Spin Nernst Effect from First Principles’, *Phys. Rev. Lett.* **109**, 026601 (2012).
- ⁵⁷S. Meyer, Y.-T. Chen, S. Wimmer, M. Althammer, T. Wimmer, R. Schlitz, S. Geprägs, H. Huebl, D. Ködderitzsch, H. Ebert, G. E. W. Bauer, R. Gross and S. T. B. Goennenwein, ‘Observation of the spin nernst effect’, *Nature Materials* **16**, 977–981 (2017).
- ⁵⁸A. v. Ettingshausen and W. Nernst, ‘Ueber das Auftreten electromotorischer Kräfte in Metallplatten, welche von einem Wärmestrome durchflossen werden und sich im magnetischen Felde befinden’, *Annalen der Physik* **265**, 343–347 (1886).
- ⁵⁹S.-g. Cheng, Y. Xing, Q.-f. Sun and X. C. Xie, ‘Spin Nernst effect and Nernst effect in two-dimensional electron systems’, *Phys. Rev. B* **78**, 045302 (2008).
- ⁶⁰X. Liu and X. Xie, ‘Spin Nernst effect in the absence of a magnetic field’, *Solid State Communications* **150**, Spin Caloritronics, 471–474 (2010).
- ⁶¹Z. Ma, ‘Spin Hall effect generated by a temperature gradient and heat current in a two-dimensional electron gas’, *Solid State Communications* **150**, Spin Caloritronics, 510–513 (2010).
- ⁶²A. Dyrdał and J. Barnaś, ‘Intrinsic contribution to spin hall and spin nernst effects in a bilayer graphene’, *Journal of Physics: Condensed Matter* **24**, 275302 (2012).
- ⁶³S. Wimmer, D. Ködderitzsch, K. Chadova and H. Ebert, ‘First-principles linear response description of the spin Nernst effect’, *Phys. Rev. B* **88**, 201108 (2013).
- ⁶⁴P. Sheng, Y. Sakuraba, Y.-C. Lau, S. Takahashi, S. Mitani and M. Hayashi, ‘The spin Nernst effect in tungsten’, *Science Advances* **3**, e1701503 (2017).
- ⁶⁵V. A. Zyuzin and A. A. Kovalev, ‘Magnon Spin Nernst Effect in Antiferromagnets’, *Phys. Rev. Lett.* **117**, 217203 (2016).
- ⁶⁶R. Cheng, S. Okamoto and D. Xiao, ‘Spin Nernst Effect of Magnons in Collinear Antiferromagnets’, *Phys. Rev. Lett.* **117**, 217202 (2016).
- ⁶⁷A. Pires, ‘Magnon spin Nernst effect on the antiferromagnetic checkerboard lattice’, *Physics Letters A* **383**, 125887 (2019).
- ⁶⁸A. Shitade, ‘Spin accumulation in the spin Nernst effect’, *Phys. Rev. B* **106**, 045203 (2022).
- ⁶⁹K. E. Atkinson, W. Han and D. Stewart, *Numerical solution of ordinary differential equations* (John Wiley & Sons, Inc., Hoboken, NJ, 2009).
- ⁷⁰M. Kunze, ‘Mathematik 3 für den Studiengang Physik’, Vorlesungsskript, Fachbereich Mathematik und Statistik, Wintersemester 2023/24, Konstanz, 2023.
- ⁷¹A. Meister and T. Sonar, *Numerik, Eine lebendige und gut verständliche Einführung mit vielen Beispielen*, 1st ed. (Springer Spektrum, Berlin, Heidelberg, 2019), pp. XI+382.
- ⁷²M. Brokate, N. Henze, F. Hettlich, A. Meister, G. Schranz-Kirlinger and T. Sonar, ‘18. Numerik gewöhnlicher Differenzialgleichungen – Schritt für Schritt zur Trajektorie’, in *Grundwissen Mathematikstudium*, edited by M. Brokate, N. Henze, F. Hettlich, A. Meister, G. Schranz-Kirlinger and T. Sonar, 1st ed. (Springer Spektrum, Berlin, Heidelberg, 2016), pp. 655–699.

- ⁷³S. Selzer, ‘Simulations on the Dynamics of Complex Magnetic Nanostructures’, PhD thesis (Universität Konstanz, Konstanz, 2021), <http://nbn-resolving.de/urn:nbn:de:bsz:352-2-czom27gzwfxe2>.
- ⁷⁴B. Øksendal, *Stochastic Differential Equations: An Introduction with Applications*, 5th ed., Vol. 82 (Springer-Verlag, Heidelberg New York, Jan. 2000).
- ⁷⁵N. G. van Kampen, ‘Itô versus Stratonovich’, *Journal of Statistical Physics* **24**, 175–187 (1981).
- ⁷⁶Oregon State University, Department of Mathematics (Course MTH 657), § 7 *The Itô/Stratonovich Dilemma*, https://sites.science.oregonstate.edu/~restrepo/MTH657/Documents/AM4062_notes7.pdf (visited on 19/08/2025).
- ⁷⁷A. Donges, ‘Computer Simulations of Ultrafast Magnetic Phenomena’, PhD thesis (Universität Konstanz, Konstanz, 2018), <http://nbn-resolving.de/urn:nbn:de:bsz:352-2-18q202iyap3fx0>.
- ⁷⁸A. Donges, *cuteLLG Wiki Documentation*, Internal Wiki, Research Group Nowak, University of Konstanz, Accessible only to group members, 2019.
- ⁷⁹NVIDIA, *CUDA Toolkit Documentation*, (n.d.) <https://docs.nvidia.com/cuda/> (visited on 22/08/2025).
- ⁸⁰NVIDIA, *CUDA C++ Programming Guide*, version 13.0, (Aug. 2025) https://docs.nvidia.com/cuda/pdf/CUDA_C_Programming_Guide.pdf (visited on 22/08/2025).
- ⁸¹G. Venkat, H. Fangohr and A. Prabhakar, ‘Absorbing boundary layers for spin wave micromagnetics’, *Journal of Magnetism and Magnetic Materials* **450**, Perspectives on magnon spintronics, 34–39 (2018).
- ⁸²C. R. Harris, K. J. Millman, S. J. van der Walt, R. Gommers, P. Virtanen, D. Cournapeau, E. Wieser, J. Taylor, S. Berg, N. J. Smith, R. Kern, M. Picus, S. Hoyer, M. H. van Kerkwijk, M. Brett, A. Haldane, J. F. del Río, M. Wiebe, P. Peterson, P. Gérard-Marchant, K. Sheppard, T. Reddy, W. Weckesser, H. Abbasi, C. Gohlke and T. E. Oliphant, ‘Array programming with NumPy’, *Nature* **585**, 357–362 (2020).
- ⁸³J. Werner, C. Neef, C. Koo, A. Ponomaryov, S. Zvyagin and R. Klingeler, ‘Exceptional field dependence of antiferromagnetic magnons in LiFePO₄’, *Phys. Rev. B* **103**, 174406 (2021).
- ⁸⁴NumPy Developers, *Discrete Fourier Transform - NumPy v2.3 Manual*, Accessed: 2025-09-19, NumPy, (19th Sept. 2025) <https://numpy.org/doc/stable/reference/routines.fft.html>.
- ⁸⁵J. W. Cooley and J. W. Tukey, ‘An algorithm for the machine calculation of complex fourier series’, *Mathematics of Computation* **19**, 297–301 (1965).
- ⁸⁶W. H. Press, S. A. Teukolsky, W. T. Vetterling and B. P. Flannery, ‘Numerical recipes: the art of scientific computing’, in , 3rd ed. (Cambridge University Press, Cambridge, UK, Sept. 2007) Chap. 12–13, Ch. 12–13.
- ⁸⁷J. Cramer, U. Ritzmann, B.-W. Dong, S. Jaiswal, Z. Qiu, E. Saitoh, U. Nowak and M. Kläui, ‘Spin transport across antiferromagnets induced by the spin Seebeck effect’, *Journal of Physics D: Applied Physics* **51**, 144004 (2018).
- ⁸⁸H. Wang, Y. Xiao, M. Guo, E. Lee-Wong, G. Q. Yan, R. Cheng and C. R. Du, ‘Spin Pumping of an Easy-Plane Antiferromagnet Enhanced by Dzyaloshinskii–Moriya Interaction’, *Phys. Rev. Lett.* **127**, 117202 (2021).

- ⁸⁹R. Hoyer, P. P. Stavropoulos, A. Razpopov, R. Valentí, L. Šmejkal and A. Mook, ‘Altermagnetic splitting of magnons in hematite α –Fe₂O₃’, *Phys. Rev. B* **112**, 064425 (2025).
- ⁹⁰F. J. dos Santos, M. dos Santos Dias and S. Lounis, ‘Nonreciprocity of spin waves in noncollinear magnets due to the dzyaloshinskii-moriya interaction’, *Phys. Rev. B* **102**, 104401 (2020).
- ⁹¹R. L. Melcher, ‘Linear contribution to spatial dispersion in the spin-wave spectrum of ferromagnets’, *Phys. Rev. Lett.* **30**, 125–128 (1973).
- ⁹²T. Farajollahpour, R. Ganesh and K. V. Samokhin, ‘Berry curvature-induced transport signature for altermagnetic order’, *npj Quantum Materials* **10**, 77 (2025).
- ⁹³Python Software Foundation, *Python*, version 3.12.2, Programming language, Feb. 2024, <https://www.python.org/>.
- ⁹⁴Python Software Foundation, *Python*, version 3.12.7, Programming language, Oct. 2024, <https://www.python.org/>.
- ⁹⁵Anaconda software distribution, version 2.6.3, Computer software, Anaconda, Sept. 2024, <https://anaconda.com>.
- ⁹⁶J. D. Hunter, ‘Matplotlib: A 2d graphics environment’, *Computing in Science & Engineering* **9**, 90–95 (2007).
- ⁹⁷M. D. Team, *Matplotlib: Visualization with Python*, version 3.9.2, <https://matplotlib.org>, 2024.
- ⁹⁸P. Virtanen, R. Gommers, T. E. Oliphant, M. Haberland, T. Reddy, D. Cournapeau, E. Burovski, P. Peterson, W. Weckesser, J. Bright, S. J. van der Walt, M. Brett, J. Wilson, K. J. Millman, N. Mayorov, A. R. J. Nelson, E. Jones, R. Kern, E. Larson, C. J. Carey, İ. Polat, Y. Feng, E. W. Moore, J. VanderPlas, D. Laxalde, J. Perktold, R. Cimrman, I. Henriksen, E. A. Quintero, C. R. Harris, A. M. Archibald, A. H. Ribeiro, F. Pedregosa, P. van Mulbregt and SciPy 1.0 Contributors, ‘SciPy 1.0: Fundamental Algorithms for Scientific Computing in Python’, *Nature Methods* **17**, 261–272 (2020).
- ⁹⁹J. Yu, *LaTeX Workshop*, version 10.10.2, VS Code extension, 14th Aug. 2025, <https://github.com/James-Yu/LaTeX-Workshop>.
- ¹⁰⁰Vel, S. R. Gunn and S. Patel, *Masters/Doctoral Thesis L^AT_EX Template*, version 2.5, licensed under a CC BY-NC-SA 3.0 license, (Aug. 2017) <https://www.latextemplates.com/template/masters-doctoral-thesis>.
- ¹⁰¹Street Side Software, *Code Spell Checker*, version 4.2.6, Aug. 2025, <https://marketplace.visualstudio.com/items?itemName=streetsidesoftware.code-spell-checker>.
- ¹⁰²OpenAI, *ChatGPT*, version GPT-4 and GPT-5, Large language model, 2025, <https://chat.openai.com/>.
- ¹⁰³Google, *Gemini*, version 2.5, Multimodal AI assistant, 2025, <https://gemini.google.com/>.
- ¹⁰⁴Google, *NotebookLM*, version latest available, AI research and document assistant with source citations, 2025, <https://notebooklm.google/>.
- ¹⁰⁵M. Duelli, *Data Analysis and Plotting for My Bachelor’s Thesis ‘Computer simulation of altermagnets with relativistic corrections’*, Oct. 2025, <https://github.com/Serenkii/Bachelor>.

- ¹⁰⁶F. Schütz, P. Kopietz and M. Kollar, 'What are spin currents in Heisenberg magnets?', *The European Physical Journal B - Condensed Matter and Complex Systems* **41**, 557–560 (2004).
- ¹⁰⁷P. J. Mohr, D. B. Newell, B. N. Taylor and E. Tiesinga, 'Codata recommended values of the fundamental physical constants: 2022', *Rev. Mod. Phys.* **97**, 025002 (2025).
- ¹⁰⁸Bureau International des Poids et Mesures, *Le système international d'unités / the international system of units*, 9th ed. (Bureau International des Poids et Mesures, 2025).

Tools Used

This section summarizes the tools that supported the creation of this work.

The simulations were performed on GPUs using the CUDA API, as described in Sec. 3.2. The core simulation software was written in C++, with version control managed via Git. The repository is hosted on a GitLab server administered by the University of Konstanz.

For data analysis and visualization, Python [93, 94] (via Anaconda [95]) was used, with development in PyCharm. The following packages played a central role:

- NumPy [82] for data manipulation and analysis
- Matplotlib [96, 97] for figure creation
- SciPy [98] for physical constants and curve fitting
- Standard Python libraries

The thesis itself was typeset in L^AT_EX using Visual Studio Code. Compilation was handled by latexmk with pdflatex, enabled by the LaTeX Workshop extension [99]. Bibliographic management was performed with biblatex. This document was created with a L^AT_EX-template [100] which was slightly adjusted.

For translation, DeepL was employed, and the Code Spell Checker extension [101] supported spell-checking.

Large language models also assisted during this work. ChatGPT [102] supported various tasks, including locating scientific sources, troubleshooting technical issues, assisting in plotting, and refining selected formulations (reviewed and revised by the author). Gemini [103] was used for exploring physical concepts and validating proposals. NotebookLM [104] aided in understanding selected papers and theoretical aspects.

Search engines used include Google, Google Scholar, and KonSearch (the University of Konstanz's internal system).

Finally, Git was used for version control of both this thesis and the accompanying Python project (data analysis and plotting scripts). Both repositories are hosted on GitHub. In the spirit of open science, the (admittedly unpolished) Python project is made publicly available here: [105]

Appendix A

Derivations in regards to Magnons

This appendix contains detailed calculations, derivations, and proofs related to section 2.1.4. For a more comprehensive collection of proofs, the appendix in Martin Evers' work [39] is recommended. The calculations presented here are those most relevant to the development of the concept of magnons.

A.1 Ground state of the ferromagnetic chain

The state with all spins pointing downwards along the chosen quantization axis z can be written as

$$|\psi_0\rangle := | -s, \dots, -s \rangle \quad (\text{A.1})$$

and is intuitively the state with lowest energy. First, it will be noted, that because of the omission of anisotropy and an external magnetic field. In all considerations only consisting of the Heisenberg exchange terms here, the state where all spins point exactly opposite is equivalent.

To treat the ground state, we show that $|\psi_0\rangle$ is an eigenstate

$$\begin{aligned} \hat{\mathcal{H}} |\psi_0\rangle &= -J \sum_{l=1}^N \left[\frac{1}{2} (\hat{S}_l^+ \hat{S}_{l+1}^- + \hat{S}_l^- \hat{S}_{l+1}^+) + \hat{S}_l^z \hat{S}_{l+1}^z \right] |\psi_0\rangle \\ &= -J \left[\frac{1}{2} \sum_l \hat{S}_l^+ \hat{S}_{l+1}^- |\psi_0\rangle + \frac{1}{2} \sum_l \hat{S}_l^- \hat{S}_{l+1}^+ |\psi_0\rangle + \sum_l \hat{S}_l^z \hat{S}_{l+1}^z |\psi_0\rangle \right] \\ &= -J \sum_l \hat{S}_l^z \hat{S}_{l+1}^z |\psi_0\rangle \\ &= -J \sum_{l=1}^N (-S) \cdot (-S) |\psi_0\rangle \\ &= -J N S^2 |\psi_0\rangle \\ &=: E_0 |\psi_0\rangle \end{aligned} \quad (\text{A.2})$$

and call the energy of this state E_0 . Here it was used, that $S_l^- |\psi_0\rangle = 0$ for any l , as the state cannot be lowered anymore.

Lastly, we quickly prove that this is indeed the state with the minimum energy. For that we calculate the expectation value

$$\begin{aligned}
\langle \psi | \mathcal{H} | \psi \rangle &= \left\langle \psi \left| -J \sum_l \hat{S}_l^z \hat{S}_{l+1}^z \right| \psi \right\rangle \\
&= -J \sum_l \langle \psi | \hat{S}_l^z \hat{S}_{l+1}^z | \psi \rangle \\
&= -J \sum_l \langle \psi | M_l M_{l+1} | \psi \rangle \\
&= -J \sum_l M_l \cdot M_{l+1} \langle \psi | \psi \rangle \\
&= -J \sum_l M_l \cdot M_{l+1} \\
&\geq -J \sum_l (-S) \cdot (-S) = E_0
\end{aligned} \tag{A.3}$$

and see that it is always greater or equal to E_0 because $-M_l \cdot M_{l+1} \geq -S^2$ for any l . That shows that the intuitive ground state is indeed the ground state of the system.

A.2 Excitation of a single spin

Here, it will be shown, that the state

$$|n\rangle := |M_1, \dots, M_{n-1}, M_n, M_{n+1}, \dots, M_N\rangle = |-S, \dots, -S, -S+1, -S, \dots, -S\rangle \tag{A.4}$$

is not an eigenstate of the Hamiltonian (2.17). This proves the intuitive ansatz for the smallest excitation wrong and leads to the development of magnons.

We apply $\hat{\mathcal{H}}$ to $|n\rangle$:

$$\begin{aligned}
\hat{\mathcal{H}} |n\rangle &= -J \sum_l \left[\frac{1}{2} (\hat{S}_l^+ \hat{S}_{l+1}^- + \hat{S}_l^- \hat{S}_{l+1}^+) + \hat{S}_l^z \hat{S}_{l+1}^z \right] |n\rangle \\
&= -J \left[\frac{1}{2} \sum_l \hat{S}_l^+ \hat{S}_{l+1}^- |n\rangle + \frac{1}{2} \sum_l \hat{S}_l^- \hat{S}_{l+1}^+ |n\rangle + \sum_l \hat{S}_l^z \hat{S}_{l+1}^z |n\rangle \right] \\
&= -J \left[\underbrace{\frac{1}{2} \hat{S}_{n-1}^+ \hat{S}_n^-}_{=:A} |n\rangle + \underbrace{\frac{1}{2} \hat{S}_n^- \hat{S}_{n+1}^+}_{=:B} |n\rangle + \underbrace{\sum_l \hat{S}_l^z \hat{S}_{l+1}^z}_{=:C} |n\rangle \right]
\end{aligned} \tag{A.5}$$

Now each part of the equation is calculated separately:

$$\begin{aligned}
A &= \frac{1}{2} \hat{S}_{n-1}^+ \hat{S}_n^- | -S, \dots, -S, -S + 1, -S, \dots, -S \rangle \\
&= \frac{1}{2} \sqrt{S(S+1) - (-S+1)((-S+1)-1)} \hat{S}_{n-1}^+ | -S, \dots, -S, -S, -S, \dots, -S \rangle \\
&= \frac{1}{2} \sqrt{2S} \hat{S}_{n-1}^+ | -S, \dots, -S, -S, -S, \dots, -S \rangle \\
&= \frac{1}{2} \sqrt{2S} \sqrt{S(S+1) - (-S)(-S+1)} | -S, \dots, -S + 1, -S, -S, \dots, -S \rangle \\
&= \frac{1}{2} \sqrt{(2S)^2} | -S, \dots, -S + 1, -S, -S, \dots, -S \rangle \\
&= S | n-1 \rangle
\end{aligned} \tag{A.6}$$

where $|n-1\rangle$ refers to the $(n-1)$ -th spin to be excited by $1\hbar$ analogous to $|n\rangle$. In the same manner

$$\begin{aligned}
B &= \frac{1}{2} \hat{S}_n^- \hat{S}_{n+1}^+ | -S, \dots, -S, -S + 1, -S, \dots, -S \rangle \\
&= \frac{1}{2} \sqrt{2S} \hat{S}_n^- | -S, \dots, -S, -S + 1, -S + 1, \dots, -S \rangle \\
&= \frac{1}{2} \sqrt{(2S)^2} \hat{S}_n^- | -S, \dots, -S, -S, -S + 1, \dots, -S \rangle \\
&= S | n+1 \rangle
\end{aligned} \tag{A.7}$$

and lastly

$$\begin{aligned}
C &= \sum_{l=1}^N \hat{S}_l^z \hat{S}_{l+1}^z | n \rangle \\
&= \hat{S}_1^z \hat{S}_2^z | n \rangle + \dots + \hat{S}_{n-1}^z \hat{S}_n^z | n \rangle + \hat{S}_n^z \hat{S}_{n+1}^z | n \rangle + \dots + \hat{S}_N^z \hat{S}_1^z | n \rangle \\
&= (-S)^2 | n \rangle + \dots + (-S)(-S+1) | n \rangle + (-S+1)(-S) | n \rangle + \dots + (-S)^2 | n \rangle \\
&= S^2 | n \rangle + \dots + (S^2 - S) | n \rangle + (S^2 - S) | n \rangle + \dots + S^2 | n \rangle \\
&= (NS^2 - 2S) | n \rangle .
\end{aligned} \tag{A.8}$$

The result then is

$$\hat{\mathcal{H}} | n \rangle = -J [S | n-1 \rangle + S | n+1 \rangle + (NS^2 - 2S) | n \rangle] \tag{A.9}$$

which shows that $|n\rangle$ is not an eigenstate of $\hat{\mathcal{H}}$ as $|n \pm 1\rangle$ and $|n\rangle$ are linearly independent.

A.3 Single magnon state

It has been established, that $|n\rangle$ is not a suitable excited state. Instead,

$$|k\rangle = \frac{1}{\sqrt{N}} \sum_{n=1}^N e^{ikna} |n\rangle \tag{A.10}$$

as a superposition of the single excited spins is proposed. The factor $1/\sqrt{N}$ ensures normalization of the state [39].

It will now be proven, that $|k\rangle$ is indeed an eigenstate. For that $\hat{\mathcal{H}}|k\rangle$ is explicitly calculated using equation (A.9):

$$\begin{aligned}
\hat{\mathcal{H}}|k\rangle &= \frac{1}{\sqrt{N}} \sum_{n=1}^N e^{ikna} \hat{\mathcal{H}}|n\rangle \\
&= -J \frac{1}{\sqrt{N}} \sum_{n=1}^N e^{ikna} (S|n-1\rangle + S|n+1\rangle + (NS^2 - 2S)|n\rangle) \\
&= -JS \left(\frac{1}{\sqrt{N}} \sum_{n=1}^N |n-1\rangle + \frac{1}{\sqrt{N}} \sum_{n=1}^N |n+1\rangle + (NS-2) \frac{1}{\sqrt{N}} \sum_{n=1}^N |n\rangle \right) \\
&= -JS \left(\frac{1}{\sqrt{N}} \sum_{n=0}^{N-1} e^{ik(n+1)a} |n\rangle + \frac{1}{\sqrt{N}} \sum_{n=2}^{N+1} e^{ik(n-1)a} |n\rangle + (NS-2) |k\rangle \right) \\
&= -JS (e^{ika}|k\rangle + e^{-ika}|k\rangle + (NS-2)|k\rangle) \\
&= -JS (e^{ika} + e^{-ika} + (NS-2))|k\rangle
\end{aligned} \tag{A.11}$$

Here, the periodic boundary conditions were used, which makes shifts in the summation irrelevant, as $\hat{S}_0 = \hat{S}_N$ and $\hat{S}_1 = \hat{S}_{N+1}$. Furthermore, we use $e^{ika} + e^{-ika} = 2\cos(ka)$ and get

$$\begin{aligned}
\hat{\mathcal{H}}|k\rangle &= -JS (2\cos(ka) - 2 + NS)|k\rangle \\
&= -JS (2\cos(ka) - 2)|k\rangle + (-JNS^2)|k\rangle \\
&=: E(k)|k\rangle
\end{aligned} \tag{A.12}$$

where $-JNS^2$ is identified as the ground state energy E_0 from (A.2). Furthermore, we can write the eigenvalue as

$$\begin{aligned}
E(k) &= \hbar \left[\frac{JS}{\hbar} (2 - 2\cos(ka)) \right] + E_0 \\
&= E_0 + \hbar\omega(k)
\end{aligned} \tag{A.13}$$

and call $\omega(k)$ the dispersion relation of the single-magnon state $|k\rangle$.

The interpretation of this state can be found in section 2.1.4.

As a last remark, it should be mentioned, that the wave vector k (e.g. in (A.10)) cannot take arbitrary values. To fulfil the conditions of periodic boundaries, $e^{ikna} = e^{ik(n+N)a}$ must be true for all lattice indices n . Therefore:

$$\begin{aligned}
e^{ikna} &= e^{ikna} \cdot e^{ikNa} \\
\Rightarrow 1 &= e^{ikNa} \\
\Rightarrow 2\pi m &= kNa \quad (m \in \mathbb{Z}) \\
\Rightarrow k &= \frac{2\pi m}{Na}
\end{aligned} \tag{A.14}$$

Often, k is restricted to the first Brillouin zone, meaning that $k \in [-\frac{\pi}{a}, \frac{\pi}{a}]$ and therefore restricting m to $m \in \{m \in \mathbb{Z} : -\frac{N}{2} \leq m < \frac{N}{2}\}$ for example [48]. In practice, this can often be overlooked because N becomes so large that the discrete steps can easily be approximated by treating k as continuous.

A.4 Extended Heisenberg model

To keep it simple, previous derivations have been done with only the Heisenberg exchange term (2.4). Adding an easy axis anisotropy and a Zeeman term with a magnetic field along the same quantization axis z does not increase the difficulty in treating the system. This is because both terms only include the \hat{S}_l^z operator, which does not change $|\psi_0\rangle$, $|n\rangle$ nor $|k\rangle$. Therefore, a Zeeman term or an anisotropy of this kind just shifts the ground state energy E_0 and the dispersion relation $\omega(k)$ by a constant.

The specifics can be found in [39], where they are also proved.

Appendix B

Miscellaneous

Here, we present the derivation for spin current formulas and a proof regarding the implementation of DMI.

B.1 Derivation of formulas for spin currents

We derive expressions for spin currents in multisublattice systems based on the microscopic spin configuration which can be found in Sec. 2.3, explicitly Eqs. (2.46) to (2.48). The basis for this derivation is chapter 7.1 of Ritzmann's dissertation [29] and the derivation of Weissenhofer and Marmodoro in [23].

For simplicity, we consider a one-dimensional chain of unit cells. There are s sublattices. We consider the edge case of no Gilbert damping in the Landau-Lifshitz-Gilbert (LLG) equation

$$\dot{\vec{S}}_i(t) = -\frac{\gamma}{\mu_s} \vec{S}_i(t) \times \left(-\frac{\partial \mathcal{H}}{\partial \vec{S}_i} + \vec{\xi}(t) \right) \quad (\text{B.1})$$

and consider the extended Heisenberg model (2.4). Taking the average gets rid of the $\vec{\xi}(t)$ -term ($\langle \vec{\xi}_i(t) \rangle = 0$) and the derivative of the Hamiltonian results in

$$\left\langle \sum_s \dot{\vec{S}}_i^s \right\rangle = -\frac{\gamma}{\mu_s} \sum_j \sum_s \sum_{s'} J_{ij}^{ss'} \left\langle \vec{S}_i^s \times \vec{S}_j^{s'} \right\rangle \quad (\text{B.2})$$

for the time-averaged change of the magnetic moment in a single unit cell with index i . The sums go over each neighbor j , and all sublattices s, s' and $J_{ij}^{ss'}$ is the exchange energy.

We now consider the continuity equation of the form $\partial_x j + \dot{\rho} = 0$ [26]. This idea can also for example be found in [106]. Here, $j := j_i$ refers to the net flux into unit cell i . We identify $\dot{\rho} := \sum_s \dot{\vec{S}}_i^s$ and assume a discrete equation, as the position coordinate of the lattice is discretely defined with the lattice constant a .

The resulting equation is

$$\left\langle \sum_s \dot{\vec{S}}_i^s \right\rangle = -\frac{\vec{j}_i^{\text{in}} - \vec{j}_i^{\text{out}}}{a} \quad (\text{B.3})$$

where we have additionally split the net flux in the unit cell into the incoming and outgoing spin currents j_i^{in} and j_i^{out} . Conventionally we view spin momentum coming from the left ($j < i$) as incoming and interaction with spins on the right ($j > i$) as outgoing. Note, that $j = i$ causes the term to become zero because of the cross

product. We can therefore identify incoming and outgoing spin currents as

$$\vec{j}_i^{\text{in}} = \frac{\gamma}{\mu_s} a \sum_{ss', j < i} J_{ij}^{ss'} \left\langle \vec{S}_i^s \times \vec{S}_j^{s'} \right\rangle, \quad (\text{B.4})$$

and

$$\vec{j}_i^{\text{out}} = -\frac{\gamma}{\mu_s} a \sum_{ss', j > i} J_{ij}^{ss'} \left\langle \vec{S}_i^s \times \vec{S}_j^{s'} \right\rangle. \quad (\text{B.5})$$

In (quasi-) equilibrium the average of the magnetic moment stays constant ($\langle \sum_s \vec{S}_i^s \rangle = 0$) and therefore incoming and outgoing currents are equal, $-\vec{j}_i^{\text{in}} = \vec{j}_i^{\text{out}} =: \vec{j}_i$. Therefore we can use this formula to calculate the spin current along a direction of our lattice. The components of the vector \vec{j} represent the component of magnetization, which the current is carrying. In three dimensions, this situation becomes more complex, as we have three components of magnetization which can be carried and three directions. Therefore, \vec{j} is a tensor in three dimensions [29].

Now, the derived formula (B.5) is adapted to our use case. In this work, we are interested in spin currents along the directions depicted in Fig. 2.6. Therefore, the one-dimensional interpretation is projected on the crystallographic axes of interest. The indices in Eq. (B.5) then refer to these directions.

One could rewrite the equation to

$$\vec{j}(\vec{r}) = -\frac{\gamma}{\mu_s} a \sum_{ss', n} J_n^{ss'} \left\langle \vec{S}^s(\vec{r}) \times \vec{S}^{s'}(\vec{r} + \vec{a} \cdot \vec{e}_\theta) \right\rangle \quad (\text{B.6})$$

to refer to the spin current which is carried along direction \vec{e}_θ . Here, $J_n^{ss'}$ is the exchange energy between spin $\vec{S}^s(\vec{r})$ and $\vec{S}^{s'}(\vec{r} + \vec{a} \cdot \vec{e}_\theta)$.

In this work, the z component of the spin is transported. Therefore, the cross product is additionally multiplied by \vec{e}_z which yields

$$j_z(\vec{r}) = -\frac{\gamma}{\mu_s} a \sum_n J_n^{ss'} \left\langle \left(\vec{S}^s(\vec{r}) \times \vec{S}^{s'}(\vec{r} + \vec{a} \cdot \vec{e}_\theta) \right) \cdot \vec{e}_z \right\rangle \quad (\text{B.7})$$

Considering the nonzero exchange interactions, this derivation yields the following formulas for spin currents along different directions θ for the toy model introduced in Sec. 2.2.1.

For the directions [1 0 0] and [0 1 0] the resulting formula is

$$\begin{aligned} j_z^\theta(\vec{r}) =: j^\theta(\vec{r}) &= -\frac{\gamma_e}{\mu_B} a J_1 \left(\left\langle S_x^A(\vec{r}) \cdot S_y^B(\vec{r} + \vec{a} \cdot \vec{e}_\theta) - S_y^A(\vec{r}) \cdot S_x^B(\vec{r} + \vec{a} \cdot \vec{e}_\theta) \right\rangle \right. \\ &\quad \left. + \left\langle S_x^B(\vec{r}) \cdot S_y^A(\vec{r} + \vec{a} \cdot \vec{e}_\theta) - S_y^B(\vec{r}) \cdot S_x^A(\vec{r} + \vec{a} \cdot \vec{e}_\theta) \right\rangle \right). \end{aligned} \quad (\text{B.8})$$

Here, a is the lattice constant, J_1 is the nearest-neighbour exchange interaction and μ_B is the Bohr magneton, which is the magnetic moment of a single spin in this work. The gyromagnetic ratio used in this toy model is the electron gyromagnetic ratio γ_e . For the straight directions, $\theta \in \{[1 0 0], [0 1 0]\}$ with $\vec{e}_{[1 0 0]} = \begin{pmatrix} 1 \\ 0 \\ 0 \end{pmatrix}$ and $\vec{e}_{[0 1 0]} = \begin{pmatrix} 0 \\ 1 \\ 0 \end{pmatrix}$. The subscripts refer to the spin components, and the superscripts refer to the sublattices.

Similarly, we obtain the formulas

$$\begin{aligned} j^{[1\bar{1}0]}(\vec{r}) = & -\frac{\gamma_e}{\mu_B} \tilde{a} \left(J_2' \left\langle S_x^A(\vec{r}) \cdot S_y^A(\vec{r} + \tilde{a} \cdot \vec{e}_{[1\bar{1}0]}) - S_y^A(\vec{r}) \cdot S_x^A(\vec{r} + \tilde{a} \cdot \vec{e}_{[1\bar{1}0]}) \right\rangle \right. \\ & \left. + J_2 \left\langle S_x^B(\vec{r}) \cdot S_y^B(\vec{r} + \tilde{a} \cdot \vec{e}_{[1\bar{1}0]}) - S_y^B(\vec{r}) \cdot S_x^B(\vec{r} + \tilde{a} \cdot \vec{e}_{[1\bar{1}0]}) \right\rangle \right) \end{aligned} \quad (\text{B.9})$$

and

$$\begin{aligned} j^{[110]}(\vec{r}) = & -\frac{\gamma_e}{\mu_B} \tilde{a} \left(J_2 \left\langle S_x^A(\vec{r}) \cdot S_y^A(\vec{r} + \tilde{a} \cdot \vec{e}_{[110]}) - S_y^A(\vec{r}) \cdot S_x^A(\vec{r} + \tilde{a} \cdot \vec{e}_{[110]}) \right\rangle \right. \\ & \left. + J_2' \left\langle S_x^B(\vec{r}) \cdot S_y^B(\vec{r} + \tilde{a} \cdot \vec{e}_{[110]}) - S_y^B(\vec{r}) \cdot S_x^B(\vec{r} + \tilde{a} \cdot \vec{e}_{[110]}) \right\rangle \right) \end{aligned} \quad (\text{B.10})$$

for the diagonal directions. Here, we have $\vec{e}_{[1\bar{1}0]} = \frac{1}{\sqrt{2}} \begin{pmatrix} 1 \\ -1 \end{pmatrix}$ and $\vec{e}_{[110]} = \frac{1}{\sqrt{2}} \begin{pmatrix} 1 \\ 1 \end{pmatrix}$. The lattice constant has changed to reflect the distance between the lattice points: $\tilde{a} = 2a_{\text{tilt}} = \frac{2}{\sqrt{2}}a$ as defined in Eq. (3.11).

Note, that because of the setup of the toy model in this work, spin currents along the straight crystallographic directions are always intersublattice spin currents, while spin currents along the diagonal directions are always intrasublattice currents.

The fraction $\frac{\gamma_e}{\mu_B}$ can be simplified to $\frac{g_e}{\hbar}$ with the g -factor of an electron $g_e \approx 2$ [107]. The dimension of the derived quantity for the spin current is $L T^{-1}$ [108]. This dimension makes sense here because we are working with dimensionless spins. If a more practical unit was desired, one could for example multiply Eq. (B.2) with the magnetic moment of a single spin and divide by an area. Then the resulting formulas contain this quantity which yields dimensions of a magnetic moment flux.

If we were interested in the spin along for example $[\bar{1}\bar{1}0]$, we can use $j^{[\bar{1}\bar{1}0]} = -j^{[110]}$ as the outgoing current in one direction is opposite to the outgoing current in the opposite direction.

B.2 Implementation of DMI

We will show that the use of the 3×3 exchange tensor

$$\mathfrak{J}_1^\pm = \begin{pmatrix} \mathfrak{J}^{xx} & \mathfrak{J}^{xy} & \mathfrak{J}^{xz} \\ \mathfrak{J}^{yx} & \mathfrak{J}^{yy} & \mathfrak{J}^{yz} \\ \mathfrak{J}^{zx} & \mathfrak{J}^{zy} & \mathfrak{J}^{zz} \end{pmatrix} = \begin{pmatrix} J_1 & 0 & 0 \\ 0 & J_1 & \pm D \\ 0 & \mp D & J_1 \end{pmatrix} \quad (\text{B.11})$$

which is introduced in section 3.4 produces the same result as a separate scalar exchange and DMI term. Specifically, we want to show that

$$\mathfrak{J}_1^+ \cdot \vec{S}_A \cdot \vec{S}_B = \vec{S}_B^T \cdot \mathfrak{J}_1^+ \cdot \vec{S}_A \stackrel{!}{=} J_1 \cdot \vec{S}_A \cdot \vec{S}_B + \vec{D} \cdot (\vec{S}_A \times \vec{S}_B) \quad (\text{B.12})$$

where

$$\vec{D} = \begin{pmatrix} D \\ 0 \\ 0 \end{pmatrix} \quad (\text{B.13})$$

is the DM-vector as introduced in 2.2.2. We prove explicitly by performing the calculations.

Let

$$\vec{S}_A = \begin{pmatrix} S_A^x \\ S_A^y \\ S_A^z \end{pmatrix} \quad \text{and} \quad \vec{S}_B = \begin{pmatrix} S_B^x \\ S_B^y \\ S_B^z \end{pmatrix}. \quad (\text{B.14})$$

Now we calculate the matrix calculation on the left side of equation (B.12). We can also directly write it as a sum over its entries

$$\sum_{\theta, \eta} \mathfrak{J}^{\theta\eta} \cdot S_A^\theta \cdot S_B^\eta = J_1 S_A^x S_B^x + J_1 S_A^y S_B^y + J_1 S_A^z S_B^z + D S_A^y S_B^z - D S_A^z S_B^y \quad (\text{B.15})$$

where $\theta, \eta \in \{x, y, z\}$.

To compare, we calculate the right side of equation (B.12):

$$\begin{aligned} & J_1 \cdot \vec{S}_A \cdot \vec{S}_B + \vec{D} \cdot (\vec{S}_A \times \vec{S}_B) \\ &= J_1 \cdot \begin{pmatrix} S_A^x \\ S_A^y \\ S_A^z \end{pmatrix} \cdot \begin{pmatrix} S_B^x \\ S_B^y \\ S_B^z \end{pmatrix} + \begin{pmatrix} D \\ 0 \\ 0 \end{pmatrix} \cdot \left[\begin{pmatrix} S_A^x \\ S_A^y \\ S_A^z \end{pmatrix} \times \begin{pmatrix} S_B^x \\ S_B^y \\ S_B^z \end{pmatrix} \right] \\ &= J_1 S_A^x S_B^x + J_1 S_A^y S_B^y + J_1 S_A^z S_B^z + D \cdot [S_A^y S_B^z - S_A^z S_B^y] \\ &= J_1 S_A^x S_B^x + J_1 S_A^y S_B^y + J_1 S_A^z S_B^z + D S_A^y S_B^z - D S_A^z S_B^y \end{aligned} \quad (\text{B.16})$$

We see that (B.15) is the same as (B.16), which proves (B.12) to be true. When calculating the same for the exchange list for SL B, the role of \vec{S}_A and \vec{S}_B change in the cross product. Because of its anti-commutative properties, this is the same as using \mathfrak{J}_1^- .

It is shown that this definition of the exchange matrix is a valid implementation of the DMI.

We denote again that the implementation of DMI in this toy model destroys its alternating magnetic symmetry, as discussed in Sec. 2.2.2.

Erklärung

Ich versichere hiermit, dass ich die anliegende Abschlussarbeit mit dem Thema:
Computer simulation of altermagnets with relativistic corrections
 selbstständig verfasst und keine anderen Hilfsmittel und Quellen als die angegebenen benutzt habe.

Falls ich textgenerierende KI-Tools als Hilfsmittel verwendet habe, ist mir bewusst, dass ich allein für die inhaltliche Richtigkeit von KI generierten Textpassagen und die Kennzeichnung von Formulierungen und Ideen anderer Personen gemäß den Grundsätzen der guten wissenschaftlichen Praxis verantwortlich bin. Die Stellen, die anderen von natürlichen Personen verfassten Werken (auch aus dem Internet und oder anderen elektronischen Text- und Datensammlungen entnommen) dem Wortlaut oder dem Sinn nach entnommen sind, habe ich in jedem einzelnen Fall durch Angabe der Quelle bzw. der Sekundärliteratur als Entlehnung kenntlich gemacht.

Ich habe zur Kenntnis genommen, dass die Prüfungs- oder Studienleistung bei Täuschung über die Eigenständigkeit oder durch Benutzung nicht zugelassener oder ggf. zugelassener aber nicht ausreichend angegebener Hilfsmittel als „nicht bestanden (5,0)“ bewertet wird und dass in besonders schwerwiegenden Täuschungsfällen der zuständige Prüfungsausschuss mich von der Wiederholungsprüfung ausschließen kann mit der Folge des endgültigen Verlustes des Prüfungsanspruchs.

Weiterhin versichere ich hiermit, dass die o.g. Arbeit noch nicht anderweitig als Abschlussarbeit einer Diplom-, Bachelor- bzw. Masterprüfung eingereicht wurde. Mir ist ferner bekannt, dass ich bis zum Abschluss des Prüfungsverfahrens die Materialien verfügbar zu halten habe, welche die eigenständige Abfassung der Arbeit belegen können.

Die Arbeit wird nach Abschluss des Prüfungsverfahrens der Bibliothek der Universität Konstanz übergeben und katalogisiert. Damit ist sie durch Einsicht und Ausleihe öffentlich zugänglich. Die erfassten beschreibenden Daten wie z.B. Autor, Titel usw. stehen öffentlich zur Verfügung und können durch Dritte (z.B. Suchmaschinenanbieter oder Datenbankbetreiber) weiterverwendet werden.

Als Urheber der anliegenden Arbeit stimme ich dem obigen Veröffentlichungsverfahren zu.

